Nonlinear Combustion Instabilities and Stochastic Sources

Thesis by
Victor S. Burnley

In Partial Fulfillment of the Requirements
for the Degree of
Doctor of Philosophy

California Institute of Technology
Pasadena, California

1996

(Defended January 8, 1996)

Acknowledgements

First, I would like to thank Professor Fred E. C. Culick. Without his guidance, this work would not have been possible. Jay Levine has been most helpful and supportive over the course of the program. His patience has been much appreciated. Professor Edward Zukoski contributed many useful suggestions. I would like to acknowledge the guidance of the remaining members of my thesis committee, Professor Joel Franklin and Professor Anthony Leonard, as well.

I am greatly indebted to Professor Eusebius Doedel for the use of his program AUTO. It was an invaluable tool in this study. In addition, he provided helpful discussions regarding its use and bifurcation theory in general. Dr. Craig Jahnke helped immensely in the initial understanding of nonlinear systems, while Dr. Leonidas Paparizos provided a good background in stochastic processes. I would like to thank Grant Swenson for his help in performing some of the numerical calculations for this study.

Thanks also go to my friends at Caltech for their support in this effort. Although there are many more unmentioned, I would like to thank the following people in particular: Dr. Andrew Lewis for many helpful discussions regarding TEX and other noble pursuits; Windsor Lin for help with practically everything; Richard Tsuyuki (Palmerston or Bust!); Patrick Lemieux for keeping me sane; Sudipto Sur and Kevin Moore for lots of computer help; and Drs. Donald Kendrick and Tom Zsak for making JPC a great place to work. Furthermore, the following people have helped in various ways: Ingrid Mounier; Dr. Mark E. Walter; Dr. Jim Ostrowski; Howie Choset; Lucky Benedict; Marionne Kirk; Dr. James Sterling; and Fabienne Breton.

Special thanks go to Dorothy Eckerman. She provided lots of support and was always there when I needed someone to talk to. Above all, I would like to thank my family for their constant love and support.

Nonlinear Combustion Instabilities and Stochastic Sources

by

Victor S. Burnley

In Partial Fulfillment of the
Requirements for the Degree of
Doctor of Philosophy

Abstract

An investigation of combustion instabilities was conducted using an approximate analysis which allows any relevant physical processes to be included. The resulting system of coupled nonlinear oscillator equations was studied using the methods of dynamical systems theory. Previous investigations have further simplified the system using the method of time-averaging and truncation to a small number of modes. We have investigated the consequences of using these additional approximations, a case which had not been addressed completely in the literature. It was determined that application of the method of time-averaging introduces a stability boundary which limits the range in which the averaged equations are valid.

Transverse oscillations in a cylindrical chamber were also treated. It was established that in addition to its role in energy transfer between modes, nonlinear gasdynamics also provides a means of shifting the frequencies of oscillations to integral multiples of the fundamental. This additional role can reduce the efficiency of energy transfer, thus increasing the acoustic amplitudes. An example of a low amplitude transverse oscillation was produced suggesting a

means by which the amplitudes of transverse modes, as well as nonintegral longitudinal modes, may be reduced.

The coupling between combustion processes and acoustic oscillations was studied as a possible explanation of the phenomenon known as triggering. Using several ad hoc models, the effects of nonlinear pressure coupling and velocity coupling on the behavior of the system were investigated. Substantial regions of possible triggering were produced when using a model of velocity coupling with a threshold, but only if nonlinear gasdynamics was also included.

The interaction between combustion noise and acoustic instabilities has received relatively little attention. The sources of noise in a combustion chamber are associated with vorticity and entropy waves. By including these contributions in the approximate analysis, the general forms of the stochastic excitations were obtained. Subsequently, the effects of these excitations on the amplitudes of acoustic modes were studied. When only nonlinear gasdynamics was included, no cases of bimodal probability density functions, characteristic of triggering, were found. However, when the model of velocity coupling with a threshold is added, bimodal probability densities can occur.

Contents

List of Figures

List of Tables

List of Symbols

Symbol	: Description
a	: speed of sound
$\bar{a}$	: mass-averaged speed of sound, Eq. (2.21)
A	: burning rate parameter
A_b	: admittance function for the burning surface
A_n, B_n	: slowly varying amplitudes, Eq. (2.58)
A_{nij}, B_{nij}	: nonlinear gasdynamic coefficients, Eq. (2.53)
B	: burning rate parameter
c	: specific heat of the particulate matter
c_p	: specific heat at constant pressure of the gas phase
$\bar{c}_p$	: mass-averaged specific heat at constant pressure
c_v	: specific heat at constant volume of the gas phase
$\bar{c}_v$	: mass-averaged specific heat at constant volume
C_m	: ρ_p/ρ_g, density ratio
$C_{ni}^{(1)}, C_{ni}^{(2)}$	: nonlinear gasdynamic coefficients for longitudinal modes
$D_{ni}^{(1)}, D_{ni}^{(2)}$	: nonlinear gasdynamic coefficients for longitudinal modes
D	: diameter of chamber
e_0	: stagnation energy, gas phase
E_n^2	: inner product defined by Eq. (2.45)
E_s	: activation energy of surface reaction

$\bar{E}_s$: $E_s/R_0\bar{T}_s$, normalized surface activation energy

f : nonlinear functional arising from the boundary condition

F_n : forcing function of the n^{th} acoustic mode

$\boldsymbol{\mathcal{F}}$: Eq. (2.27)

$\boldsymbol{\mathcal{F}}_p$: force exerted on fluid by particles

h : nonlinear functional arising from the conservation equations

$I_{nij}^{(A)}, I_{ni}^{(B)}, I_{nij}^{(C)}$: nonlinear combustion coefficients, Eq. (5.42)

J_m : Bessel function of the first kind of order m

k : thermal conductivity

k_l : wave number of the n^{th} longitudinal mode

k_n : wave number of the n^{th} acoustic mode

L : length of chamber

$\dot{m}$: mass flux at the surface

M_b : u_{b}/a, Mach number at the burning surface

M_r : characteristic Mach number

n : pressure exponent in linear burning rate

$\hat{\boldsymbol{n}}$: unit normal vector

p : pressure

$\mathcal{P}$: Eq. (2.28)

$\boldsymbol{q}$: heat transfer by conduction

Q : heat released by chemical reactions

Q_p : heat transfer between phases

r_n : amplitude, Eq. (2.58)

R : radius of chamber

R_0 : universal gas constant

$\bar{R}_0$: mass-averaged universal gas constant

$\boldsymbol{r}$: spatial coordinates

R_b : linear pressure coupled response function

R_{vc} : velocity coupled response function

$\bar{R}_{\mathrm{vc}}$: $R_{\mathrm{vc}}a$, nondimensional velocity coupled response function

s : entropy

S : surface area

t : time

T : temperature

T_c : temperature of the cold propellant

$\boldsymbol{u}$: velocity

V : volume

w : reaction rate

W : Wiener process

x : longitudinal coordinate

$\tilde{x}$: $\pi x/L$, nondimensional coordinate

X_{R} : phase difference of the first tangential and first radial modes

X_{T} : phase difference of the first and second tangential modes

Greek Symbols :

α_n : linear growth rate of the n^{th} acoustic mode

β : nonlinear gasdynamic coefficient for the time-averaged equations

β_1 : temperature exponent in Arrhenius Law

δ_{mn} : Kronecker delta

ε_n : nondimensional energy in the n^{th} acoustic mode

γ : ratio of specific heats

$\bar{\gamma}$: mass-averaged ratio of specific heats

κ_{ms} : wave number of the transverse mode, determined by solving Eq. (2.57)

λ : complex function of frequency, Eq. (5.7)

η_n : amplitude of the n^{th} acoustic mode

ζ_n : $d\eta_n/dt$

ξ : parametric stochastic excitation associated with pressure

ξ^v : parametric stochastic excitation associated with velocity

Ξ : external stochastic excitation

ρ : density

$\boldsymbol{\sigma}$: momentum transfer between gas and particles due to residual combustion

$\overleftrightarrow{\tau}$: viscous stress tensor

τ_1 : period of the fundamental mode

τ_c : correlation time

θ_n : frequency shift of the n^{th} acoustic mode

ϕ_n : phase, Eq. (2.58)

ψ_n : mode shape of the n^{th} acoustic mode

ω_n : frequency of the n^{th} acoustic mode

$\dot{\omega}_p$: rate of conversion of particulate material to gas

Ω : $\nabla \times \boldsymbol{u}$, vorticity

Subscripts :

a : value in acoustic wave

b : at the burning surface

f : flame

g : gas

p : particle

pc : pressure coupled

s : value at the solid-gas interface; or value in entropy wave

vc : velocity coupled

1R : first radial mode

1T : first tangential mode

2T : second tangential mode

Ω : value in vorticity wave

Superscripts :

BL : Baum and Levine's model

G : Greene's model

GD : gasdynamics

NL : nonlinear

(r) : real part of a complex quantity

(i) : imaginary part of a complex quantity

$\bar{}$: mean quantity

$'$: fluctuating quantity

$\dot{}$: time derivative

Chapter 1

Introduction

Early in the development of rocket propulsion, it became apparent that unwanted oscillatory motions often occur in propulsion systems. These oscillatory motions, commonly referred to as combustion instabilities, still present a problem in the design of modern systems. Combustion instabilities arise due to a high energy density being confined to a chamber where dissipation is relatively small [15]. Only a very small fraction of the available energy is required to start and maintain oscillations having unacceptable amplitudes. These oscillations can cause unwanted vibrations and in extreme cases can lead to failure of the propulsion system.

There are two general types of nonlinear oscillations which occur in combustion chambers, spontaneous oscillations and pulsed oscillations. A spontaneous oscillation, or intrinsic instability, occurs when the system is linearly unstable so that any perturbation in the pressure field will grow exponentially in time. Under the influence of nonlinear effects, the pressure field may reach a periodic motion, or limit cycle. An example of a spontaneous oscillation is shown in Fig. 1.1. A pulsed oscillation, on the other hand, is a true nonlinear instability of a linearly stable system. Small perturbations in the pressure field decay exponentially to zero, while larger perturbations may lead to stable or unstable periodic motions. Examples of a pulsed oscillation for a stable and

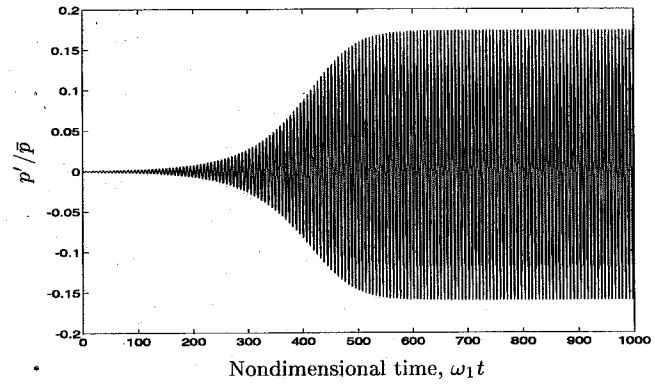

Figure 1.1 Example of a spontaneous oscillation; pressure at the head end of the chamber after a small perturbation

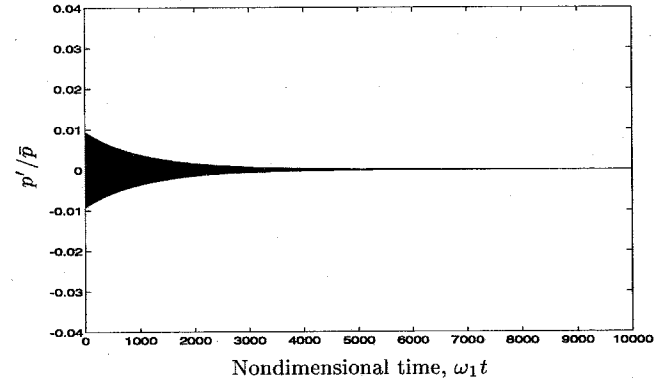

Figure 1.2 Example of a pulsed oscillation; pressure at the head end of the chamber after a stable initial pulse

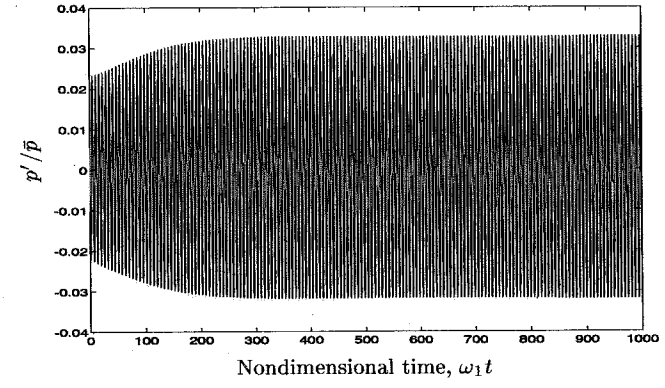

Figure 1.3 Example of a pulsed oscillation; pressure at the he end of the chamber after an unstable initial pulse

unstable initial pulse are shown in Figs. 1.2 and 1.3.

Spontaneous oscillations have often been encountered in practice since dissipative mechanisms inside combustion chambers are usually quite small. For this reason, the first investigations into combustion instabilities dealt only with the question of linear stability. This was the main thrust of research in the 1950s and 1960s [22]. The linear problem is now fairly well understood and gives much information about intrinsic instabilities [21]. However, solution to the linear problem is insufficient to predict limiting amplitudes of oscillations and offers no hope of capturing pulsed instabilities, or "triggering." Due to these insufficiencies, investigations into nonlinear behavior were pursued in order to address the following two questions: 1) what limiting amplitude will a linearly unstable system reach; and 2) under what conditions will a linearly stable system exhibit triggering?

The first question has been the focus of many studies over the past three decades. Chu and Ying [7], in the first study concerning linear instability, used the method of characteristics to treat thermally driven waves in a pipe. Using a pressure sensitive heat source, a limit cycle was determined to occur, although combustion processes and mean flow were not considered in their analysis. Sirignano and Crocco [54] investigated some of the influences of combustion and mean flow using techniques similar to those of Chu and Ying. A weak shock model was employed to study limit cycles in a rocket motor where combustion was assumed to occur in a negligibly small region at the head end of the chamber. Both of these analyses, however, involved the solution of partial differential equations for specific problems, and it was not possible to obtain general trends applicable to other systems.

An important change in the study of linear instabilities was introduced by Zinn and Powell [59] in their investigation of transverse oscillations in liquid rocket motors. Galerkin's method was applied to spatially average the conser-

vation equations using a single mode approximation to the spatial waveform of the oscillation. The resulting set of ordinary differential equations for the unknown dependent variables was then solved numerically.

Independently, Culick [12] applied spatial averaging to study longitudinal oscillations in solid rocket motors. Again, the acoustic field was approximated by a single mode. An additional simplification was introduced by the application of time-averaging, a step which not only gives a reduction in computational time, but also provides a framework to more easily obtain general trends of the problem. More careful examination of experimental results for solid propellant rockets and T-burners revealed that the acoustic field was more complicated, and the approximate analysis was reformulated to explicitly include all possible acoustic waves in a later work [13].

The only means of checking the validity of the approximate analysis based on spatial and time-averaging is by comparison with numerical results due to the large uncertainties associated with experimental data. Culick and Levine [19] performed such a comparison for a limited number of cases involving one-dimensional flows. The approximate analysis was shown to produce good agreement with numerical methods, at least for cases where the amplitudes do not become too large.

Subsequently, the approximate analysis has been used systematically to investigate the problem of linear instability, and considerable progress has been made. Awad and Culick [3] and Yang and Culick [55] studied the conditions for the existence and stability of limit cycles for longitudinal and transverse acoustic modes, respectively. Both of these works used the time-averaged equations along with truncation to a small number of modes. It was also assumed in both works that gasdynamics, to second-order only, provided the only nonlinear influences. These works established that, in this case, the existence and stability of limit cycles depend only on the linear parameters of

the system, while nonlinear gasdynamics influences the limiting amplitudes.

Paparizos and Culick [51] obtained exact results for the existence, stability, and amplitude of limit cycles for two longitudinal modes in a cylindrical chamber using the time-averaged equations. The results were consistent with the previous works but provided more insight by utilizing a geometrical representation theory. This work also extended the previous results by considering the energy transfer between modes. It was determined that the preferred direction of energy transfer is from the lower to the higher acoustic modes, consistent with experimental observations and with the fundamental behavior of compressible motions in fluid mechanics. The effect of truncating the infinite system to two modes was also addressed by comparison of the exact results with numerical results for higher numbers of modes.

Exact solutions, such as those obtained by Paparizos and Culick [51], have been obtained only for a limited number of cases. In fact, analytic solutions have been restricted to the time-averaged equations with nonlinear influences arising from gasdynamics only and truncation to a small number of modes. In order to determine the effects of these approximations, Jahnke and Culick [37, 38] first applied the methods of dynamical systems theory. Using continuation methods, the effects of truncation to a small number of modes and time-averaging were investigated. The results showed that these approximations may have a strong effect on the behavior of the system of equations. For instance, in the case of a first mode instability, the two-mode, time-averaged equations predict a stability boundary above which no stable periodic solutions exist. Application of dynamical systems theory showed that this stability boundary does not occur with the original equations. This investigation illustrated the usefulness of dynamical systems theory in determining general trends which would be much more difficult to obtain using numerical simulations.

The second question, "under what conditions will a linearly stable system exhibit triggering?," has received increasingly more attention as the understanding of linear instability has grown. This question is important because the unstable growth of oscillations induced by finite pulses is potentially serious in practical rocket motors. During the Apollo program, NASA developed a method of rating the stability of liquid rocket engines by "bombing," i.e., exploding small charges during a firing. A motor is then considered acceptably stable if the decay rate exceeds some chosen value. Liquid rockets may experience pulses, for example, during ignition, changes of thrust level, or if for some reason liquid reactants accumulate in a region and suddenly ignite. A common cause for pulses in solid rockets is expulsion of pieces of an igniter or of insulation material.

Results for nonlinear gasdynamics to second-order have not explained this type of behavior. However, a simple example introduced by Awad [2] gave reason to believe that gasdynamics to a higher order might lead to the possibility of triggering. The phase diagram for a one-degree-of-freedom system suggests [3, 51] that a linearly stable third-order system might produce triggering to stable limit cycles. Motivated by this example, Yang et al. [56, 57, 58], Kim [42], and Paparizos and Culick [52] treated the case of third-order acoustics in an attempt to explain this type of true nonlinear instability. Results for third-order acoustics were found to be qualitatively like those for second-order acoustics, and once again, no cases of triggering were reported.

Although it was not proven explicitly, calculations for a wide range of special cases in the previously mentioned works showed that nonlinear gasdynamics up to third-order does not contain the possibility of triggering. Evidently, some other nonlinear contribution must also be included. Kim [42], Yang et al. [58], and Paparizos and Culick [52] examined mean flow/acoustics interactions as a possible mechanism of triggering. While the mean flow offers a

significant energy source which could possibly sustain such oscillations, the results did not produce cases of stable limit cycles for a linearly stable system.

The interaction of oscillations and combustion processes is a very complicated process. It is likely that this interaction plays an important role in pulsed instabilities. For this reason, the nonlinear response of combustion processes to acoustic perturbations has been investigated as a possible cause of triggering. Kooker and Zinn [43] investigated the role of nonlinear pressure coupling in pulsed oscillations. By solving the equations of motion simultaneously with the equations governing the nonlinear pressure coupled response of the propellant, the effects of large-amplitude disturbances on solid propellant rocket engines were studied. Because this was a numerical investigation, it suffers from the same shortcoming as all numerical works. Each calculation is a special case: extracting qualitative rules of thumb potentially helpful in the design process is a tedious matter. In addition, there is no way with numerical solutions to know rigorously if a limit cycle has been reached.

Motivated by the operational implications of triggered instabilities, the Air Force Rocket Propulsion Laboratory conducted a lengthy experimental and theoretical program over a period of about a decade beginning in the mid-1970s. Baum, Levine and Lovine published the last paper [5] covering that project in 1988; the paper contains a complete list of references to the work. Extensive data were taken for a range of geometries and for three propellants, using either explosive charges or ejected plastic objects to generate pulses.

As part of the effort to understand the observations, Baum and Levine [4, 45] solved the partial differential equations numerically for conditions approximating those in the tests. As described in Section 5.2.1, a simple model of nonlinear combustion response was used, based on the idea of the kinematical nonlinearity associated with velocity coupling.

Although quite satisfactory results were obtained, the authors were well

aware of the deficiencies of using a purely numerical analysis to interpret measurements. It is, for example, difficult to make definite conclusions concerning the relative influences of nonlinear combustion and other processes. Moreover, because the run time of the numerical solutions was limited by practical considerations arising with the computers then available, it is not clear that any of the numerical results definitely represent limit cycles for long times after the pulses. Nonetheless, the results showed convincingly that nonlinear combustion is an essential feature of those pulsed instabilities treated.

Powell et al. [53] used the approximate analysis based on spatial averaging to study instabilities in solid rocket motors and T-burners. Using a heuristic model of pressure coupling, a case of triggering was reported. However, the pressure coupled model does not seem to have a good physical basis. Also, the presentation of results does not easily show whether or not triggering to a stable limit cycle has actually occurred.

Awad [2] and Yang et al. [56] used simple model examples to investigate possible nonlinear combustion response functions. Using models with one and two modes, these works found that "self-coupling" terms can be important in triggering. However, the focus of these works was on identifying what type of terms could be important in triggering rather than on realistic modeling of combustion processes. It is important, yet difficult, to determine if a model is physically realistic.

Gadiot and Gany [29] used the approximate analysis with both spatial and time-averaging to investigate the effects of nonlinear pressure coupling. Cases of triggering were reported, but the results are questionable. A perturbation method was used to derive the approximate analysis which assumed that the amplitudes are small compared to the mean pressure. The amplitudes of the oscillations are much higher than the range of applicability of the perturbation method. Also, it appears that the gas phase was not handled properly in the

development of the pressure coupled response function.

Kim [42] used an ad hoc velocity coupled model along with the two-mode, time-averaged equations. Limited amounts of triggering were found for some ranges of the velocity coupled response function. Greene [32] treated a simpler ad hoc model of velocity coupling, one which turns out to be a subset of the model used by Kim. Both of these analyses failed to determine the effects of the approximations introduced by time-averaging and truncation to two modes. As a result, the reported cases of triggering may be a consequence of truncation to a small number of modes instead of an actual case of triggering. This possibility will be addressed in the current investigation.

The present work uses the approximate analysis developed by Culick to investigate nonlinear combustion instabilities. In particular, it is the purpose of this work to investigate the effects of different nonlinear contributions with emphasis on nonlinear combustion response and noise.

In Chapter 2, we will develop the approximate analysis based on spatial averaging in the form of Galerkin's method. This well-established analysis, introduced by Culick, leads to a set of coupled nonlinear oscillators. Nonlinear contributions from gasdynamics to second-order will be derived. Other nonlinear contributions will be handled in subsequent chapters. The method of time-averaging, as applied by Culick [12], will also be described.

In Chapter 3, the methods of dynamical systems theory will be introduced. These methods have proven to be very useful tools in the study of nonlinear systems of equations and are therefore well suited for the purposes here. Three different continuation methods, applicable to steady states, periodic solutions, and folds, will be discussed. Finally, the nonlinear acoustic equations will be put into a form that can used with these methods.

Many previous investigations have studied the case where gasdynamics provides the only nonlinear contribution, and much progress has been made.

Nonetheless, there are still unanswered questions, and some of these will be addressed in Chapter 4. This chapter will study the effect of the method of time-averaging when a higher number of modes is included. In addition, dynamical systems theory will be applied to the case of transverse modes. The effect of including higher transverse modes will then be determined.

The modeling of nonlinear contributions from combustion processes will be covered in Chapter 5. Several models will be used to investigate the influence of nonlinear combustion on instabilities in solid propellant rocket motors: one which represents coupling to pressure fluctuations at the burning surface, and three which represent coupling to velocity fluctuations. The influence of these models on the behavior of the system of equations will be studied, with emphasis on locating the possibility of pulsed oscillations.

The influence of noise is examined in Chapter 6. First, the unsteady field will be split into acoustic and random parts to determine the form of the stochastic terms, as in the work by Culick et al. [20]. The previous results by Culick et al. will be extended by determining the effects of each type of stochastic excitation, by adding more modes, by including noise in more than one mode, and by treating the case where nonlinear combustion is also taken into account.

Chapter 2

Development of the Nonlinear Acoustic Equations

In general, combustion chambers contain some type of particulate matter such as liquid droplets or condensed solid propellant. The presence of such matter can significantly change the properties of the flow inside the chamber, with the speed of sound being especially affected due to the additional mass of this material. In order to account for these changes, it is necessary to begin with the conservation equations for two-phase flow. Although many gases and condensed species may be present, it is sufficient to treat the gases as one gas with average properties and the condensed species in an average way as a fluid [16]. Following the method developed by Marble [48] and applied by Culick [13] to combustion instabilities, we will further simplify the conservation equations by combining the equations for two-phase flow into an equivalent form for a single medium having the mass-averaged properties of the two phases.

2.1 Conservation Equations

The equations of motion for two-phase flow, allowing for the conversion of particulate material to gas, are as follows.

Conservation of mass (gas):

$$\frac{\partial \rho_g}{\partial t} + \nabla \cdot (\rho_g \boldsymbol{u}) = \omega_p \tag{2.1}$$

Conservation of mass (particles):

$$\frac{\partial \rho_p}{\partial t} + \nabla \cdot (\rho_p \boldsymbol{u}_p) = -\omega_p \tag{2.2}$$

Conservation of momentum:

$$\frac{\partial}{\partial t}(\rho_g \boldsymbol{u} + \rho_p \boldsymbol{u}_p) + \nabla \cdot (\rho_g \boldsymbol{u}\boldsymbol{u} + \rho_p \boldsymbol{u}_p \boldsymbol{u}_p) + \nabla p = \nabla \cdot \overleftrightarrow{\tau} \tag{2.3}$$

Conservation of energy:

$$\frac{\partial}{\partial t}(\rho_g e_0 + \rho_p e_{p0}) + \nabla \cdot (\rho_g \boldsymbol{u} e_0 + \rho_p \boldsymbol{u}_p e_{p0}) + \nabla \cdot (p\boldsymbol{u}) = \nabla \cdot \boldsymbol{q} + Q \tag{2.4}$$

where ω_p is the rate of conversion of particulate material to gas and $\overleftrightarrow{\tau}$ is the viscous stress tensor for the gases. The heat flux vector, $\boldsymbol{q}$, represents the heat transfer by conduction, while Q represents heat released by chemical reactions. It should be noted that ρ_p is the mass of particles per unit volume and not the density of the particulate matter itself.

Many cases of interest involve small accelerations and temperature changes so that the velocities and temperatures of the two phases differ by only a small amount. For these cases, the particles and gases are nearly in equilibrium, and the density ratio, $C_m = \rho_p/\rho_g$, is almost constant throughout the chamber. Marble [49] has shown that for such a case, the mixture behaves like a perfect

gas with proper modification of the thermodynamic properties. As a result, the conservation equations for two phase flow can be rewritten in a form for a single medium with the mass-averaged properties of the two phases. We will now develop the analogous set of conservation equations for the mixture.

The first step in the development of the conservation equations for the mixture is to rewrite the momentum and energy equations for the gas phase only. Simple rearrangement of Eqs. (2.3) and (2.4) yields the following equations for the gas phase.

$$\rho_g \left[\frac{\partial \boldsymbol{u}}{\partial t} + (\boldsymbol{u} \cdot \nabla)\boldsymbol{u} \right] + \nabla p = \nabla \cdot \overleftrightarrow{\tau} - \boldsymbol{\sigma} + \boldsymbol{\mathcal{F}}_p \tag{2.5}$$

$$\rho_g c_v \left[\frac{\partial T}{\partial t} + (\boldsymbol{u} \cdot \nabla)T \right] + p \nabla \cdot \boldsymbol{u} = \nabla \cdot \boldsymbol{q} + Q + Q_p + (e_{p0} - e_0)\omega_p + \boldsymbol{u} \cdot \boldsymbol{\sigma} + \boldsymbol{u} \cdot (\nabla \cdot \overleftrightarrow{\tau}) + (\boldsymbol{u}_p - \boldsymbol{u}) \cdot \boldsymbol{\mathcal{F}}_p \tag{2.6}$$

The variables describing the interaction between particles and gas are defined as follows:

$$\boldsymbol{\sigma} = -(\boldsymbol{u}_p - \boldsymbol{u})\omega_p, \tag{2.7}$$

$$\boldsymbol{\mathcal{F}}_p = -\rho_p \left[\frac{\partial \boldsymbol{u}_p}{\partial t} + (\boldsymbol{u}_p \cdot \nabla)\boldsymbol{u}_p \right], \tag{2.8}$$

$$Q_p = -\rho_p c \left[\frac{\partial T_p}{\partial t} + (\boldsymbol{u}_p \cdot \nabla)T_p \right]. \tag{2.9}$$

where $\boldsymbol{\sigma}$ is the momentum transfer between gas and particles due to residual combustion, and $\boldsymbol{\mathcal{F}}_p$ denotes the force exerted on the fluid by particles. In Eq. (2.6), Q_p is the heat transfer between phases, with c denoting the specific heat of the particulate matter.

The assumption of small accelerations and temperature changes allows us to define two small quantities for the differences in velocity and temperature

between the two phases. By defining $\delta \boldsymbol{u}_p = \boldsymbol{u}_p - \boldsymbol{u}$, we can rewrite the equation for $\boldsymbol{\mathcal{F}}_p$ in terms of the velocity of the gas and the velocity difference.

$$\begin{aligned}\boldsymbol{\mathcal{F}}_p = &-\rho_p \left[\frac{\partial \boldsymbol{u}}{\partial t} + (\boldsymbol{u}\cdot\nabla)\boldsymbol{u}\right] \\ &- \rho_p \left[\frac{\partial \delta\boldsymbol{u}_p}{\partial t} + (\boldsymbol{u}\cdot\nabla)\delta\boldsymbol{u}_p + (\delta\boldsymbol{u}_p\cdot\nabla)\boldsymbol{u} + (\delta\boldsymbol{u}_p\cdot\nabla)\delta\boldsymbol{u}_p\right] \quad (2.10)\end{aligned}$$

Rearranging we obtain

$$\rho_p \left[\frac{\partial \boldsymbol{u}}{\partial t} + (\boldsymbol{u}\cdot\nabla)\boldsymbol{u}\right] = -\boldsymbol{\mathcal{F}}_p + \delta\boldsymbol{\mathcal{F}}_p, \quad (2.11)$$

where the force of particles upon the fluid due to the velocity difference, $\delta\boldsymbol{\mathcal{F}}_p$, has been defined as follows.

$$\delta\boldsymbol{\mathcal{F}}_p = \rho_p \left[\frac{\partial \delta\boldsymbol{u}_p}{\partial t} + (\boldsymbol{u}\cdot\nabla)\delta\boldsymbol{u}_p + (\delta\boldsymbol{u}_p\cdot\nabla)\boldsymbol{u} + (\delta\boldsymbol{u}_p\cdot\nabla)\delta\boldsymbol{u}_p\right] \quad (2.12)$$

Similarly, letting $\delta T_p = T_p - T$ leads to an equivalent equation for the conservation of energy.

$$\rho_p c \left[\frac{\partial T}{\partial t} + (\boldsymbol{u}\cdot\nabla)T\right] = -Q_p + \delta Q_p, \quad (2.13)$$

where

$$\delta Q_p = -\rho_p c \left[\frac{\partial \delta T_p}{\partial t} + (\boldsymbol{u}_p\cdot\nabla)\delta T_p + (\delta\boldsymbol{u}_p\cdot\nabla)T + (\delta\boldsymbol{u}_p\cdot\nabla)\delta T_p\right]. \quad (2.14)$$

Finally, adding Eq. (2.5) to (2.11) and (2.6) to (2.13) yields the momentum and energy equations for the mixture.

$$\rho \left[\frac{\partial \boldsymbol{u}}{\partial t} + (\boldsymbol{u}\cdot\nabla)\boldsymbol{u}\right] + \nabla p = \nabla\cdot\overleftrightarrow{\tau} - \boldsymbol{\sigma} + \delta\boldsymbol{\mathcal{F}}_p \quad (2.15)$$

$$\rho\bar{c}_v\left[\frac{\partial T}{\partial t}+(\boldsymbol{u}\cdot\nabla)T\right]+p\nabla\cdot\boldsymbol{u}=\nabla\cdot\boldsymbol{q}+Q+\delta Q_p$$
$$+(e_{p0}-e_0)\omega_p+\boldsymbol{u}\cdot\boldsymbol{\sigma}-\boldsymbol{u}\cdot(\nabla\cdot\overleftrightarrow{\tau})+\delta\boldsymbol{u}_p\cdot\boldsymbol{\mathcal{F}}_p \quad (2.16)$$

From these equations, we can see that the mixture behaves like a perfect gas with density $\rho=\rho_g+\rho_p$ and the following thermodynamic properties [48].

$$\bar{c}_v=\frac{c_v+C_mc}{1+C_m} \quad (2.17)$$
$$\bar{c}_p=\frac{c_p+C_mc}{1+C_m} \quad (2.18)$$
$$\bar{R}_0=\frac{R_0}{1+C_m} \quad (2.19)$$
$$\bar{\gamma}=\frac{\bar{c}_p}{\bar{c}_v} \quad (2.20)$$

Using these new properties, the proper speed of sound for the mixture is

$$\bar{a}=\sqrt{\bar{\gamma}\bar{R}_0T}=\left[\frac{\bar{\gamma}}{1+C_m}\frac{p}{\rho_g}\right]^{1/2}. \quad (2.21)$$

Depending on the mass fraction of particles, the speed of sound for the mixture can be significantly reduced from the speed of sound for the gas alone.

In the development of the approximate analysis, it is convenient to use pressure instead of temperature. Using the mass and energy equations for the mixture along with the appropriate equation of state, $p=\rho\bar{R}_0T$, we will rewrite the energy equation with the pressure as the dependent variable.

$$\frac{\partial p}{\partial t}+(\boldsymbol{u}\cdot\nabla)p=-\bar{\gamma}p\nabla\cdot\boldsymbol{u}+(\bar{\gamma}-1)[\nabla\cdot\boldsymbol{q}+Q+\delta Q_p+(e_{p0}-e_0)\omega_p$$
$$+\boldsymbol{u}\cdot\boldsymbol{\sigma}-\boldsymbol{u}\cdot(\nabla\cdot\overleftrightarrow{\tau})+\delta\boldsymbol{u}_p\cdot\boldsymbol{\mathcal{F}}_p-\bar{c}_vT\nabla\cdot(\rho_p\delta\boldsymbol{u}_p)] \quad (2.22)$$

The present goal is to develop a general framework for the approximate analysis. We are not currently concerned with the forms of the source terms

on the right-hand sides. Therefore, we will now assemble and rewrite the conservation equations for the mixture in a more illustrative form, partly in preparation for the development of the nonlinear wave equation in the next section.

$$\text{mass}: \quad \frac{\partial \rho}{\partial t} + (\boldsymbol{u} \cdot \nabla)\rho = \mathcal{W} \tag{2.23}$$

$$\text{momentum}: \quad \rho\left[\frac{\partial \boldsymbol{u}}{\partial t} + (\boldsymbol{u} \cdot \nabla)\boldsymbol{u}\right] = -\nabla p + \boldsymbol{\mathcal{F}} \tag{2.24}$$

$$\text{energy}: \quad \frac{\partial p}{\partial t} + \bar{\gamma} p \nabla \cdot \boldsymbol{u} = -\boldsymbol{u} \cdot \nabla p + \mathcal{P}, \tag{2.25}$$

where

$$\mathcal{W} = -\rho \nabla \cdot \boldsymbol{u} - \nabla \cdot (\rho_p \delta \boldsymbol{u}_p), \tag{2.26}$$

$$\boldsymbol{\mathcal{F}} = \nabla \cdot \overleftrightarrow{\tau} - \boldsymbol{\sigma} + \delta \boldsymbol{\mathcal{F}}_p, \tag{2.27}$$

$$\begin{aligned} \mathcal{P} = (\bar{\gamma} - 1)[&\nabla \cdot \boldsymbol{q} + Q + \delta Q_p + (e_{p0} - e_0)\omega_p + \boldsymbol{u} \cdot \boldsymbol{\sigma} \\ &- \boldsymbol{u} \cdot (\nabla \cdot \overleftrightarrow{\tau}) + \delta \boldsymbol{u}_p \cdot \boldsymbol{\mathcal{F}}_p - \bar{c}_v T \nabla \cdot (\rho_p \delta \boldsymbol{u}_p)]. \end{aligned} \tag{2.28}$$

2.2 Derivation of the Nonlinear Wave Equation

The conservation equations for the mixture are the equations used in the study of acoustics with some additional terms. This is not coincidental and stresses the opinion that combustion instabilities are best viewed as perturbations of classical acoustics [15]. Therefore, as the first step in the development of the approximate analysis, we will derive the nonlinear wave equation for pressure.

To construct the nonlinear wave equation, we first write all variables as

sums of averaged and small-amplitude fluctuating parts [13].

$$\begin{aligned} p(t) &= \bar{p} + p'(t) \\ \rho(\boldsymbol{r},t) &= \bar{\rho}(\boldsymbol{r}) + \rho'(\boldsymbol{r},t) \\ \boldsymbol{u}(\boldsymbol{r},t) &= \bar{\boldsymbol{u}}(\boldsymbol{r}) + \boldsymbol{u}'(\boldsymbol{r},t) \end{aligned} \tag{2.29}$$

It is assumed here that the averaged values are independent of time and satisfy their own conservation equations. Substitution of Eq. (2.29) into the conservation equations for momentum and energy yields the following equations for the fluctuating quantities.

$$\begin{aligned} \bar{\rho}\frac{\partial \boldsymbol{u}'}{\partial t} + \nabla p' = -\rho'\frac{\partial \boldsymbol{u}'}{\partial t} - \bar{\rho}(\bar{\boldsymbol{u}}\cdot\nabla\boldsymbol{u}' + \boldsymbol{u}'\cdot\nabla\bar{\boldsymbol{u}} + \boldsymbol{u}'\cdot\nabla\boldsymbol{u}') \\ - \rho'(\bar{\boldsymbol{u}}\cdot\nabla\bar{\boldsymbol{u}} + \bar{\boldsymbol{u}}\cdot\nabla\boldsymbol{u}' + \boldsymbol{u}'\cdot\nabla\bar{\boldsymbol{u}}) + \boldsymbol{\mathcal{F}}' \end{aligned} \tag{2.30}$$

$$\frac{\partial p'}{\partial t} + \bar{\gamma}\bar{p}\nabla\cdot\boldsymbol{u}' = -\bar{\gamma}p'\nabla\cdot\bar{\boldsymbol{u}} - \bar{\gamma}p'\nabla\cdot\boldsymbol{u}' - \bar{\boldsymbol{u}}\cdot\nabla p' - \boldsymbol{u}'\cdot\nabla\bar{p} - \boldsymbol{u}'\cdot\nabla p' + \mathcal{P}' \tag{2.31}$$

Previous results have convincingly demonstrated that the influence of third-order gasdynamic terms is almost always quite small [56, 57, 52]. Third-order gasdynamic terms appear to affect the quantitative values of results only slightly, while producing the same qualitative behavior as results obtained using only second-order terms. Therefore, in the above equations, only terms to second-order in perturbations have been retained.

From Eqs. (2.30) and (2.31), the nonlinear wave equation for pressure is easily formed. This is achieved by first differentiating Eq. (2.31) with respect

to time, followed by substitution for $\partial \boldsymbol{u}'/\partial t$ from Eq. (2.30).

$$\begin{aligned}\nabla^2 p' - \frac{1}{\bar{a}^2}\frac{\partial^2 p'}{\partial t^2} = \\ - \bar{\rho}\nabla\cdot\left\{\bar{\boldsymbol{u}}\cdot\nabla\boldsymbol{u}' + \boldsymbol{u}'\cdot\nabla\bar{\boldsymbol{u}} + \boldsymbol{u}'\cdot\nabla\boldsymbol{u}' + \frac{\rho'}{\bar{\rho}}\frac{\partial \boldsymbol{u}'}{\partial t}\right\} + \frac{\bar{\gamma}}{\bar{a}^2}\frac{\partial p'}{\partial t}\nabla\cdot\bar{\boldsymbol{u}} \\ + \frac{1}{\bar{a}^2}\bar{\boldsymbol{u}}\cdot\nabla\frac{\partial p'}{\partial t} + \frac{1}{\bar{a}^2}\frac{\partial}{\partial t}(\boldsymbol{u}'\cdot\nabla p' + \bar{\gamma}p'\nabla\cdot\boldsymbol{u}') + \frac{1}{\bar{a}^2}\frac{\partial \mathcal{P}'}{\partial t} + \nabla\cdot\boldsymbol{\mathcal{F}}' \quad (2.32)\end{aligned}$$

In obtaining this equation, we have assumed that the average pressure is uniform throughout the chamber, which is equivalent to assuming that the average Mach number is small. Under this assumption, terms which are second-order in $\bar{\boldsymbol{u}}$ are ignored.

In many cases, entropy waves can be neglected, allowing a reduction in the number of dependent variables. Using the isentropic relation, $p = C\rho^{\bar{\gamma}}$, with Eq. (2.29) leads to the following approximation for ρ', thus reducing the number of dependent variables.

$$\rho' \approx \frac{p'}{\bar{a}^2} \quad (2.33)$$

Introducing this approximation into Eq. (2.32) gives the following formula for the nonlinear wave equation for the pressure.

$$\nabla^2 p' - \frac{1}{\bar{a}^2}\frac{\partial^2 p'}{\partial t^2} = h, \quad (2.34)$$

where

$$\begin{aligned}h = &- \bar{\rho}\nabla\cdot(\bar{\boldsymbol{u}}\cdot\nabla\boldsymbol{u}' + \boldsymbol{u}'\cdot\nabla\bar{\boldsymbol{u}}) + \frac{1}{\bar{a}^2}\bar{\boldsymbol{u}}\cdot\nabla\frac{\partial p'}{\partial t} + \frac{\bar{\gamma}}{\bar{a}^2}\frac{\partial p'}{\partial t}\nabla\cdot\bar{\boldsymbol{u}} \quad (2.35) \\ &- \bar{\rho}\nabla\cdot\left(\boldsymbol{u}'\cdot\nabla\boldsymbol{u}' + \frac{p'}{\bar{\gamma}\bar{p}}\frac{\partial \boldsymbol{u}'}{\partial t}\right) + \frac{1}{\bar{a}^2}\frac{\partial}{\partial t}(\boldsymbol{u}'\cdot\nabla p') + \frac{\bar{\gamma}}{\bar{a}^2}\frac{\partial}{\partial t}(p'\nabla\cdot\boldsymbol{u}') \\ &+ \nabla\cdot\boldsymbol{\mathcal{F}}' - \frac{1}{\bar{a}^2}\frac{\partial \mathcal{P}'}{\partial t}.\end{aligned}$$

The corresponding boundary condition for p' is found by taking the scalar product of the outward normal vector with the momentum equation (2.30).

$$\hat{\boldsymbol{n}} \cdot \nabla p' = -f, \tag{2.36}$$

with

$$\begin{aligned} f = & \bar{\rho} \frac{\partial \boldsymbol{u}'}{\partial t} \cdot \hat{\boldsymbol{n}} + \bar{\rho}(\bar{\boldsymbol{u}} \cdot \nabla \boldsymbol{u}' + \boldsymbol{u}' \cdot \nabla \bar{\boldsymbol{u}}) \cdot \hat{\boldsymbol{n}} \\ & + \bar{\rho}(\boldsymbol{u}' \cdot \nabla \boldsymbol{u}') \cdot \hat{\boldsymbol{n}} + \frac{p'}{\bar{a}^2} \frac{\partial \boldsymbol{u}'}{\partial t} \cdot \hat{\boldsymbol{n}} - \boldsymbol{\mathcal{F}}' \cdot \hat{\boldsymbol{n}}. \end{aligned} \tag{2.37}$$

2.3 Development of the Approximate Analysis

The idea behind the approximate analysis is to transform the partial differential equations into an equivalent set of ordinary differential equations. This is achieved by averaging over the volume of the chamber using Galerkin's method [12, 13]. This removes the spatial dependence, leaving a system of ordinary differential equations with time as the independent variable.

The application of Galerkin's method consists of multiplying the nonlinear wave equation by an appropriate weighting function, then integrating over the volume. Here, the weighting function is chosen to be the unperturbed wave form predicted by classical acoustics for the same chamber with rigid boundaries and no combustion or mean flow. This is a sufficient choice for the cases under consideration, but for other cases of interest, it may not be suitable. By setting $h = f = 0$, we obtain the equations which define the

mode shapes for the unperturbed motions.

$$\nabla^2\psi_n + k_n^2\psi_n = 0 \tag{2.38}$$

$$\hat{\boldsymbol{n}} \cdot \nabla\psi_n = 0 \tag{2.39}$$

The wave number for the n_{th} mode is denoted by k_n. Using the mode shape ψ_n as the weighting function, we now apply Galerkin's method, which amounts to comparing the unperturbed problem with the actual problem. The steps consist of multiplying Eq. (2.34) by ψ_n, multiplying Eq. (2.38) by p', subtracting the results, and integrating over the volume.

$$\int \left[p'\nabla^2\psi_n - \psi_n\nabla^2 p'\right] dV + \frac{1}{\bar{a}^2}\int \psi_n \frac{\partial^2 p'}{\partial t^2} dV + k_n^2 \int \psi_n p' dV = -\int \psi_n h dV \tag{2.40}$$

After applying Greene's theorem to the first term on the left-hand side and subsequently substituting for the boundary conditions, we are left with an integral equation for the pressure fluctuation.

$$\frac{1}{\bar{a}^2}\int \psi_n \frac{\partial^2 p'}{\partial t^2} dV + k_n^2 \int \psi_n p' dV = -\int \psi_n h dV - \oint \psi_n f dS \tag{2.41}$$

Now we would like to develop an approximation to the unsteady pressure field for use in the above equation. We assume that the classical modes shapes defined by Eqs. (2.38) and (2.39) form a complete orthogonal set. Using these mode shapes as a basis, the unsteady pressure field is written as a synthesis of classical modes with time-varying amplitudes $\eta_m(t)$.

$$p'(\boldsymbol{r}, t) = \bar{p}\sum_{m=1}^{\infty} \eta_m(t)\psi_m(\boldsymbol{r}) \tag{2.42}$$

The terms in h and f are all small, being either second-order in perturbations,

or first-order multiplied by a small quantity, e.g., the Mach number of the mean flow. Hence, as approximations in h and f, we will use p' from Eq. (2.42), along with the corresponding velocity from classical acoustics,

$$\boldsymbol{u}'(\boldsymbol{r},t) = \sum_{m=1}^{\infty} \frac{\dot{\eta}_m(t)}{\bar{\gamma} k_m^2} \nabla \psi_m(\boldsymbol{r}). \tag{2.43}$$

We assume that the unperturbed modes are orthogonal so that the following properties hold.

$$\int \psi_m \psi_n dV = E_n^2 \delta_{mn} \tag{2.44}$$

$$E_n^2 \equiv \int \psi_n^2 dV \tag{2.45}$$

Substituting Eqs. (2.42) and (2.43) into (2.41) and using these properties, we obtain a system of second-order ordinary differential equations describing the amplitudes of the acoustic modes.

$$\frac{d^2\eta_n}{dt^2} + \omega_n^2 \eta_n = F_n, \tag{2.46}$$

where $\omega_n = \bar{a} k_n$ and

$$F_n = -\frac{\bar{a}^2}{\bar{p} E_n^2} \left\{ \int \psi_n h dV + \oint \psi_n f dS \right\}. \tag{2.47}$$

Equation (2.46) describes the unsteady motions of a set of coupled nonlinear oscillators. In order to solve for the amplitudes η_n, it is first necessary to evaluate h and f. These functionals are very general and can accommodate all damping and amplification mechanisms, e.g., viscous losses, particle damping, and combustion response. The most difficult part of the problem is in the identification and modeling of the physical processes which are important in the system of interest.

It should be noted that several assumptions have been made in the development of Eq. 2.46. While these assumptions may limit the range of applicability somewhat, the approximate analysis is still useful for a wide range of cases of practical interest and has provided much insight into combustion instabilities in the past, as well as in the present study. In Chapter 6, two of these assumptions, namely neglecting vorticity and entropy waves, will be relaxed.

2.4 Equations for Computing the Time-Dependent Pressure Field

The set of coupled nonlinear equations (2.46) are the basis for the numerical results in much of the present analysis. To carry out the calculations, the forcing functions F_n must be written explicitly in terms of the amplitudes η_n. That result is accomplished by using the expansions (2.42) and (2.43) as an approximation to p' and $\boldsymbol{u}'$ in h and f.

Because the procedure for evaluating the integrals arising from the linear and nonlinear gasdynamics has been previously documented in several places [21, 13, 42], only the important aspects will be discussed here. First, all linear processes, those arising from the gasdynamics and any others generated from $\mathcal{P}'$ and $\boldsymbol{\mathcal{F}}'$, will produce the terms $2\alpha_n\dot{\eta}_n + 2\omega_n\theta_n\eta_n$ in the n^{th} equation of the set (2.46). In general, linear coupling will also be present; from the gasdynamics alone, one finds the off-diagonal terms

$$\frac{\bar{\rho}}{\bar{\gamma}}\sum_{j\neq n}\dot{\eta}_j\left(\frac{k_n^2}{k_j^2}+1\right)\int(\bar{\boldsymbol{u}}\cdot\nabla\psi_j)\psi_n dV. \tag{2.48}$$

In principle, linear coupling can be eliminated by defining a new set of orthogonal modes by applying familiar methods. For example, in the case of

two modes, the governing linear equations are

$$\frac{d^2\eta_1}{dt^2} - 2\alpha_1\dot{\eta}_1 + \Omega_1^2\eta_1 = a_{12}\dot{\eta}_2, \tag{2.49}$$

$$\frac{d^2\eta_2}{dt^2} - 2\alpha_2\dot{\eta}_2 + \Omega_2^2\eta_2 = a_{21}\dot{\eta}_1, \tag{2.50}$$

where $\Omega_i^2 = \omega_i^2 - 2\omega_i\theta_i$ and $a_{12} \neq a_{21}$ are constants. The characteristic equation, whose roots λ_i are the new eigenvalues for the uncoupled modes, is

$$\lambda^4 - 2(\alpha_1 + \alpha_2)\lambda^3 + (\Omega_1^2 + \Omega_2^2 + 4\alpha_1\alpha_2 - a_{12}a_{21})\lambda^2 + (\Omega_1^2 + \Omega_2^2)\lambda + \Omega_1^2\Omega_2^2 = 0. \tag{2.51}$$

If there is no coupling ($a_{12}a_{21} = 0$) the roots of this equation are Ω_1^2 and Ω_2^2 shifted by the perturbations represented by α_i. Those values are then perturbed by an amount proportional to $a_{12}a_{21}$ when coupling is present. But $a_{12}a_{21}$ is proportional to the square of a characteristic Mach number $\bar{M}_r$ of the mean flow. Thus $a_{12}a_{21}$ is small and a simple perturbation expansion of Eq. (2.51) will show that the roots are shifted by amounts proportional to $a_{12}a_{21} \sim \bar{M}_r^2$.

However, it is assumed in this study that terms of order $\bar{M}_r^2$ and higher can be dropped. Hence the effects of linear coupling, being of order $\bar{M}_r^2$, must be dropped. It is of course possible that other sorts of linear coupling might arise from $\mathcal{F}'$ and $\mathcal{P}'$, but we will assume that those too are negligible. Hence the system (2.46) has the form

$$\ddot{\eta}_n + \omega_n^2\eta_n = 2\alpha_n\dot{\eta}_n + 2\omega_n\theta_n\eta_n + (F_n)_{\text{nonlinear}}, \tag{2.52}$$

where the last term contains all nonlinear processes.

We will ignore nonlinear contributions from $\mathcal{F}'$ and $\mathcal{P}'$. If also we continue the practice followed in the previous works using this method and drop terms

of order $\bar{M}_r(M_r')^2$ where M_r' is a characteristic Mach number for the unsteady flow, then the gasdynamics to second-order lead eventually to [13]

$$(F_n)^{\mathrm{GD}}_{\mathrm{nonlinear}} = -\sum_{i=1}^{\infty}\sum_{j=1}^{\infty}[A_{nij}\dot{\eta}_i\dot{\eta}_j + B_{nij}\eta_i\eta_j], \tag{2.53}$$

where

$$A_{nij} = \frac{1}{E_n^2}\int\left\{\frac{1}{\bar{\gamma}k_i^2}(\nabla\psi_i\cdot\nabla\psi_j + \bar{\gamma}\psi_j\nabla^2\psi_i)\psi_n \right. \\ \left. + \frac{1}{\bar{\gamma}k_i^2k_j^2}[(\nabla\psi_i\cdot\nabla)\nabla\psi_j]\cdot\nabla\psi_n\right\}dV, \tag{2.54}$$

$$B_{nij} = -\frac{1}{E_n^2}\int\frac{\bar{a}^2}{\bar{\gamma}}[(\nabla\psi_i\cdot\nabla\psi_j + \bar{\gamma}\psi_i\nabla^2\psi_j)\psi_n + \psi_i\nabla\psi_j\cdot\nabla\psi_n]dV. \tag{2.55}$$

The analysis as developed so far is very general. It can be applied to a chamber of arbitrary geometry. However, the special case of a cylindrical chamber is often of interest when dealing with rocket motors. We will therefore restrict the investigation to the case of a cylindrical chamber of radius R and length L. For this case, the mode shapes are given by

$$\psi_n(\boldsymbol{r}) = \cos k_l x J_m(\kappa_{ms}r)\begin{cases}\cos m\theta \\ \sin m\theta,\end{cases} \tag{2.56}$$

with the wave number of the n_{th} mode defined as

$$k_n^2 \equiv k_l^2 + \kappa_{ms}^2.$$

The eigenvalues k_l are $l\pi/L$, while the values of κ_{ms} are found by solving for

the roots of the derivative of the Bessel function.

$$\left.\frac{dJ_m(\kappa_{ms}r)}{dr}\right|_{r=R} = 0 \tag{2.57}$$

2.5 The Method of Time-Averaging

In previous work based on the approximate analysis, considerable use has been made of the first-order equations produced by time-averaging Eq. (2.46), beginning with Culick [12, 13]. The idea is that in many applications, the oscillations have slowly varying amplitudes and phase: only small fractional changes occur during one period of the fundamental mode. For this type of oscillation, the method of time-averaging developed by Krylov and Bogoliubov [44] allows the system of second-order equations to be transformed into a simpler system of first-order equations.

For an oscillation with slowly varying amplitude and phase, it is reasonable to write the amplitude η_n in the following form.

$$\eta_n(t) = r_n(t)\sin\left(\omega_n t + \phi_n(t)\right) = A_n(t)\sin\omega_n t + B_n(t)\cos\omega_n t \tag{2.58}$$

where $r_n(t)$, $\phi_n(t)$, $A_n(t)$, and $B_n(t)$ are assumed to be slowly varying functions of time. Using this representation, the velocity of the oscillator becomes

$$\dot{\eta}_n(t) = A_n\omega_n\cos\omega_n t - B_n\omega_n\sin\omega_n t + [\dot{A}_n\sin\omega_n t + \dot{B}_n\cos\omega_n t]. \tag{2.59}$$

Assuming that the amplitudes are slowly varying functions of time implies that

$$\dot{A}_n\tau_1 << 1, \tag{2.60}$$

$$\dot{B}_n\tau_1 << 1. \tag{2.61}$$

The above inequalities indicate that the bracketed terms in Eq. (2.59) are negligible compared with the first two terms. In fact, since we have introduced two functions in place of η_n, we have the freedom to impose an additional constraint on A_n and B_n, and we require that [9]

$$\dot{A}_n \sin \omega_n t + \dot{B}_n \cos \omega_n t = 0. \tag{2.62}$$

Upon substituting Eq. (2.58) in (2.46), applying the above constraint, and averaging over one period of the fundamental mode, we obtain a system of first-order differential equations for the amplitudes A_n and B_n.

$$\frac{dA_n}{dt} = \frac{1}{\omega_n \tau_1} \int_t^{t+\tau_1} F_n \cos \omega_n t' dt' \tag{2.63}$$

$$\frac{dB_n}{dt} = -\frac{1}{\omega_n \tau_1} \int_t^{t+\tau_1} F_n \sin \omega_n t' dt' \tag{2.64}$$

When the integrals are carried out, A_n and B_n appearing in F_n are treated as constants since they vary little in the time τ_1 of integration.

This form of the time-averaged equations has been used extensively in the past. When applying the methods of dynamical systems theory, however, it will be more efficient to use the variables r_n and ϕ_n. Performing the same procedure above with the variables r_n and ϕ_n leads to the following time-averaged equations.

$$\frac{dr_n}{dt} = \frac{1}{\omega_n \tau_1} \int_t^{t+\tau_1} F_n \cos(\omega_n t' + \phi_n) dt' \tag{2.65}$$

$$r_n \frac{d\phi_n}{dt} = -\frac{1}{\omega_n \tau_1} \int_t^{t+\tau_1} F_n \sin(\omega_n t' + \phi_n) dt' \tag{2.66}$$

Substantial progress has been made using the time-averaged equations, especially when used in conjunction with truncation to two modes. As mentioned in Chapter 1, analytic solutions are obtained for a limited number of

cases, a significant accomplishment given the complexity of the original problem [51, 17]. Time-averaging and truncation to a small number of modes can change the behavior of the solutions, however, and results must be compared to the results obtained for the original oscillator equations. One way of checking these approximations is through the use of dynamical systems theory covered in the next chapter. In Chapter 4, we will use this theory to explore the validity of the time-averaged equations.

Chapter 3

Dynamical Systems Theory

Numerical simulations, such as those shown in Figs. 1.1–1.3, provide detailed information for one specific set of parameters and initial conditions. Each run is a special case, and it is an expensive and tedious process to obtain general trends. A better way to study the behavior of a system of nonlinear equations is through the use of dynamical systems theory.

Dynamical systems theory has proven to be a very useful tool in the study of systems of ordinary differential equations. Although this theory has been used extensively in other fields, it has only recently been applied to the study of nonlinear combustion instabilities, first by Jahnke and Culick [38]. When applied to the system of equations derived in the approximate analysis, dynamical systems theory provides a systematic approach for determining general trends. For instance, regions of possible triggering can easily be located using the tools of dynamical systems theory.

In particular, the methods of dynamical systems theory can be used to create bifurcation diagrams which provide a visual representation of nonlinear equations by plotting the equilibrium points of a system as a function of one parameter. For a given value of this parameter, a bifurcation diagram shows all possible states of the system and the stability of these states. This is best illustrated by looking at two sample diagrams which correspond to the

simulations in Figs. 1.1–1.3.

The bifurcation diagram in Fig. 3.1 corresponds to the spontaneous oscillation of Fig. 1.1. All modes except the first acoustic mode are linearly stable. Therefore, when the linear growth rate of the first mode is negative, i.e., $\alpha_1 < 0$, the system is linearly stable, and when it is positive, the system is linearly unstable. From this diagram, we see that for a positive value of α_1, there are two equilibrium points; one unstable steady state and one stable limit cycle (for clarity, only the maximum value attained in limit cycle is plotted). Since the steady state is unstable, any perturbation from it will be attracted to the periodic solution.

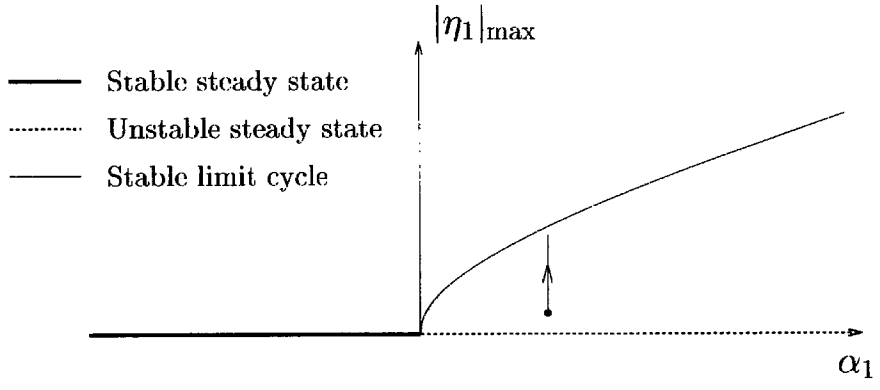

Figure 3.1 Example of a supercritical bifurcation, characteristic of a spontaneous oscillation

In the case of a pulsed oscillation, the system is linearly stable, so α_1 must be negative. Figure 3.2 corresponds to the pulsed oscillation shown in Figs. 1.2 and 1.3. For the chosen value of α_1, there are now three equilibrium points; a stable steady state, an unstable limit cycle, and a stable limit cycle. Depending on the initial conditions, the system can be drawn to either of the stable solutions, as illustrated in Fig. 3.2 for two different initial pulses. For a one-dimensional system, the branch of unstable limit cycles represents the boundary between the region of attraction of the steady state and the region

of attraction of the limit cycle. However, for a multi-dimensional system, it is not so simple. The regions of attraction depend on the initial conditions in all modes, not just the mode pictured in the diagram. This will be demonstrated in Sec. 5.3.3 for several different rectangular pulses.

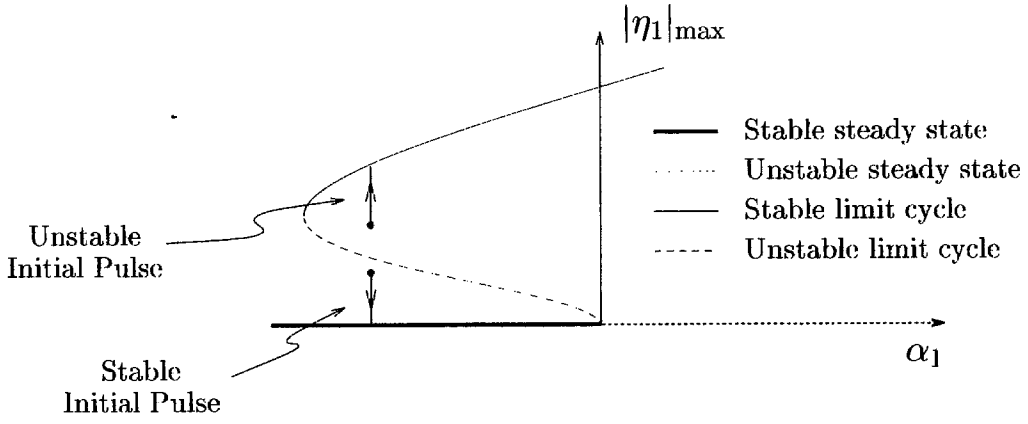

Figure 3.2 Example of a subcritical bifurcation corresponding to the simulations in Figs. 1.2 and 1.3

The previous bifurcation diagrams were generated through the use of local continuation methods. Using these methods, steady states and periodic solutions may be traced as functions of a free parameter of the system, thus allowing the global behavior of the system to be determined. In addition, two-parameter continuations can be used to track loci of turning points, or folds. Continuation methods and their application to the nonlinear acoustic equations will be described in the following sections.

3.1 Calculation of Steady States

The nonlinear acoustic equations (2.46) comprise an autonomous system of ordinary differential equations. The general form of such a system is

$$\frac{d\boldsymbol{x}}{dt} = F(\boldsymbol{x}, \mu), \tag{3.1}$$

where $\boldsymbol{x}$ is the set of unknowns and μ is a parameter of the system. Systems with higher-order time derivatives can always be put into this form by a suitable change of variables. The change of variables for the acoustic equations (2.46) will be introduced in Sec. 3.5.

The usual starting point in the analysis of a nonlinear system of the form (3.1) is to calculate the steady states of the system and determine the local stability of these states. The steady states are found by setting all time derivatives in Eq. (3.1) to zero and solving the resulting set of equations,

$$F(\boldsymbol{x}, \mu) = 0. \tag{3.2}$$

There are many methods, e.g., Newton's method, which can be used to solve for the zeros of this function, but it is not always a trivial step for a general nonlinear system. For our purposes, determination of the steady states of Eq. 2.46 is of little concern since the only physically realistic steady state is the trivial one, $\eta_n = 0$ for all n. Of greater importance is whether or not this steady state is linearly stable or unstable, i.e., what is the local stability of these steady states?

The local stability of a steady state of a nonlinear system can be determined using the Hartman-Grobman linearization theorem [33, page 13]. This theorem proves that the local stability is determined by the eigenvalues of the Jacobian matrix of the linearized system. Let $\boldsymbol{x} = \bar{\boldsymbol{x}} + \delta\boldsymbol{x}$, where $\bar{\boldsymbol{x}}$ is a steady

state found by solving Eq. (3.2) and $\delta \boldsymbol{x} \ll 1$. Using a Taylor series expansion, the system can then be linearized about the steady state $\bar{\boldsymbol{x}}$. The linearized system is given by

$$\delta \dot{\boldsymbol{x}} = F_{\boldsymbol{x}}(\bar{\boldsymbol{x}}, \mu)\delta \boldsymbol{x}, \tag{3.3}$$

where $F_{\boldsymbol{x}}(\bar{\boldsymbol{x}}, \mu)$ is the Jacobian of the function $F(\boldsymbol{x}, \mu)$ evaluated at $\bar{\boldsymbol{x}}$. According to the Hartman-Grobman theorem, if no eigenvalues of $F_{\boldsymbol{x}}(\bar{\boldsymbol{x}}, \mu)$ have positive real parts, then the steady state is locally stable. If any of the real parts of the eigenvalues are positive, then the steady state is locally unstable. When one or more eigenvalues have a zero real part, the stability of the system can change and lead to a qualitatively different behavior of the system. Points where the stability of the system changes are known as bifurcation points.

Many different types of bifurcations can occur in a nonlinear system, although only three types are commonly found in our analysis. The type of bifurcation is determined by the number of eigenvalues with zero real parts. A *pitchfork bifurcation* occurs when one real eigenvalue is equal to zero and $F_{\mu}(\bar{\boldsymbol{x}}, \mu) = 0$. Two additional branches of steady states are created or destroyed at a pitchfork bifurcation, as the name implies. A *turning point bifurcation*, or *fold*, is characterized by $F_{\mu}(\bar{\boldsymbol{x}}, \mu) \neq 0$ and a change in sign of $d\mu(\boldsymbol{x})/d\boldsymbol{x}$. By the factorization theorem, a change in stability of solutions takes place when $d\mu(\boldsymbol{x})/d\boldsymbol{x}$ changes sign [36, page 22].

Perhaps the most important bifurcation in the study of combustion instabilities is the *Hopf bifurcation*, which occurs when a pair of purely imaginary eigenvalues exist [1, page 212]. At a Hopf bifurcation, a branch of periodic solutions is created. The branch of periodic solutions produced at a Hopf bifurcation may be either stable or unstable, as demonstrated in Figs. 3.1 and 3.2. If the branch of periodic solutions is initially stable (a fold or other bifurcation may later change the stability), the bifurcation is said to be *su-*

percritical. If it is initially unstable, the branch is said to be *subcritical.* As Fig. 3.2 demonstrates, the combination of a subcritical bifurcation followed by a fold in the branch leads to the possibility of triggering. Therefore, subcritical bifurcations are important in the study of pulsed oscillations.

3.2 Continuation of Steady States

From a known steady state $(\boldsymbol{x}_o, \mu_o)$, it is possible to calculate a nearby steady state $(\boldsymbol{x}_o + \delta\boldsymbol{x}, \mu_o + \delta\mu)$ using a local continuation method. The basis for such a continuation method is the implicit function theorem [36, page 13]. This theorem proves that for a continuously differentiable system, the steady states are continuous functions of the parameters of the system. Therefore, solutions of Eq. (3.2) are continuous functions of the parameter μ, so long as $F(\boldsymbol{x}, \mu)$ is sufficiently smooth.

The current investigation uses the package AUTO by Doedel [26, 27] to perform continuations of stationary states, i.e., steady states and periodic orbits. The general method as applied to steady states will be outlined in this section. Many of the details are omitted here since the continuation method is simply a tool used to study the system; see Doedel et al. [24, 25] and Keller [41] for more details on the continuation method, and Jahnke and Culick [37] for application to the nonlinear acoustic equations.

One way of calculating solutions along a branch of steady states is to use μ as the continuation parameter. However, with this choice, the continuation method breaks down when a fold is encountered [41, page 74]. To avoid this shortcoming, AUTO uses the pseudoarclength continuation technique developed by Keller [40]. First, a new parameter s is defined which represents the arclength along the branch of steady states. Both $\boldsymbol{x}$ and μ are considered to

be unknown functions of s. Therefore, we are now seeking solutions to

$$F(\boldsymbol{x}(s), \mu(s)) = 0. \tag{3.4}$$

By making μ an unknown, we have increased the number of unknowns by one. To close the system, we require that

$$(\boldsymbol{x}')^2 + (\mu')^2 = 1, \tag{3.5}$$

where

$$\boldsymbol{x}' = \frac{d\boldsymbol{x}}{ds},$$
$$\mu' = \frac{d\mu}{ds}.$$

The slope of the branch can be determined by taking the derivative of $F(\boldsymbol{x}(s), \mu(s))$ with respect to s. Using the chain rule, we obtain

$$F_{\boldsymbol{x}}\boldsymbol{x}' + F_{\mu}\mu' = 0. \tag{3.6}$$

However, calculating the slope in this manner requires the inversion of the matrix $(F_{\boldsymbol{x}} \; — \; F_{\mu})$, a numerically expensive calculation. A less expensive procedure can be used when two steady states, e.g., $(\boldsymbol{x}_0, \mu_0)$ and $(\boldsymbol{x}_1, \mu_1)$, are known. In this case, AUTO approximates the above derivatives by the following formulas.

$$\boldsymbol{x}_1' = \frac{(\boldsymbol{x}_1 - \boldsymbol{x}_0)}{\Delta s} \tag{3.7}$$

$$\mu_1' = \frac{(\mu_1 - \mu_0)}{\Delta s} \tag{3.8}$$

It is also useful to approximate Eq. (3.5) by

$$(\boldsymbol{x} - \boldsymbol{x}_1)\boldsymbol{x}_1' + (\mu - \mu_1)\mu_1' - \Delta s = 0. \tag{3.9}$$

The computational process then consists of the following steps [37].

- Approximate $\boldsymbol{x}'$ and μ' at the previous steady state using Eqs. (3.7) and (3.8).
- Calculate an approximation to the new steady state using $\boldsymbol{x} = \boldsymbol{x}_1 + \boldsymbol{x}_1'\Delta s$ and $\mu = \mu_1 + \mu_1'\Delta s$.
- Reduce the error between the approximate steady state and the actual steady state to an acceptable level using Newton's method in the following way.

$$\boldsymbol{x}_{i+1} = \boldsymbol{x}_i - F_{\boldsymbol{x}}^{-1}(\boldsymbol{x}_i, \mu_1)F(\boldsymbol{x}_i, \mu_1) \tag{3.10}$$

In order to determine the stability of the steady states and find bifurcations of the system, the eigenvalues of the Jacobian are also computed at each step. When a bifurcation is found, AUTO allows branch-switching in order to calculate solutions along any new branches.

3.3 Continuation of Periodic Solutions

A periodic solution of Eq. (3.1) is found by solving

$$\begin{aligned} \dot{\boldsymbol{x}} - \tau F(\boldsymbol{x}(t), \mu) &= 0, \\ \boldsymbol{x}(0) - \boldsymbol{x}(1) &= 0, \end{aligned} \tag{3.11}$$

where time has been rescaled by τ, the period of the orbit. The system (3.11) is not unique since if $\tilde{\boldsymbol{x}}(t)$ is a solution, then $\tilde{\boldsymbol{x}}(t+\sigma)$ is also a solution. This arbitrary phase shift can be removed by minimizing the function [26]

$$g(\sigma) \equiv \int_0^1 ||\tilde{\boldsymbol{x}}(t+\sigma) - \boldsymbol{x}_{k-1}(t)||_2^2 dt, \tag{3.12}$$

where $\boldsymbol{x}_{k-1}$ is a known periodic orbit. Setting the derivative of Eq. (3.12) equal to zero and integrating by parts yields an integral condition which closes the system.

$$\int_0^1 \boldsymbol{x}(t)\boldsymbol{x}'_{k-1}(t)dt = 0 \tag{3.13}$$

To allow continuation past folds, the above system of equations (3.11) and (3.13) is reformulated in terms of the pseudoarclength continuation technique. Finally, the periodic solution is discretized in time allowing the computation to be transformed to a continuation of steady states, as illustrated in Fig. 3.3 for the current system of interest. The details of this procedure and its implementation in AUTO are described well in Doedel et al. [25] and will be omitted here.

Bifurcations of a periodic orbit can also occur. In the case of periodic orbits, the type of bifurcation is determined by the number of Floquet multipliers with modulus equal to one.* One Floquet multiplier is always located at $z = 1$ due to periodicity. A second Floquet multiplier at $z = 1$ signifies a pitchfork bifurcation, which creates or destroys two additional branches of periodic solutions. A *period-doubling* bifurcation occurs when one Floquet multiplier is located at $z = -1$. Finally, a *torus bifurcation* occurs when a complex pair of Floquet multipliers has magnitude of one [26, page 48].

*A brief overview of Floquet theory is given in Appendix A; see Iooss and Joseph [36, Sec. VII.6] or Guckenheimer and Holmes [33, Sec. 1.5] for more details.

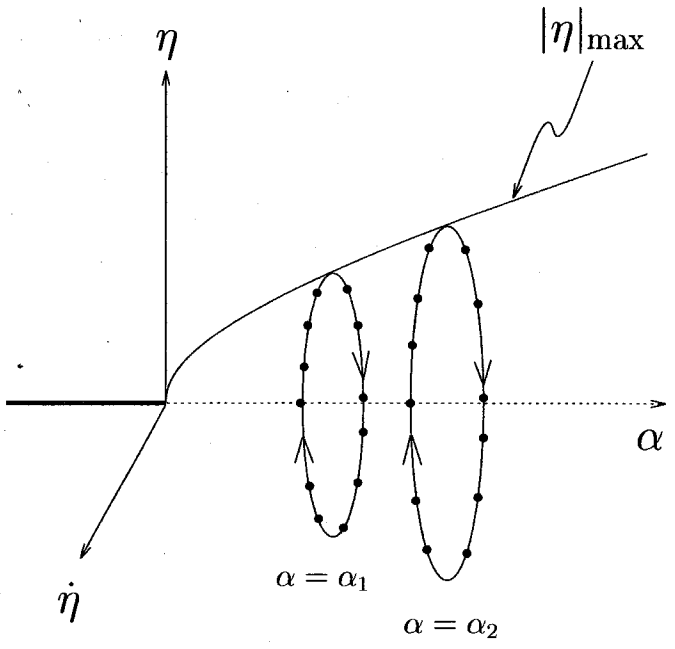

Figure 3.3 Illustration of discretization for the periodic solution continuation method

The stability of periodic solutions is also determined by the Floquet multipliers. If any Floquet multipliers have modulus greater than 1, i.e., $|z| > 1$, the periodic solution is unstable. Only if all Floquet multipliers (other than the one at $z = 1$) have modulus less than 1 is the limit cycle stable.

3.4 Continuation of Folds

It is often interesting to know how the location of a fold varies with a second parameter. For instance, when studying the possibility of triggering, we may wish to know how the region of possible triggering varies with another parameter, say the strength of coupling to combustion processes. AUTO allows the locus of folds to be continued as a function of two parameters. This is accomplished by performing a pseudoarclength continuation of the following

system:

$$\begin{aligned} F(\boldsymbol{x}(s),\mu(s),\lambda(s)) &= 0, \\ F_{\boldsymbol{x}}(\boldsymbol{x}(s),\mu(s),\lambda(s))\phi(s) &= 0, \\ \phi(s)^T\phi_0 - 1 &= 0, \\ (\boldsymbol{x}-\boldsymbol{x}_0)^T\boldsymbol{x}_0' + (\phi-\phi_0)^T\phi_0' + (\mu-\mu_0)\phi_0' + (\lambda-\lambda_0)\lambda_0' - \Delta s &= 0, \end{aligned} \tag{3.14}$$

where λ is a second parameter and ϕ is an eigenvector found by solving the equation $F_{\boldsymbol{x}}(\boldsymbol{x}(s),\lambda(s))\phi(s) = \kappa(s)\phi(s)$.

The above procedure is for the continuation of folds in branches of steady states. The method can be extended to accommodate folds of periodic solution branches as well. AUTO allows continuation of folds in branches of both steady states and periodic solutions.

3.5 Application to the Nonlinear Acoustic Equations

To apply dynamical systems theory to the nonlinear acoustic equations, it is necessary to transform the system from second-order to first-order. This is accomplished by defining a new variable ζ_n such that

$$\zeta_n = \dot{\eta}_n. \tag{3.15}$$

When this new variable is substituted into the second-order system of equations (2.52), we obtain the first-order system of $2n$ equations,

$$\dot{\eta}_n = \zeta_n, \tag{3.16}$$

$$\dot{\zeta}_n = 2\alpha_n\dot{\eta}_n + (2\omega_n\theta_n - \omega_n^2)\eta_n + (F_n)^{\mathrm{NL}}. \tag{3.17}$$

If we let

$$\boldsymbol{x} = \begin{pmatrix} \eta_n \\ \zeta_n \end{pmatrix} \tag{3.18}$$

in Eq. (3.1), then all of the methods of dynamical systems can be readily applied. In most cases, the continuation parameter is chosen to be the linear growth rate of the fundamental mode so that $\mu = \alpha_1$. In the study of the second longitudinal mode instability covered in the next chapter, however, it is more appropriate to chose the linear growth rate of the second mode.

When using the time-averaged equations, the main branches consist of steady states instead of periodic solutions. The time-averaged equations as developed in Chapter 2 are

$$\dot{r}_n = \alpha_n r_n + \frac{1}{\tau_1}\int_t^{t+\tau_1} (F_n)^{\mathrm{NL}} \cos(\omega_n t' + \phi_n) dt', \tag{3.19}$$

$$r_n \dot{\phi}_n = -\theta_n r_n - \frac{1}{\tau_1}\int_t^{t+\tau_1} (F_n)^{\mathrm{NL}} \sin(\omega_n t' + \phi_n) dt'. \tag{3.20}$$

If the equations are modified somewhat, a steady state continuation method may be used. In a limit cycle, $\dot{\phi}_n$ is constant, but not necessarily equal to zero. However, if we define a new variable for the phase shift as

$$\Phi_n(t) = n\phi_1 - \phi_n, \tag{3.21}$$

we find that $\dot{\Phi}_n$ is equal to zero in a limit cycle. Therefore, for the time-averaged equations, we define

$$\boldsymbol{x} = \begin{pmatrix} r_n \\ \Phi_n \end{pmatrix}, \tag{3.22}$$

and a steady state continuation method can then be used instead of a more expensive continuation method for periodic solutions. In addition, the dimension of the system is reduced to $2n - 1$ since $\Phi_1 \equiv 0$.

Chapter 4

Nonlinear Gasdynamics: The Consequences of Truncation and Time-Averaging

Many previous investigations have used the approximate analysis developed in Chapter 2 to study the influence of nonlinear gasdynamics in a cylindrical combustion chamber. Most of those investigations have also used the approximations of time-averaging and truncation to a small number of modes in order to simplify the system of equations. The effects of truncation were examined by Jahnke and Culick [39], but the effects of time-averaging have not been properly studied, especially when more than two modes are included. The cost of calculating solutions for the time-averaged equations is much lower than for the original equations, particularly when the methods of dynamical systems theory are used; a steady state continuation method is much more efficient than a continuation of periodic solutions. Therefore, it is desirable to use the time-averaged equations as long as they produce correct results. In this chapter, we will determine the effects of the method of time-averaging on the case of longitudinal modes in a cylindrical chamber. We will also use dynamical systems theory to study transverse modes in a cylindrical chamber, a case not previously treated using these methods.

4.1 Longitudinal Modes

Oscillations in solid propellant rocket motors often involve mainly fluctuations in the axial direction. If we restrict the analysis to longitudinal modes in a uniform chamber, the mode shapes are given by

$$\psi_n = \cos k_n x, \tag{4.1}$$

where the wave number of the n_{th} mode is $k_n = \frac{n\pi}{L}$. Thus, the frequencies for longitudinal modes are integral multiples of the fundamental frequency, i.e., $\omega_n = n\omega_1$. This simplifies the equations by transforming the double sum in Eq. (2.53) to two single sums. The resulting equations are [51]

$$\begin{aligned}\ddot{\eta}_n + \omega_n^2\eta_n = 2\alpha_n\dot{\eta}_n + 2\omega_n\theta_n\eta_n - \sum_{i=1}^{n-1}[C_{ni}^{(1)}\dot{\eta}_i\dot{\eta}_{n-i} + D_{ni}^{(1)}\eta_i\eta_{n-i}] \\ - \sum_{i=1}^{\infty}[C_{ni}^{(2)}\dot{\eta}_i\dot{\eta}_{n+i} + D_{ni}^{(2)}\eta_i\eta_{n+i}] + (F_n)_{\text{other}}^{\text{NL}},\end{aligned} \tag{4.2}$$

where the term $(F_n)_{\text{other}}^{\text{NL}}$ contains any nonlinear contribution other than gasdynamics to second-order and the nonlinear gasdynamic coefficients are given by

$$C_{ni}^{(1)} = \frac{-1}{2\bar{\gamma}i(n-i)}[n^2 + i(n-i)(\bar{\gamma}-1)], \tag{4.3a}$$

$$C_{ni}^{(2)} = \frac{1}{\bar{\gamma}i(n+i)}[n^2 - i(n+i)(\bar{\gamma}-1)], \tag{4.3b}$$

$$D_{ni}^{(1)} = \frac{(\bar{\gamma}-1)\omega_1^2}{4\bar{\gamma}}[n^2 - 2i(n-i)], \tag{4.3c}$$

$$D_{ni}^{(2)} = \frac{(\bar{\gamma}-1)\omega_1^2}{2\bar{\gamma}}[n^2 + 2i(n+i)]. \tag{4.3d}$$

The system of equations (4.2) will henceforth be referred to as the *original oscillator equations.*

To determine the effects of time-averaging, results for the original oscillator equations will be compared to results for the corresponding time-averaged equations. Application of the method of time-averaging as outlined in Chapter 2 leads to the following set of equations.

$$\frac{dr_n}{dt} = \alpha_n r_n + \frac{1}{2}\beta\omega_n \sum_{i=1}^{n-1} r_i r_{n-i} \cos(\Phi_n - \Phi_i - \Phi_{n-i}) \tag{4.4a}$$
$$+ \beta\omega_n \sum_{i=1}^{\infty} r_i r_{n+i} \cos(\Phi_{n+i} - \Phi_i - \Phi_n)$$
$$+ \frac{1}{\tau_1}\int_t^{t+\tau_1} (F_n)^{\mathrm{NL}}_{\mathrm{other}} \cos(\omega_n t' + \phi_n) dt',$$

$$r_n \frac{d\phi_n}{dt} = -\theta_n r_n + \frac{1}{2}\beta\omega_n \sum_{i=1}^{n-1} r_i r_{n-i} \sin(\Phi_n - \Phi_i - \Phi_{n-i}) \tag{4.4b}$$
$$+ \beta\omega_n \sum_{i=1}^{\infty} r_i r_{n+i} \sin(\Phi_{n+i} - \Phi_i - \Phi_n)$$
$$- \frac{1}{\tau_1}\int_t^{t+\tau_1} (F_n)^{\mathrm{NL}}_{\mathrm{other}} \sin(\omega_n t' + \phi_n) dt',$$

where $\Phi_n = n\phi_1 - \phi_n$ and $\beta = (1+\bar{\gamma})/8\bar{\gamma}$.

In this chapter, we are interested in nonlinear contributions from gasdynamics only. Therefore, we assume here that $(F_n)^{\mathrm{NL}}_{\mathrm{other}} = 0$ in both the original oscillator and the time-averaged equations. The effects of other nonlinear contributions will be dealt with in subsequent chapters.

4.1.1 First Mode Instability

In many cases of interest, the first mode is linearly unstable, and the remaining modes are linearly stable. This occurs because unsteady energy release often affects primarily the fundamental mode, while dissipation from particle damping, etc., is often larger for higher frequencies. Paparizos and Culick [51]

studied the case of a first mode instability using the two mode, time-averaged equations. Later, Jahnke and Culick [39] used dynamical systems theory to determine the effects of truncation on the system of equations. In this section,

n	1	2	3	4	5	6
α_n ($\sec^{-1}$)	$0 \rightarrow 300$	-324.8	-583.6	-889.4	-1262.7	-1500.0
θ_n (rad/sec)	12.9	46.8	-29.3	-131.0	-280.0	-300.0

Table 4.1 Linear growth rates and frequency shifts for the first mode instability

we will investigate the other approximation, namely time-averaging, when the first mode is unstable. The linear growth rates and frequency shifts in Table 4.1 will be used; the fundamental frequency ω_1 is 5654.87 rad/sec.

In their study of the first mode instability, Paparizos and Culick found a stability boundary for the two mode, time-averaged equations. For values of $\alpha_1 > -\frac{1}{2}\alpha_2$, no stable limit cycles exist. Jahnke and Culick compared these results with those obtained using the original oscillator equations. As shown in Fig. 4.1, the two mode, original oscillator equations produce a turning point bifurcation at $\alpha_1 = 146.2$ $\sec^{-1}$. Above this value, no stable limit cycles exist. For this particular case, there is good agreement between the two results up to $\alpha_1 \approx 120$ $\sec^{-1}$. Closer to the turning point bifurcation and the stability boundary, the results diverge.

When four modes are included in the analysis, a turning point bifurcation does not appear in results for the original oscillator equations, as shown in Figs. 4.2–4.5 for modes one to four. The time-averaged equations still produce a stability boundary, but it occurs for a higher value of α_1. Now, the time-averaged results are accurate up to $\alpha_1 \approx 200$ $\sec^{-1}$. In the six mode case, the range is increased even more, as shown in Figs. 4.6 for the first mode. Results for more than six modes were also calculated, and this trend continued as

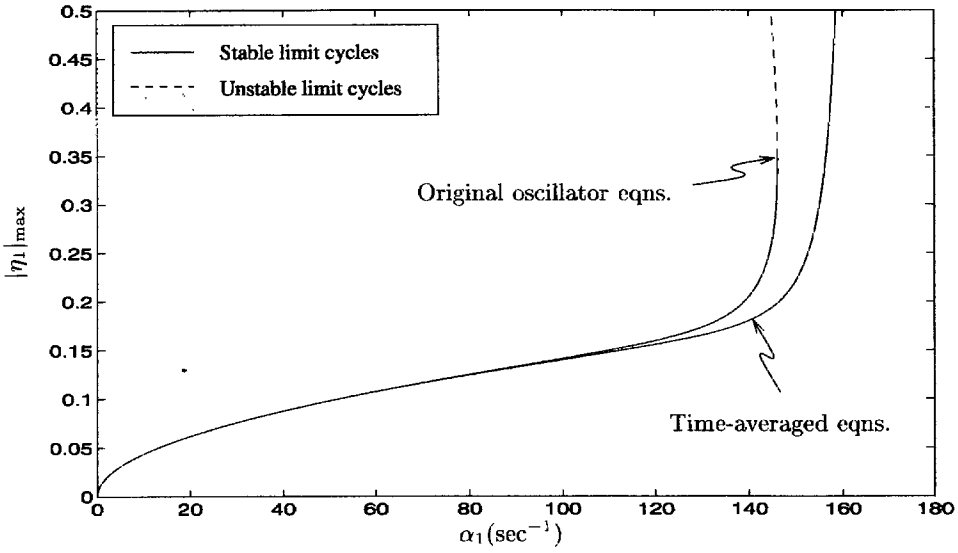

Figure 4.1 Maximum amplitude of η_1 in limit cycle for the time-averaged and original oscillator equations; first longitudinal mode instability, two modes

more modes were included; see Figs. 4.7 and 4.8 for eight and ten modes, respectively.

It is evident that if a sufficient number of modes is used, the time-averaged equations can adequately predict the amplitudes of acoustic modes in a highly unstable system. Although the limit cycle amplitudes do not match exactly for very high values of α_1, the agreement is good until the amplitudes become large. It must not be forgotten that both sets of equations are based on a perturbation method, and results are not valid for 'large' amplitudes, say greater than 0.3 or so.

The previous figures also show another interesting result. One major conclusion of the investigation by Jahnke and Culick concerned the stability boundary produced by the time-averaged equations when truncated to two modes. It was reported that this stability boundary was an artifact of truncation to two modes and not a result of the method of time-averaging. Closer inspection of the current results reveals that this is not true. As more modes

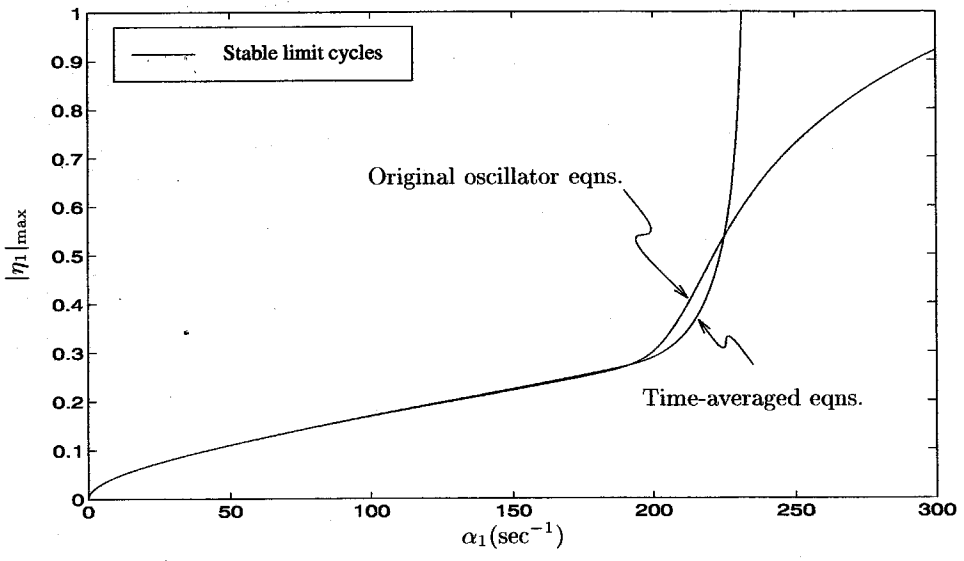

Figure 4.2 Maximum amplitude of η_1 in limit cycle for the time-averaged and original oscillator equations; first longitudinal mode instability, four modes

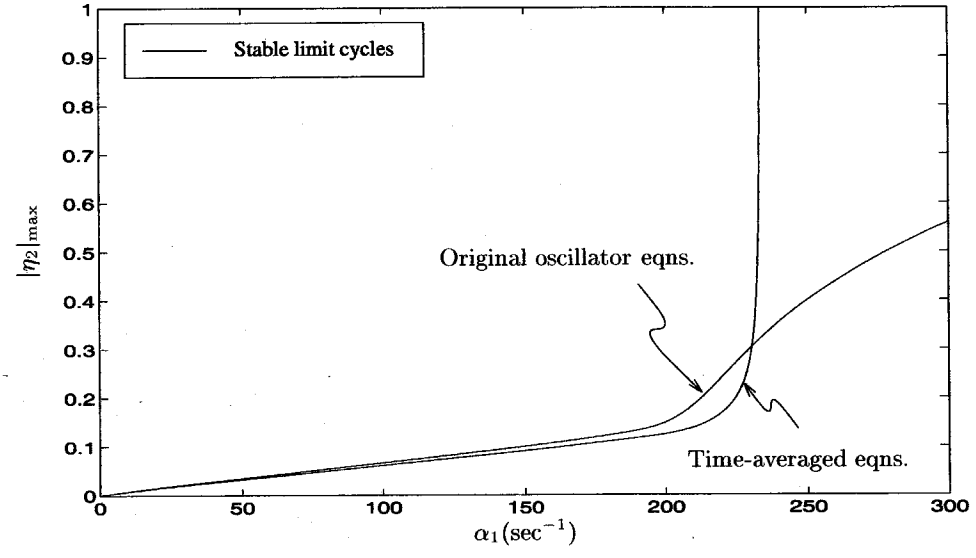

Figure 4.3 Maximum amplitude of η_2 in limit cycle for the time-averaged and original oscillator equations; first longitudinal mode instability, four modes

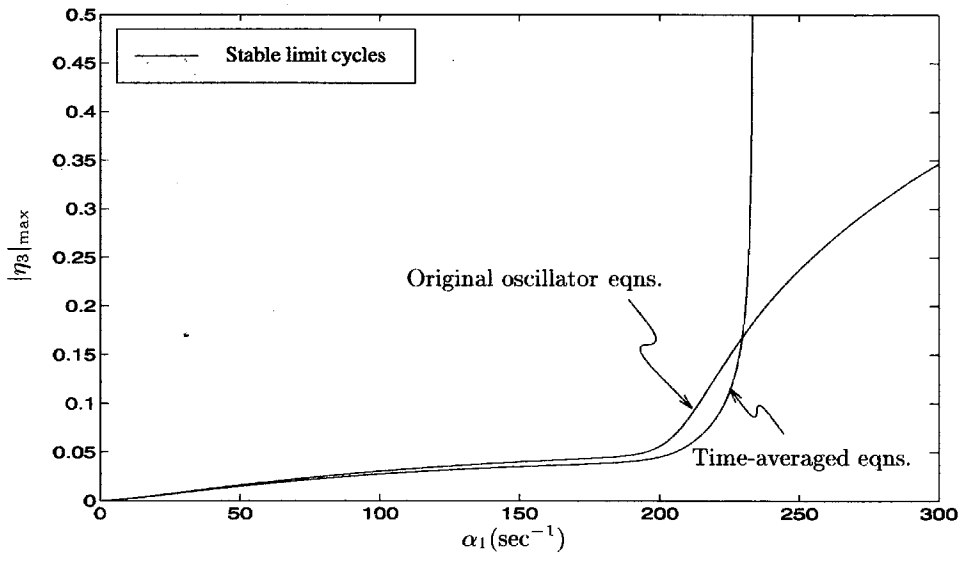

Figure 4.4 Maximum amplitude of η_3 in limit cycle for the time-averaged and original oscillator equations; first longitudinal mode instability, four modes

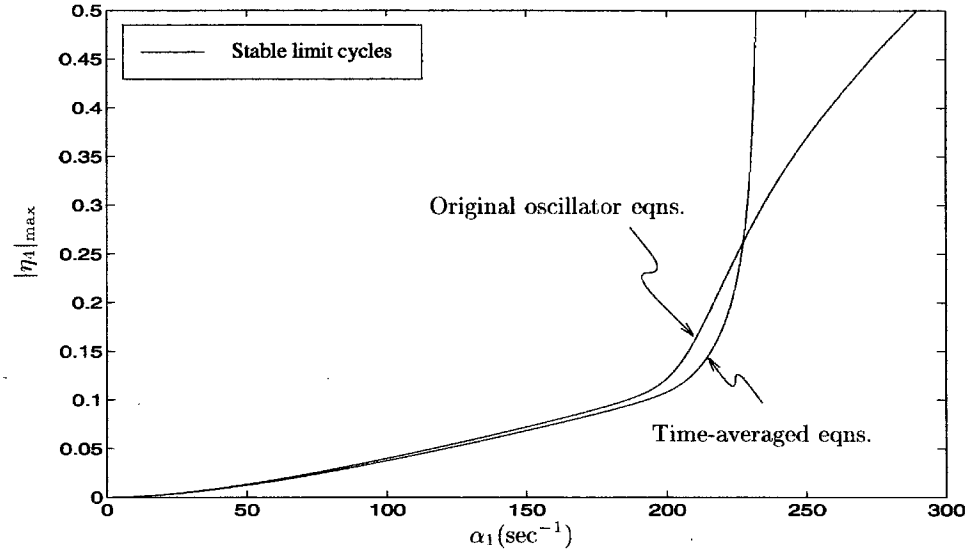

Figure 4.5 Maximum amplitude of η_4 in limit cycle for the time-averaged and original oscillator equations; first longitudinal mode instability, four modes

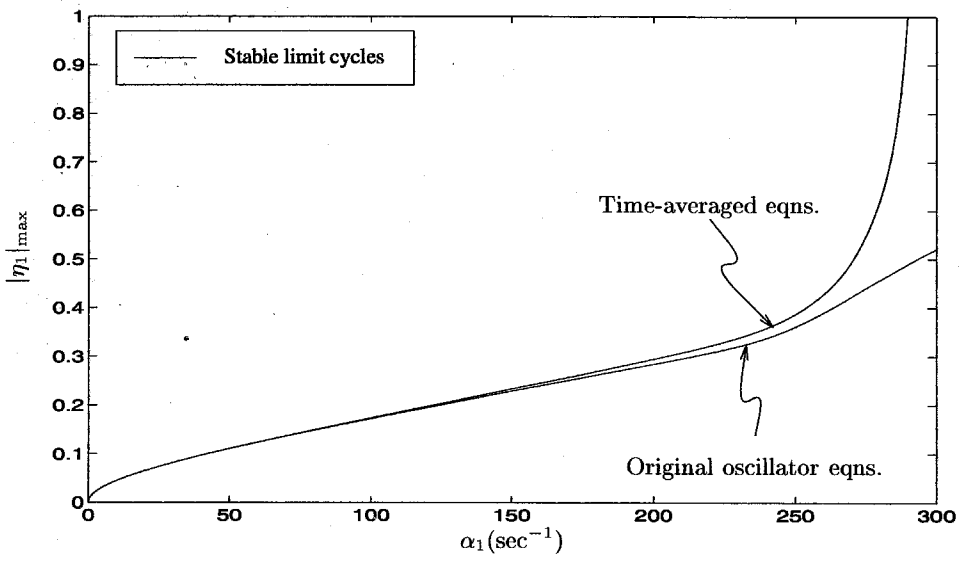

Figure 4.6 Maximum amplitude of η_1 in limit cycle for the time-averaged and original oscillator equations; first longitudinal mode instability, six modes

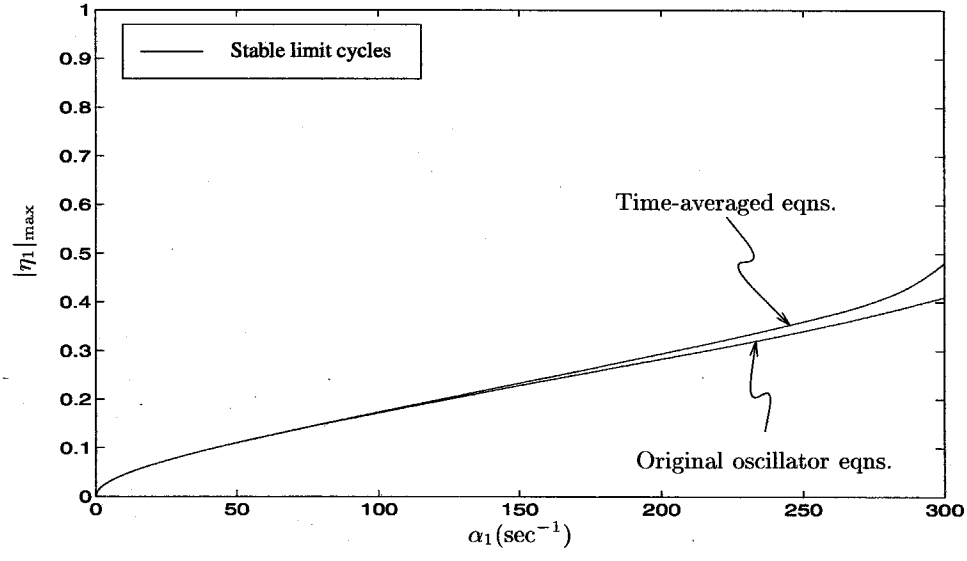

Figure 4.7 Maximum amplitude of η_1 in limit cycle for the time-averaged and original oscillator equations; first longitudinal mode instability, eight modes

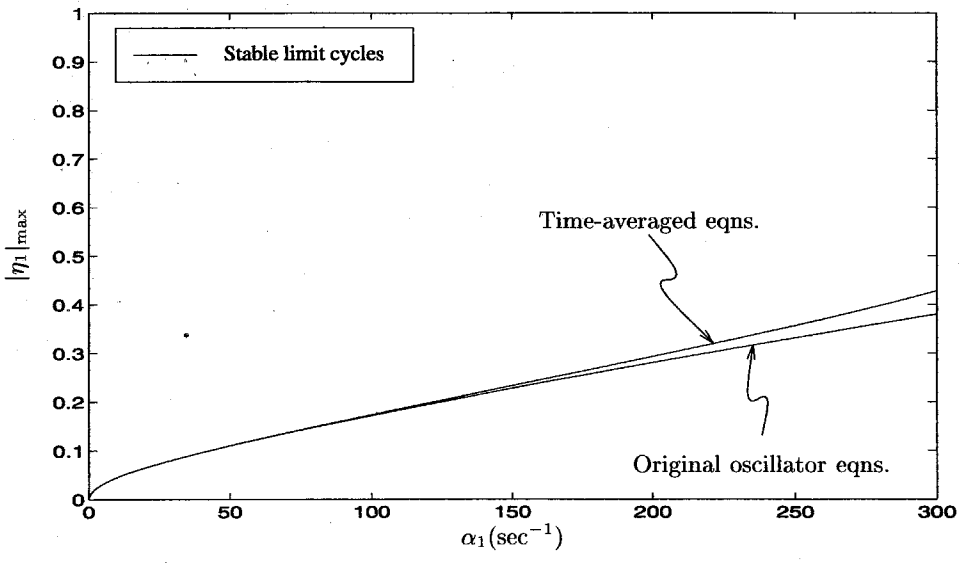

Figure 4.8 Maximum amplitude of η_1 in limit cycle for the time-averaged and original oscillator equations; first longitudinal mode instability, ten modes

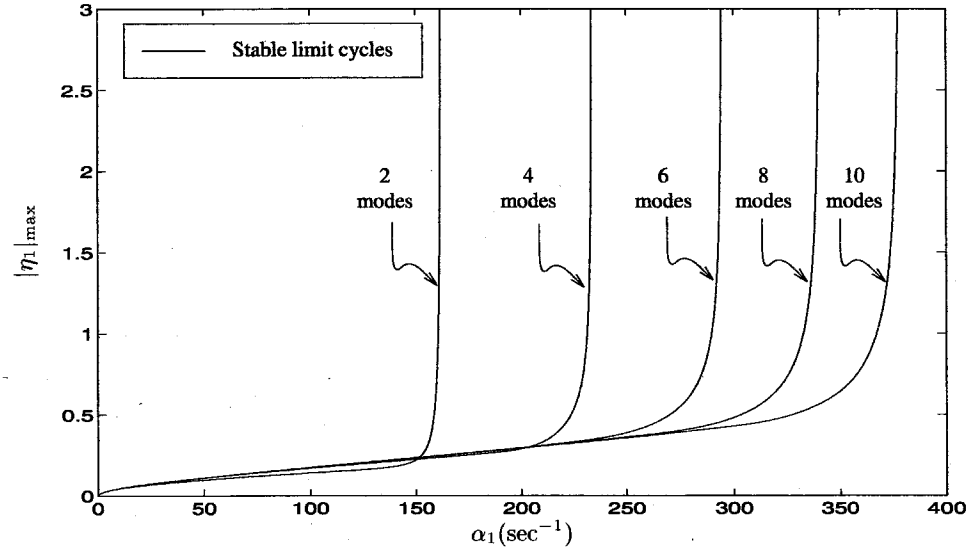

Figure 4.9 Stability boundaries produced by the time-averaged equations for truncation from two to ten modes; first longitudinal mode instability

are included with the time-averaged equations, the stability boundary shifts to a larger value of α_1, but the boundary is still present as illustrated in Fig. 4.9. The turning point produced by the original oscillator equations is, in fact, a consequence of truncation to two modes since no turning point is found when using a higher number of modes. However, the time-averaged equations appear to produce a stability boundary, no matter how many modes are included in the analysis.

4.1.2 Second Mode Instability

The previous section has shown that the time-averaged equations can yield satisfactory results for the case of a first mode instability. This case is fairly simple; no additional bifurcation points have been found. The case of a second mode instability, however, can be more complicated, as shown by Jahnke and Culick [39, 38]. For small values of α_2, the odd-numbered modes are unexcited while only the even-numbered modes have non-zero amplitudes. As the system becomes more unstable, these modes can become excited via a period-doubling bifurcation if an insufficient number of modes is included. Additional bifurcations, such as torus bifurcations, have also been found when the second mode is unstable. The values in Table 4.2 were used by Jahnke and Culick and will be used here as well to determine the effects of time-averaging when the second mode is unstable.

n	1	2	3	4	5	6
α_n ($\sec^{-1}$)	-84.9	$0 \rightarrow 200$	-161.0	-279.4	-329.7	-520.2
θ_n (rad/sec)	-66.7	12.9	108.2	46.8	8.8	-29.3

Table 4.2 Linear growth rates and frequency shifts for the second mode instability

In their study of a second mode instability, Jahnke and Culick [37] obtained results for truncation to four modes using both the time-averaged and original oscillator equations. However, results for the time-averaged equations were qualitatively incorrect. Only one branch of limit cycles was reported, while at least two other branches are present. Two additional bifurcations, one period-doubling bifurcation and one Hopf bifurcation, are also found as shown in Figs. 4.10–4.13.

Bifurcation diagrams for the time-averaged equations are difficult to obtain when the second mode is unstable, so it is possible that other branches may also be present. Due to the combination of unexcited modes along with a singularity for $r_n = 0$, it is not possible to construct the bifurcation diagrams in the normal fashion. The modified computational process is as follows. First, compute a steady state ($\dot{r}_n, \dot{\Phi}_n = 0$ for all n) for a small value of α_2 using only the second and fourth modes in the simulation. This state is then used with the continuation method to generate the primary branch, i.e., the one reported by Jahnke and Culick. Next, a search for other steady states and/or periodic solutions is performed for different values of α_2 using all four modes. When a stationary solution is found, the continuation method allows this branch to be calculated as well.

Creating a bifurcation diagram in this manner is less than ideal since bifurcations of the full system cannot be located while using only the even-numbered modes. It is therefore difficult to determine if all branches have been discovered. It should be noted, however, that it is always difficult to know whether or not all possible states of the system have been located due to the possibility of isolated solutions [36].

In any case, application of time-averaging along with truncation to four modes produces a very interesting result for the second mode instability. This is the first case reported in which two stable periodic solutions have been

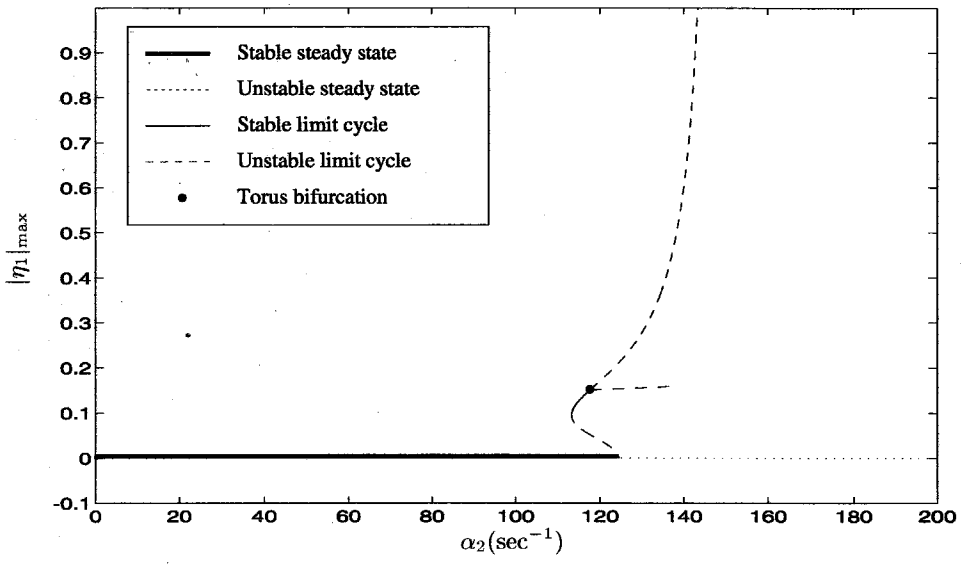

Figure 4.10 Maximum amplitude of η_1 in limit cycle for the time-averaged equations; second longitudinal mode instability, four modes

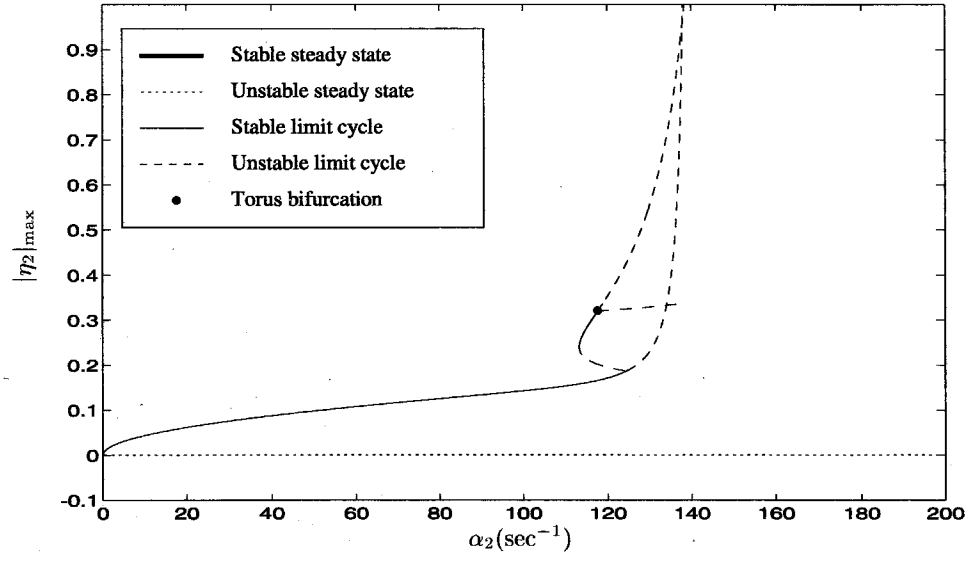

Figure 4.11 Maximum amplitude of η_2 in limit cycle for the time-averaged equations; second longitudinal mode instability, four modes

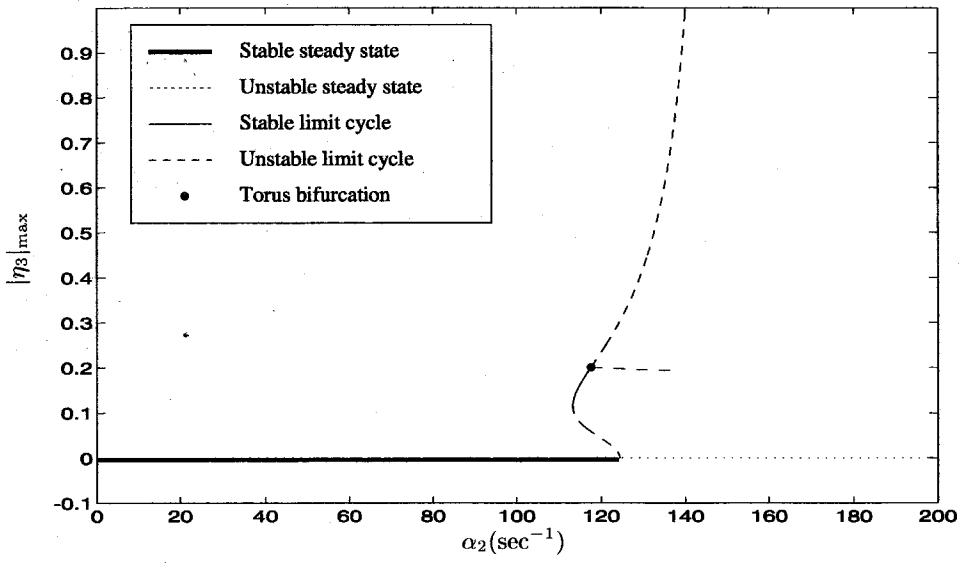

Figure 4.12 Maximum amplitude of η_3 in limit cycle for the time-averaged equations; second longitudinal mode instability, four modes

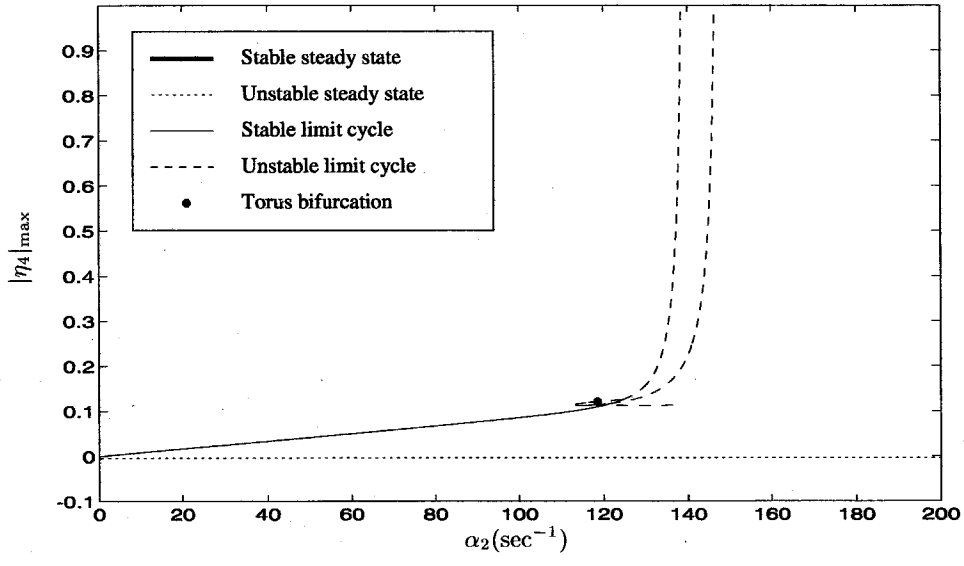

Figure 4.13 Maximum amplitude of η_4 in limit cycle for the time-averaged equations; second longitudinal mode instability, four modes

found for the same values of the linear parameters. As seen in Figs. 4.10–4.13, there is a small range of α_2 which contains two branches of stable limit cycles. Which stable limit cycle is reached depends upon the initial conditions, as demonstrated in Figs. 4.14 and 4.15. When more modes are included in the analysis, this behavior, i.e., that shown in Figs. 4.10–4.13, no longer occurs. It is clearly a direct result of truncation to a small number of modes and is therefore of little consequence in the overall picture. It does, however, illustrate the complexity of the system of equations, even when truncated to only a few modes.

Results obtained by Jahnke and Culick [37] for the four mode case showed that the agreement between the original oscillator and time-averaged equations is good for mildly unstable systems. We will now look at the six mode approximation to determine if the inclusion of more modes extends this to a more linearly unstable system. We would also like to establish whether the time-averaged equations can accurately predict the complex behavior produced by the original oscillator equations.

The bifurcation diagrams for the six mode case were produced using the procedure outlined above. As shown in Figs. 4.16–4.21, the results for the two sets of equations are qualitatively similar, although the locations of the additional bifurcations are not exact. As in the first mode instability, a stability boundary exists which appears to influence the accuracy of results. As more modes are included, the boundary shifts to a higher value of α_2, and the time-averaged results are then accurate over a larger range of α_2 as well.

It was previously shown by Jahnke and Culick [39] that the period-doubling bifurcation produced by the original oscillator equations is a result of truncation. This is also the case for the time-averaged equations. Figure 4.22 shows a comparison of results for the 16 mode, time-averaged equations and the results obtained by Jahnke and Culick for the original oscillator equations (only

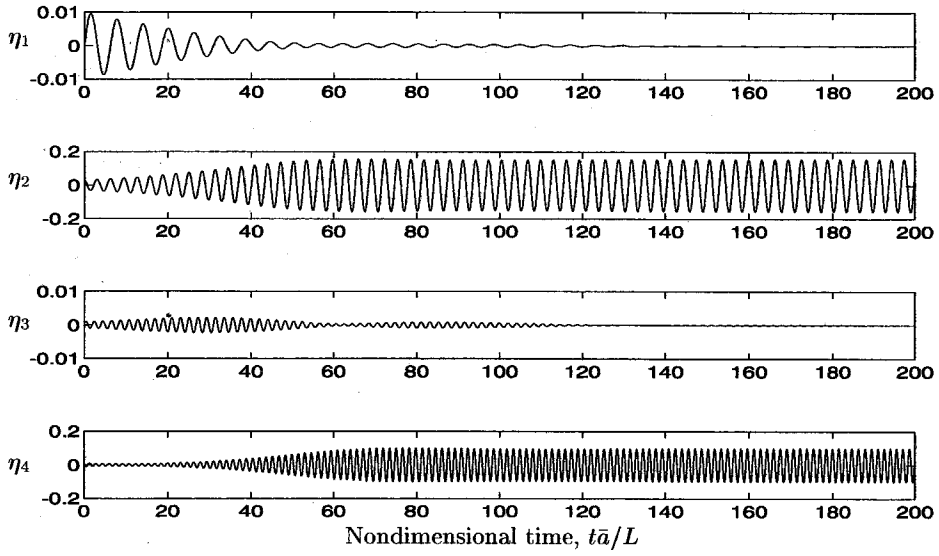

Figure 4.14 Time history of the second longitudinal mode instability; $\alpha_2 = 114$ sec^{-1}, low initial conditions

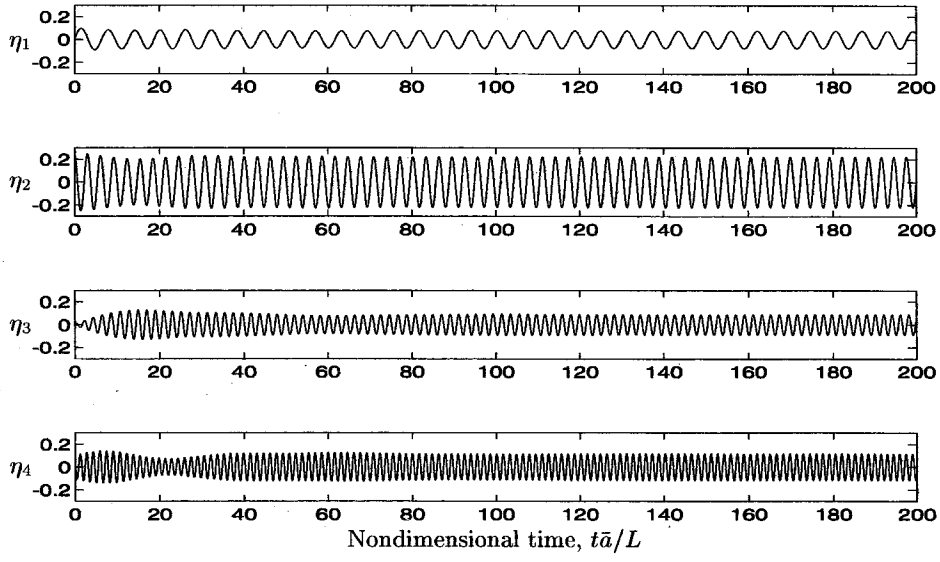

Figure 4.15 Time history of the second longitudinal mode instability; $\alpha_2 = 114$ sec^{-1}, high initial conditions

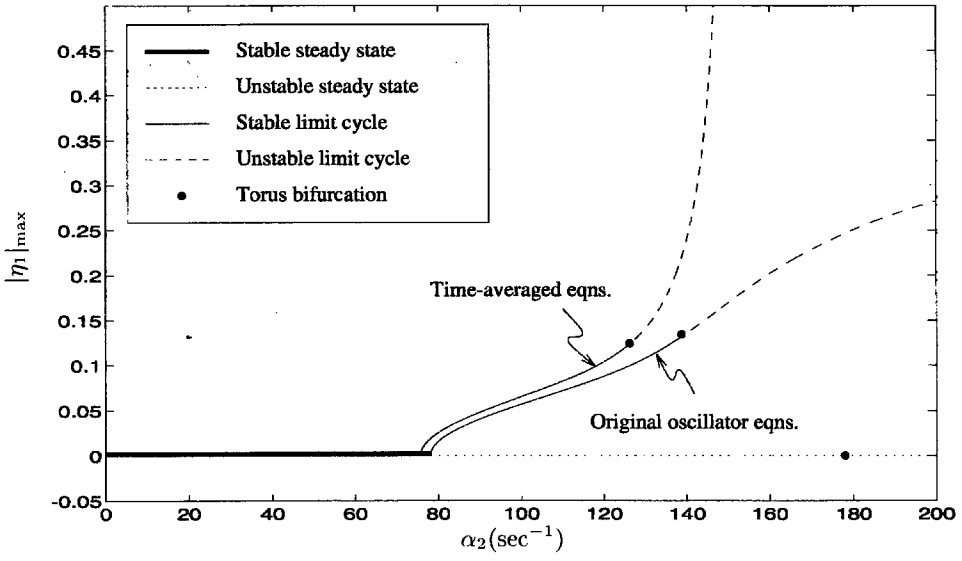

Figure 4.16 Maximum amplitude of η_1 in limit cycle for the time-averaged and original oscillator equations; second longitudinal mode instability, six modes

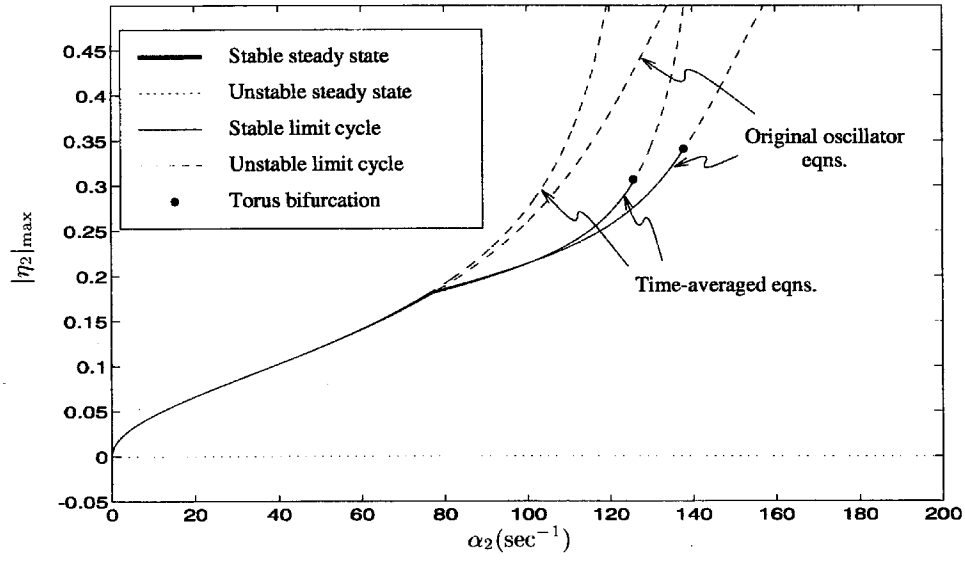

Figure 4.17 Maximum amplitude of η_2 in limit cycle for the time-averaged and original oscillator equations; second longitudinal mode instability, six modes

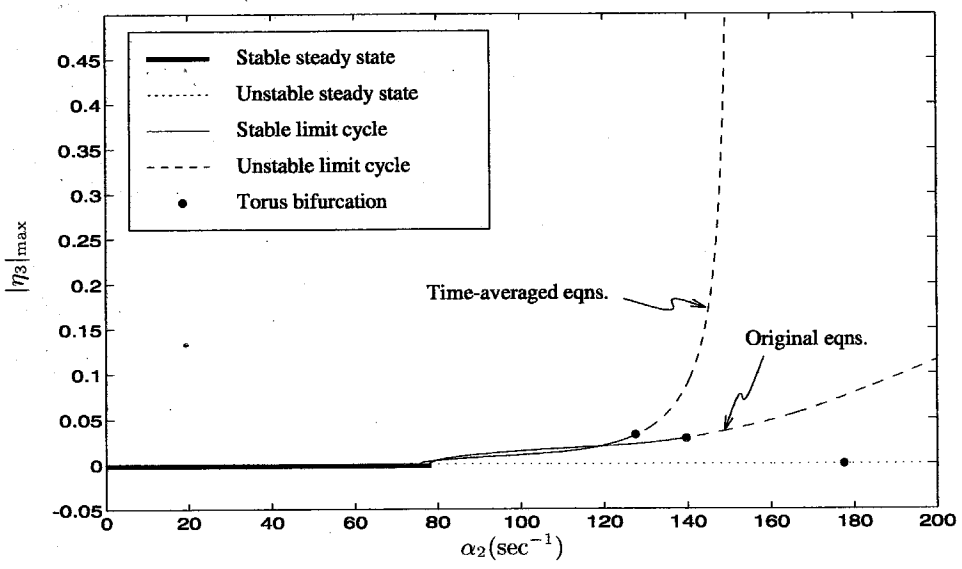

Figure 4.18 Maximum amplitude of η_3 in limit cycle for the time-averaged and original oscillator equations; second longitudinal mode instability, six modes

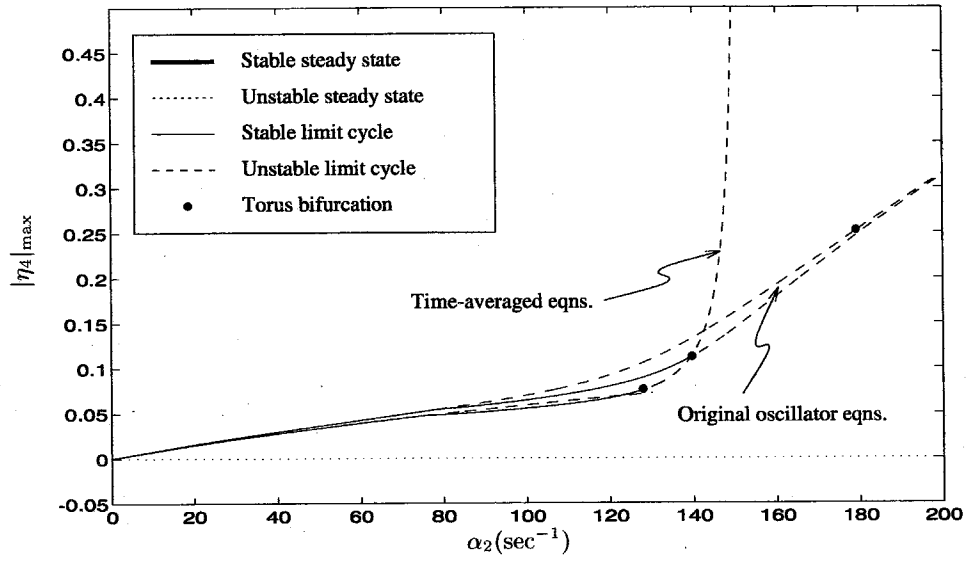

Figure 4.19 Maximum amplitude of η_4 in limit cycle for the time-averaged and original oscillator equations; second longitudinal mode instability, six modes

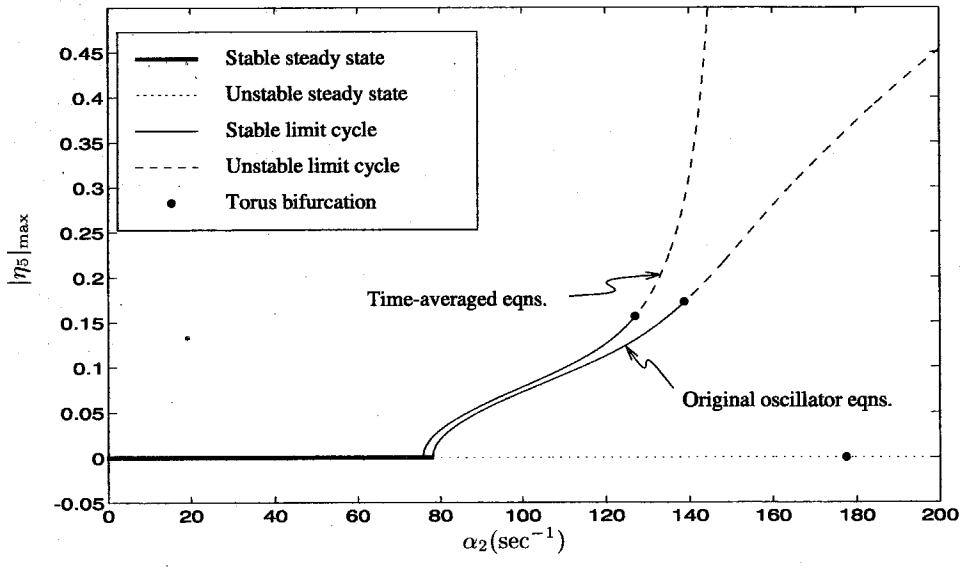

Figure 4.20 Maximum amplitude of η_5 in limit cycle for the time-averaged and original oscillator equations; second longitudinal mode instability, six modes

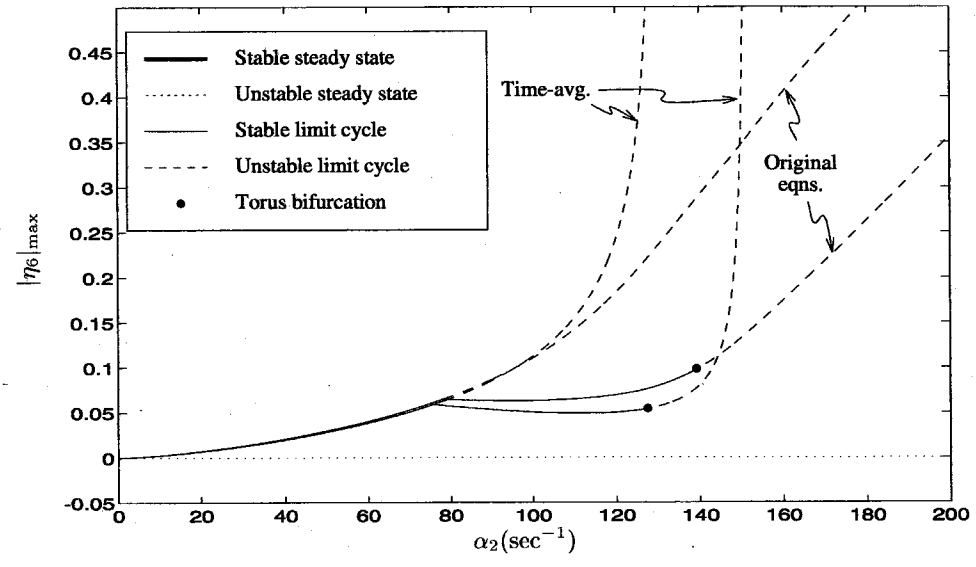

Figure 4.21 Maximum amplitude of η_6 in limit cycle for the time-averaged and original oscillator equations; second longitudinal mode instability, six modes

the second mode is included for brevity). For this range of α_2, no additional bifurcations are found, and the odd-numbered modes remain unexcited. In addition, the amplitudes are in close agreement over the entire range.

The previous sections have shown that the time-averaged equations can produce good results in the cases of a first or second longitudinal mode instability. This is a very useful result since the time-averaged equations can be used at a substantial savings compared with the original oscillator equations. However, the following points should be kept in mind whenever using these equations. 1) The approximate analysis is based on a perturbation method which assumes that $p'/\bar{p}$ is a small quantity. Therefore, results with large amplitudes are not valid. 2) The accuracy of results depends on the number of modes included in the analysis: the more highly unstable the system, the higher the number of modes needed to obtain good accuracy. In particular, agreement between the two sets of equations is good only sufficiently far from the stability boundary produced by time-averaging.

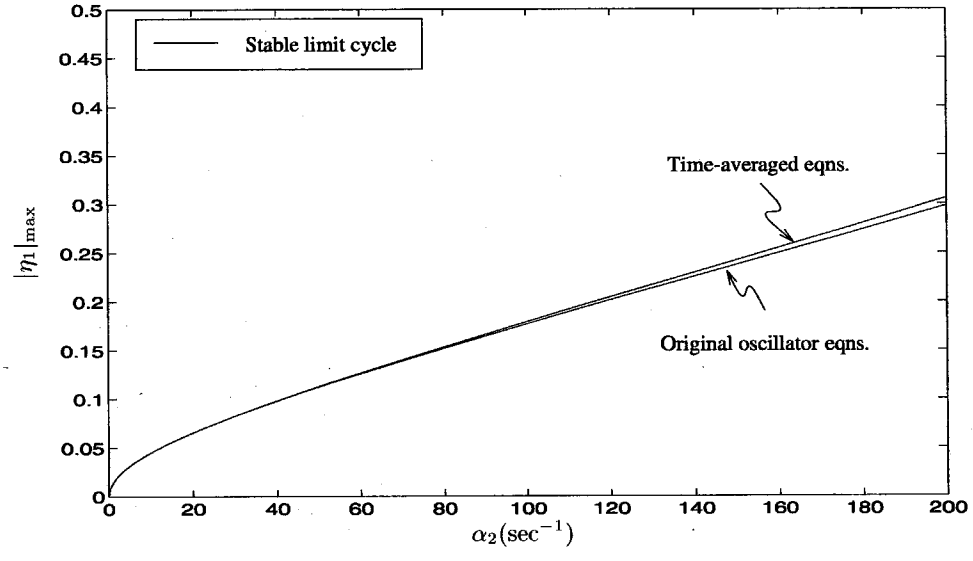

Figure 4.22 Maximum amplitude of η_2 in limit cycle for the time-averaged and original oscillator equations; second longitudinal mode instability, 16 modes

4.2 Transverse Modes

Several previous works have studied transverse oscillations in a uniform cylindrical chamber using the approximate analysis [55, 57, 42]. Those investigations have used the additional approximations of time-averaging and truncation to a small number of modes in order to obtain analytical solutions. In this section, we will apply the methods of dynamical systems theory to cases involving transverse modes. We will also study the role of nonlinear gasdynamics in the formation of limit cycles using the analytical results obtained by Yang and Culick [55].

When dealing with transverse oscillations, an extra degree of freedom allows the possibility of both standing and spinning modes. In this study, we will treat only the case of standing transverse modes by restricting the mode shapes to only one of the two azimuthal eigenvalues. The mode shapes are then defined by

$$\psi_n(\boldsymbol{r}) = J_m(\kappa_{ms} r)\cos m\theta. \tag{4.5}$$

The wave number of the n_{th} mode k_n is now equal to κ_{ms} and is determined by solving Eq. (2.57). Table 4.3 is a list of the wave numbers for the modes which will be used in this section. Note that, unlike longitudinal modes, the wave numbers and thus the natural frequencies are not integral multiples of the fundamental mode. Also, the nonlinear gasdynamic coefficients A_{nij} and B_{nij} for transverse modes involve integration of Bessel functions. Closed form solutions are difficult to obtain, and the values will thus be calculated by numerical integration.

Yang and Culick [55] studied the conditions for existence and stability of limit cycles for transverse modes using the time-averaged equations truncated to a small number of modes. The amplitudes of oscillations were found to

s \ m	0	1	2	3	4	5	6
1	3.8317	1.8412	3.0542	4.2012	5.3176	6.4156	7.5013
2	7.0156	5.3314	6.7061	8.0152	9.2824	10.5199	11.7349
3	10.1735	8.5363	9.9695	11.3459	12.6819	13.9872	15.2682

Table 4.3 Nondimensional wave numbers for transverse modes, $(\kappa_{ms}R)$

be quite large, even for reasonable values of the linear growth rates. We will investigate two of the cases treated by Yang and Culick to determine the reason that such high amplitudes were attained.

4.2.1 Tangential Oscillations

Of the cases studied by Yang and Culick [55], the case involving only the first and second tangential modes produced the largest amplitudes. In fact, all results for this case were outside the range of validity of the approximate analysis. An example of a numerical simulation of the time-averaged equations is shown in Fig. 4.23.

Truncation to a small number of modes can have a substantial effect on the amplitudes of oscillations in some cases. It was suggested by Yang and Culick that this may be partly responsible for the large amplitudes. To determine the effects of truncation on tangential oscillations, results for the original oscillator equations with truncation to two, four, and six modes are compared. As shown in Fig. 4.24, inclusion of more modes had an effect on the amplitudes as α_{1T} increases. However, the results are valid only for very small values of α_{1T} due to the large amplitudes that are reached. Below $\alpha_{1T} \approx 0.0002$ sec^{-1}, there is virtually no difference between results obtained using two, four, and six modes. It was also determined that including tangential modes with higher values of s

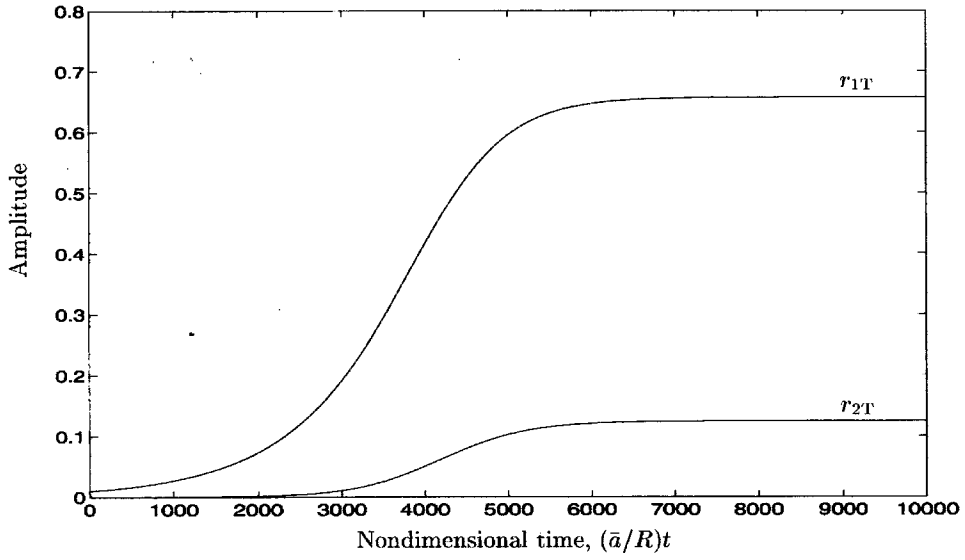

Figure 4.23 Simulation of the time-averaged equations, first and second tangential modes; $(R/\bar{a})\alpha_{1T} = 0.001$, $(R/\bar{a})\alpha_{2T} = -0.1$, $\theta_{1T} = \theta_{2T} = 0$

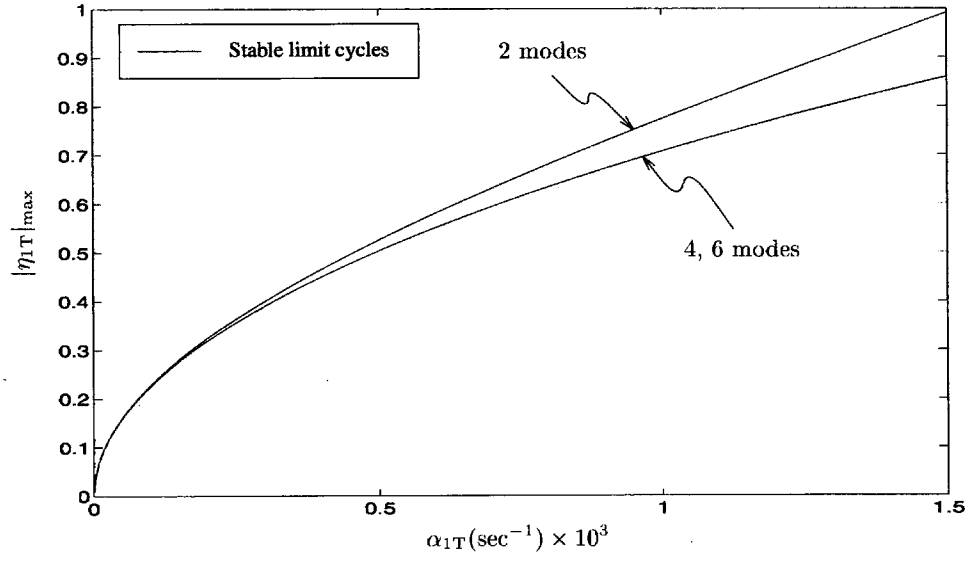

Figure 4.24 Maximum amplitude in limit cycle of the first tangential mode; original oscillator equations with two, four, and six tangential modes, $\theta_n = 0$ for all n

has little effect on the amplitudes. It is thus evident that the high amplitudes found by Yang and Culick are not the result of truncation to a small number of modes.

The energy balance among acoustic modes is very important in the formation of limit cycles [51]. The simplest case of a limit cycle consists of one mode which provides energy, one mode which dissipates energy, and a mechanism which transfers energy between the two. In order to better understand the case of tangential oscillations, we will investigate the balance of energy between the first and second tangential modes using the time-averaged equations. The first tangential mode will be unstable, while the second will be stable.

In terms of the amplitude r_n, the nondimensional energy in an acoustic mode is defined as [46]

$$\varepsilon_n(t) = \left(\frac{E_n^2}{R^2 L}\right) r_n^2(t), \tag{4.6}$$

where E_n^2 is the inner product defined in Chapter 2. This definition of energy is different than the definition used in the investigation by Yang and Culick. The previous definition referred to the energy in the oscillator, not the energy in the acoustic mode. Differentiation of Eq. (4.6) with respect to time yields the rate of change of energy in the acoustic mode.

$$\frac{d\varepsilon_n}{dt} = 2\left(\frac{E_n^2}{R^2 L}\right) r_n \frac{dr_n}{dt} \tag{4.7}$$

Thus, in order to study the energy balance in detail, we need an expression for dr_n/dt.

As derived in Yang and Culick [55], the time-averaged equations for the amplitudes and phase difference of the first and second tangential modes are

$$\frac{dr_{1T}}{dt} = \alpha_{1T} r_{1T} + a_T r_{1T} r_{2T} \cos X_T, \tag{4.8}$$

$$\frac{dr_{2T}}{dt} = \alpha_{2T} r_{2T} + b_T r_{1T}^2 \cos X_T, \tag{4.9}$$

$$\frac{dX_T}{dt} = -2\theta_{1T} + \theta_{2T} + \Omega_{2T} - \left(2a_T r_{2T} + b_T \frac{r_{1T}^2}{r_{2T}}\right) \sin X_T, \tag{4.10}$$

where

$$X_T(t) = 2\phi_{1T} - \phi_{2T} + \Omega_{2T} t,$$

$$\Omega_{2T} = 2\omega_{1T} - \omega_{2T},$$

$$a_T = -0.0521 \left(\frac{\bar{a}}{R}\right),$$

$$b_T = 0.1873 \left(\frac{\bar{a}}{R}\right).$$

Substitution of Eqs. (4.8) and (4.9) in (4.7) gives the rate of change of energy in the first two tangential modes.

$$\frac{d\varepsilon_{1T}}{dt} = 2\alpha_{1T}\varepsilon_{1T} + 2a_T \varepsilon_{1T} r_{2T} \cos X_T \tag{4.11}$$

$$\frac{d\varepsilon_{2T}}{dt} = 2\alpha_{2T}\varepsilon_{2T} + 2b_T \varepsilon_{2T} \left(\frac{r_{1T}^2}{r_{2T}}\right) \cos X_T \tag{4.12}$$

In the above equations, the first term in each equation represents the rate of energy production/dissipation in the acoustic mode, while the second term represents the rate of energy transfer into/out of the mode.

Based on the results for longitudinal modes by Paparizos and Culick [51], we expect that the sum of linear energy production and linear energy dissipation should equal zero in limit cycle, i.e., $\sum_n 2\alpha_n \varepsilon_n = 0$. Although it has not been proven formally for the case of transverse modes, numerical results show

that for the first and second tangential modes,

$$2\alpha_{1T}\varepsilon_{1T} + 2\alpha_{2T}\varepsilon_{2T} \approx 0. \tag{4.13}$$

Attempts at a formal proof have been unsuccessful so far due to the complex nature of transverse modes. This topic will be the subject of future work.

The rate of energy transfer between modes depends on the phase difference X_T, so it is important to examine this variable more closely and determine its role in the balance of energy. In particular, we are interested in $\cos X_T$ since it is a measure of the efficiency of the energy transfer mechanism. We will first look at the limiting value of $\cos X_T$ in limit cycle, and then examine its transient behavior.

In limit cycle, the amplitudes r_n and the phase difference X_T are constant. Therefore, the time derivatives in Eqs. (4.8)–(4.10) vanish, and the system becomes

$$\alpha_{1T} r_{1T} + a_T r_{1T} r_{2T} \cos X_T = 0, \tag{4.14}$$

$$\alpha_{2T} r_{2T} + b_T r_{1T}^2 \cos X_T = 0, \tag{4.15}$$

$$-2\theta_{1T} + \theta_{2T} + \Omega_{2T} - \left(2a_T r_{2T} + b_T \frac{r_{1T}^2}{r_{2T}}\right) \sin X_T = 0. \tag{4.16}$$

From Eq. (4.16), it is easy to see that

$$\sin X_T = \left(\frac{-2\theta_{1T} + \theta_{2T} + \Omega_{2T}}{2a_T r_{2T} + b_T \frac{r_{1T}^2}{r_{2T}}}\right). \tag{4.17}$$

After substitution for r_{1T} and r_{2T} from Eqs. (4.14) and (4.15) followed by some straightforward algebra, we find that

$$\cos^2 X_T = \frac{(2\alpha_{1T} + \alpha_{2T})^2}{(2\alpha_{1T} + \alpha_{2T})^2 + (2\theta_{1T} - \theta_{2T} - \Omega_{2T})^2}. \tag{4.18}$$

This is an important relation as it reveals much information about the energy transfer between modes. Two results can be obtained immediately from this equation. First, when the numerator $2\alpha_{1T} + \alpha_{2T}$ is equal to zero, then

$$\cos X_T = 0. \tag{4.19}$$

In terms of the energy balance, this relation corresponds to a complete absence of energy transfer between modes, as inspection of Eqs. (4.11) and (4.12) shows. As a result, a stability boundary occurs when $\alpha_{1T} = -\frac{1}{2}\alpha_{2T}$ due to the lack of energy transfer. Closer inspection of the equations for longitudinal modes shows that this, i.e., zero energy transfer between modes, is the cause for the stability boundary in that case as well.

A second result is found when the second term in the denominator of Eq. (4.18) is equal to zero, i.e., $2\theta_{1T} - \theta_{2T} - \Omega_{2T} = 0$. In a more illustrative form, this is equivalent to

$$\omega_{2T} - \theta_{2T} = 2\left(\omega_{1T} - \theta_{1T}\right). \tag{4.20}$$

Hence, if the shifted linear frequency* of the second tangential mode is exactly twice the shifted linear frequency of the first tangential mode, then

$$|\cos X_T| = 1, \tag{4.21}$$

and the energy transfer between modes is most efficient. If the shifted linear frequency of the second tangential mode is not exactly twice that of the first, then the energy transfer is less efficient and the amplitudes must become larger in order to attain a balance between the rate of energy transfer between

*By shifted linear frequency, we mean the unperturbed natural frequency shifted by linear processes, i.e., $\omega - \theta$.

modes and the rates of energy production/dissipation. For instance, in the case studied by Yang and Culick, θ_{1T} and θ_{2T} were arbitrarily set to zero. The limiting value of $|\cos X_T|$ is 0.143 so that the energy transfer mechanism is only 14.3% as efficient as the case in which Eq. (4.20) is satisfied. This inefficient energy transfer is precisely the reason that such high amplitudes were produced. Accurate modeling of all important linear processes is needed in order to obtain good quantitative results.

To illustrate the dramatic effect that linear frequency shifts can have on the amplitudes of the tangential modes, bifurcation diagrams were generated using the original oscillator equations. Figure 4.25 shows diagrams for three different ratios of shifted frequencies, $(\omega_{2T} - \theta_{2T})/(\omega_{1T} - \theta_{1T})$. The arbitrary choice by Yang and Culick of $\theta_{1T} = \theta_{2T} = 0$ corresponds to $(\omega_{2T} - \theta_{2T})/(\omega_{1T} - \theta_{1T}) = 1.66$. For this ratio of shifted frequencies, the amplitudes are quite high, and the results are valid only for very mildly unstable systems. When the ratio is increased to 1.8, the amplitudes are reduced substantially. Finally, the smallest amplitudes are attained when the ratio is exactly equal to two, as indicated above. The results are then valid for a much larger range of α_{1T} in this case.

The effect of the linear frequency shifts can also be seen directly in the analytical results obtained by Yang and Culick. The limiting amplitudes for the first and second tangential modes are

$$r_{1T}^2 = \frac{\alpha_{1T}\alpha_{2T}}{a_T b_T}\left[1 + \left(\frac{2\theta_{1T} - \theta_{2T} - \Omega_{2T}}{2\alpha_{1T} + \alpha_{2T}}\right)^2\right], \tag{4.22}$$

$$r_{2T} = -\frac{\alpha_{1T}}{a_T}\left[1 + \left(\frac{2\theta_{1T} - \theta_{2T} - \Omega_{2T}}{2\alpha_{1T} + \alpha_{2T}}\right)^2\right]^{1/2}. \tag{4.23}$$

By inspection, we see that both r_{1T} and r_{2T} are minimum when Eq. (4.20) is satisfied, i.e., $2\theta_{1T} - \theta_{2T} - \Omega_{2T} = 0$. As $|2\theta_{1T} - \theta_{2T} - \Omega_{2T}|$ increases, the amplitudes for the first and second tangential modes increase as well. The stability

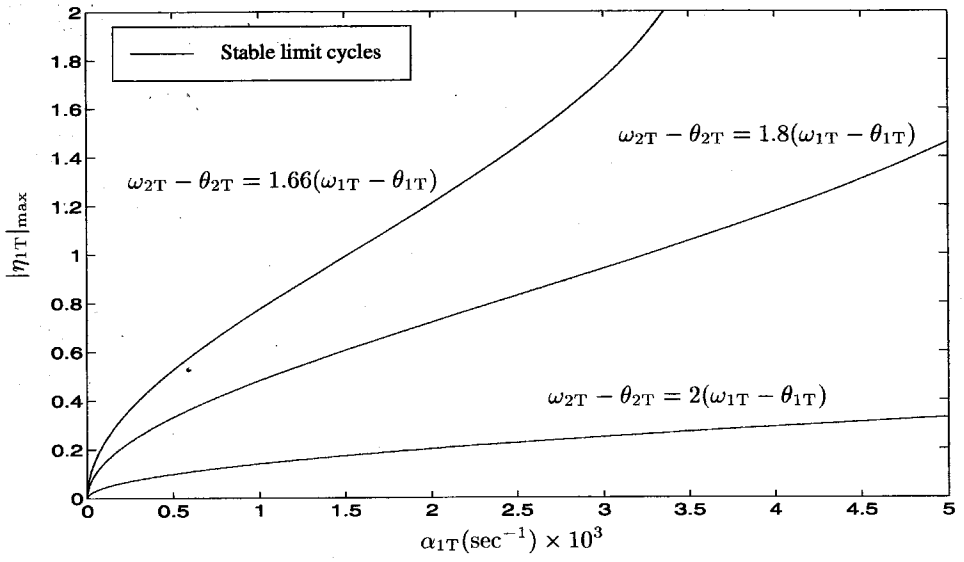

Figure 4.25 Illustration of the effect of frequency shift on limit cycle amplitudes, first and second tangential modes; $(R/\bar{a})\alpha_{2T} = -0.1$, $\theta_{1T} = 0$

boundary is also easily identified in Eqs. (4.22) and (4.23). At the stability boundary, the denominator $2\alpha_{1T} + \alpha_{2T}$ is equal to zero, and the amplitudes become infinite.

As a side note, it is interesting that the analytical results for the first and second longitudinal modes obtained by Paparizos and Culick [51] display these same characteristics. The amplitude of the first longitudinal mode is given by

$$r_{1L}^2 = -\frac{\alpha_{1L}\alpha_{2L}}{\beta^2}\left[1 + \left(\frac{2\theta_{1L} - \theta_{2L}}{2\alpha_{1L} + \alpha_{2L}}\right)^2\right]. \tag{4.24}$$

Both the stability boundary and the effect of the linear frequency shifts are apparent. Of course, the frequency difference $\Omega_{2L} = 2\omega_{1L} - \omega_{2L}$ is equal to zero and does not appear in this equation. In addition, we can extend the requirement on linear frequency shifts to include higher modes for the longitudinal case. By induction, it is easy to show that $n\theta_{1L} - \theta_{nL} = 0$ leads to the most efficient energy transfer; see Eq. (4.4).

4.2.2 First Tangential and First Radial Modes

The time-averaged equations for this case are [55]

$$\frac{dr_{1T}}{dt} = \alpha_{1T} r_{1T} + a_R r_{1T} r_{1R} \cos X_R, \tag{4.25}$$

$$\frac{dr_{1R}}{dt} = \alpha_{1R} r_{1R} + b_R r_{1T}^2 \cos X_R, \tag{4.26}$$

$$\frac{dX_R}{dt} = -2\theta_{1T} + \theta_{1R} + \Omega_{1R} - \left(2a_R r_{1R} + b_R \frac{r_{1T}^2}{r_{1R}}\right) \sin X_R, \tag{4.27}$$

where

$$X_R(t) = 2\phi_{1T} - \phi_{1R} + \Omega_{1R} t,$$

$$\Omega_{1R} = 2\omega_{1T} - \omega_{1R},$$

$$a_R = 0.1570 \left(\frac{\bar{a}}{R}\right),$$

$$b_R = -0.1054 \left(\frac{\bar{a}}{R}\right).$$

It should first be noted that the natural frequency difference for the first radial mode $|\Omega_{1R}|$ is less than the frequency difference for the second tangential mode $|\Omega_{2T}|$. When the frequency shifts θ_n are set to zero as in the study by Yang and Culick, a smaller frequency shift is required from nonlinear processes than in the previous case. We would therefore expect the amplitudes to be smaller since the energy transfer between modes is more efficient. This is consistent with the numerical and analytical results obtained by Yang and Culick.

All of the previous observations apply for this case as well. In particular, the nonlinear coupling is most efficient when $2\theta_{1T} - \theta_{1R} - \Omega_{1R} = 0$, i.e.,

$$\omega_{1R} - \theta_{1R} = 2(\omega_{1T} - \theta_{1T}). \tag{4.28}$$

Yang and Culick found that the first radial mode also oscillates at twice the

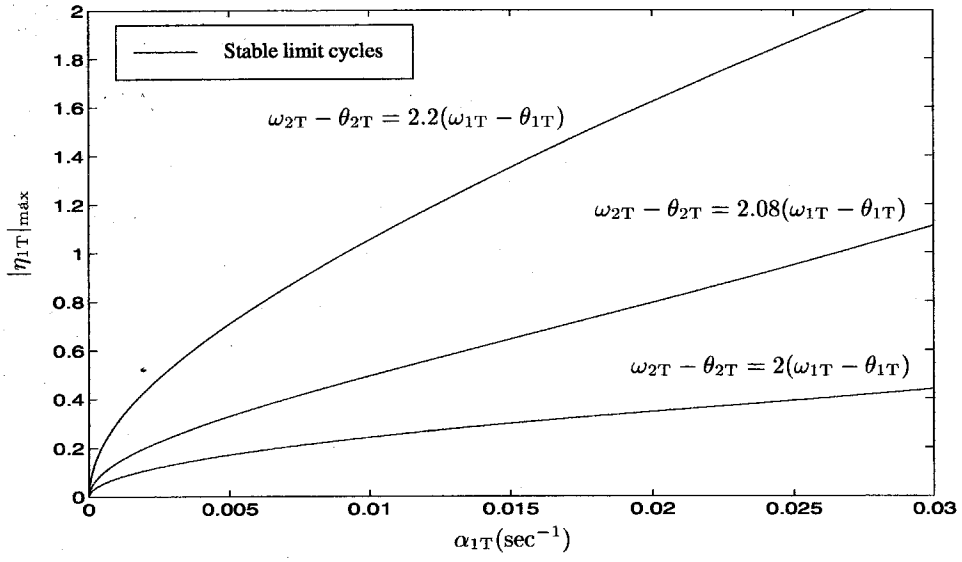

Figure 4.26 Illustration of the effect of frequency shift on limit cycle amplitudes, first tangential and first radial modes; $(R/\bar{a})\alpha_{1R} = -0.1$, $\theta_{1T} = 0$

frequency of the first tangential mode once a limit cycle is attained. Thus, when Eq. (4.28) is satisfied, nonlinear gasdynamics is only involved in transferring energy between modes and is thus very efficient.

As in the case of tangential oscillations, the linear frequency shifts can have a pronounced effect on the limit cycle amplitudes. Figure 4.26 shows bifurcation diagrams for three ratios of shifted frequencies. A ratio of 2.08 corresponds to the Yang and Culick case where $\theta_{1T} = \theta_{1R} = 0$. The amplitudes decrease as the ratio is decreased until a minimum is reached at a ratio of 2.

4.3 The Role of Nonlinear Gasdynamics in the Formation of Limit Cycles

Previous investigations have identified the role of nonlinear gasdynamics as a means of energy transfer between modes. The current results show that

nonlinear gasdynamics has an additional role in the formation of limit cycles, namely as a means of frequency shift.

Numerical simulations performed by Yang and Culick showed that in limit cycle, the second tangential mode oscillates at twice the frequency of the first tangential mode, even when the linear frequency shifts do not satisfy Eq. (4.20). The natural frequencies are not integral multiples of the fundamental for transverse modes, but the modes must necessarily oscillate at integral multiples of the shifted fundamental mode when in limit cycle. When Eq. (4.20) is not satisfied, nonlinear processes must shift the frequencies and maintain them at integral multiples of the fundamental. In the current chapter, nonlinear gasdynamics is the only nonlinear process and must therefore be responsible for any frequency shifts. It is apparent that when nonlinear gasdynamics is involved in shifting and maintaining frequencies, it is less efficient at transferring energy between modes. The higher the frequency shift, the less efficient the energy transfer becomes.

We will now take a brief look at the transient behavior of both $\cos X_{\mathrm{T}}$ and the total rate of energy transfer between modes for the case when $\theta_{1\mathrm{T}} = \theta_{2\mathrm{T}} = 0$. By comparing Figs. 4.27 and 4.28, we see that the evolution of $\cos X_{\mathrm{T}}$ occurs on a much smaller time scale than the total energy transfer. This implies that the frequency shift provided by nonlinear gasdynamics occurs on a smaller time scale as well. To show this, an approximation to the instantaneous frequency of oscillations was obtained using the zero crossings of η_n. For the purposes here, this approximation is sufficient since we are only interested in the transition time and not the details of the transition itself. Figure 4.29 shows the evolution of the oscillatory frequencies of the first and second tangential modes. As expected, the frequency of the second tangential mode quickly shifts to twice the frequency of the first mode and remains there for the duration.

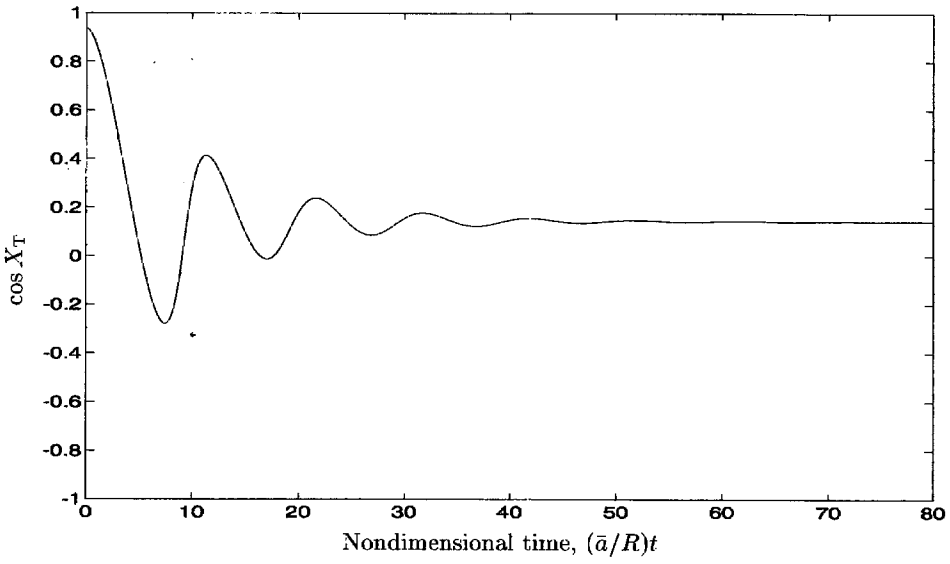

Figure 4.27 Time evolution of $\cos X_{\mathrm{T}}$ for the first and second tangential modes; $(R/\bar{a})\alpha_{1\mathrm{T}} = 0.001$, $(R/\bar{a})\alpha_{2\mathrm{T}} = -0.1$, $\theta_{1\mathrm{T}} = \theta_{2\mathrm{T}} = 0$

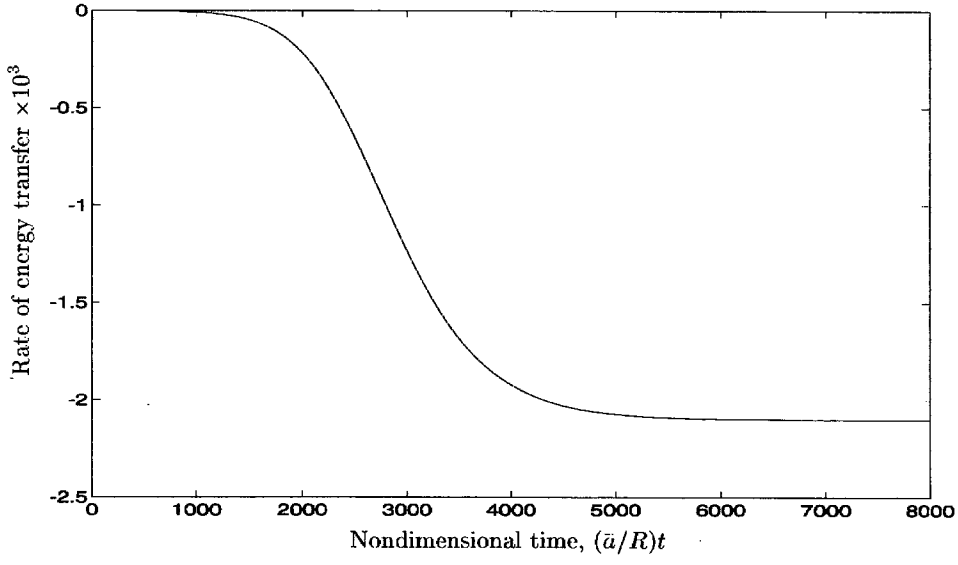

Figure 4.28 Total rate of energy transfer from the first to the second tangential mode; $(R/\bar{a})\alpha_{1\mathrm{T}} = 0.001$, $(R/\bar{a})\alpha_{2\mathrm{T}} = -0.1$, $\theta_{1\mathrm{T}} = \theta_{2\mathrm{T}} = 0$

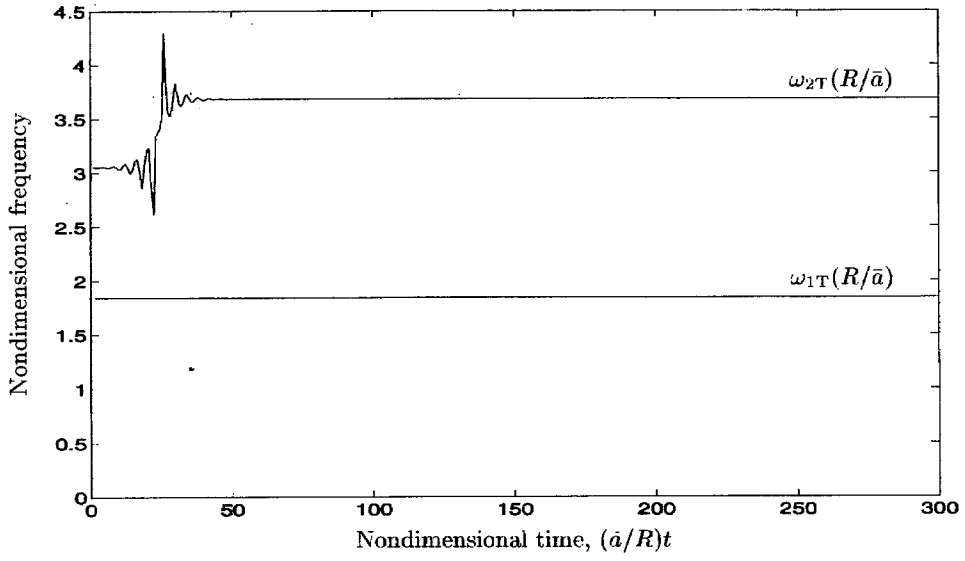

Figure 4.29 Time evolution of nondimensional frequencies for the first and second tangential modes; $(R/\bar{a})\alpha_{1T} = 0.001$, $(R/\bar{a})\alpha_{2T} = -0.1$, $\theta_{1T} = \theta_{2T} = 0$

4.4 Concluding Remarks

In the present chapter, several important results have been established. First, it was shown that results obtained using the time-averaged equations agree well with results from the original oscillator equations, as long as the amplitudes are not too large. However, it was also determined that the method of time-averaging introduces a stability boundary above which no stable limit cycles exist. Near this boundary, the amplitudes become large, and the results are no longer valid. As more modes are included in the analysis, the stability boundary shifts to a higher value of α. This extends the range over which the time-averaged equations agree closely with results from the original oscillator equations.

It has been determined that the stability boundary produced by the time-averaged equations is the result of zero energy transfer between modes. Moreover, the original oscillator equations are also affected by this breakdown in

energy transfer. Inspection of Figs. 4.2–4.5 reveals a marked increase in amplitudes at approximately the same location as the stability boundary. However, the original oscillator equations have additional coupling to higher modes which was averaged out by the method of time-averaging. This coupling allows the original oscillator equations to produce stable limit cycles past the stability boundary, although the amplitudes increase due to less efficient energy transfer. The two mode case is special as there is no coupling to higher modes. A turning point bifurcation is thus found near the time-averaged stability boundary due to insufficient energy transfer between the two modes.

Furthermore, it was determined that, in addition to its role of energy transfer between modes, nonlinear gasdynamics also provides a means of shifting the frequencies to integral multiples of the fundamental. By definition, the acoustic modes must oscillate at integral multiples when in a limit cycle. Therefore, if the linear processes do not shift the frequencies sufficiently, nonlinear gasdynamics must necessarily shift them if a limit cycle is to be reached. This additional role reduces the efficiency of gasdynamics in transferring energy between modes. Higher amplitude oscillations are thus attained. It happens that the frequency shift provided by nonlinear gasdynamics occurs at a much faster rate than the exponential growth of the amplitudes. This should be studied more closely to determine the reason for the two vastly different time scales.

The previous results demonstrate the importance of accurate modeling of linear processes. For transverse modes, the amplitudes are especially sensitive to the linear frequency shifts. In addition, results obtained using the approximate analysis may not be valid if the shifted frequencies differ substantially from integral multiples of the fundamental.

Chapter 5

Modeling the Nonlinear Combustion Response of a Solid Propellant

Combustion of a solid propellant is nonlinear chiefly for two reasons: chemical processes depend nonlinearly on both temperature and pressure; and the conversion of condensed material to gaseous products is a nonlinear function of the properties of the local flow field. Nonlinear behavior necessarily arises in any representation of the chemical kinetics, the strongest influence being due to the Arrhenius factor appearing in the usual formulas for the reaction rate. In the past, analysis of unsteady burning has been directed largely to investigating the response of burning to small fluctuations of the flow field in order to satisfy the needs for predicting linear stability. In particular, the response of burning to fluctuations in pressure has received the most attention; see Culick [10] for a review of calculations of the linear response function. Without a thorough analysis of the entire burning process, it is not possible to state unequivocally the form that the nonlinearity should take.

For the purposes here, the precise formula for nonlinear unsteady combustion is unimportant. We intend primarily to determine the effects of different nonlinear combustion models on the behavior of the system. We investigate the matter with models representing both pressure and velocity coupling. One

model represents nonlinear pressure coupling, and three represent velocity coupling. The pressure coupled model is derived by extending the derivation of a linear response function to include second-order terms. The first velocity coupled model was introduced by Baum and Levine [5, 45]. This model has been successfully used in comparisons of numerical results and observations of pulsed instabilities. The third model, proposed by Greene [32], is also based on the idea of velocity coupling but using a slightly different form than the Baum and Levine model. The final model is a modification of the Greene model to include the influence of a threshold velocity.

In order to be used in the present analysis, any model of unsteady combustion must be put in such a form as to fit into the appropriate terms in the forcing function given by Eq. (2.47). For gasdynamics up to second-order, the right-hand side of Eq. (2.46) can be written:

$$-\frac{\bar{p}E_n^2}{a^2}F_n = \bar{\rho}\int(\bar{\boldsymbol{u}}\cdot\nabla\boldsymbol{u}' + \boldsymbol{u}'\cdot\nabla\bar{\boldsymbol{u}})\cdot\nabla\psi_n dV + \frac{1}{a^2}\frac{\partial}{\partial t}\int(\bar{\gamma}p'\nabla\cdot\bar{\boldsymbol{u}} + \bar{\boldsymbol{u}}\cdot\nabla p')\psi_n dV$$

linear gasdynamics

$$+\bar{\rho}\int\left[\boldsymbol{u}'\cdot\nabla\boldsymbol{u}' + \frac{\rho'}{\bar{\rho}}\frac{\partial\boldsymbol{u}'}{\partial t}\right]\cdot\nabla\psi_n dV + \frac{1}{a^2}\frac{\partial}{\partial t}\int(\bar{\gamma}p'\nabla\cdot\boldsymbol{u}' + \boldsymbol{u}'\cdot\nabla p')\psi_n dV \tag{5.1}$$

nonlinear gasdynamics

$$+\oint\bar{\rho}\frac{\partial\boldsymbol{u}'}{\partial t}\cdot\hat{\boldsymbol{n}}\psi_n dS - \int\left[\frac{1}{a^2}\frac{\partial\mathcal{P}'}{\partial t}\psi_n + \boldsymbol{\mathcal{F}}'\cdot\nabla\psi_n\right]dV$$

linear and nonlinear surface processes

other contributions

The linear and nonlinear gasdynamics terms will be computed using the zeroth-order approximations (2.42) and (2.43) for the pressure and velocity. To the same order, the density fluctuation may be set equal to its isentropic value, $\rho'/\bar{\rho} = p'/\bar{\gamma}\bar{p}$, legitimate because we assume that there is no residual combustion within the chamber. Those terms labeled "other contributions," containing for example, interactions between the gas and condensed phase, will be ignored here.

It should be noted that the surface integral in Eq. (5.1) differs from the form used in Kim [42] and Greene [32]. In those representations, two additional terms are included in the surface integral. When deriving this equation, we have expanded in terms of two small parameters. It is necessary to keep terms consistently. The above representation is correct as derived.

As a means of accommodating nonlinear combustion of solid propellants, we are concerned with the remaining terms arising from unsteady processes on the boundary of the chamber. Part of this contribution is due to the exhaust nozzle and will be absorbed in the linear attenuation. For the nonlinear combustion, the term labeled "linear and nonlinear surface processes" is nearly equal to the time derivative of the second-order fluctuation of mass flux inward. The mass flux at the surface is defined as $\dot{\boldsymbol{m}} = \rho \boldsymbol{u}$ so that the fluctuating part becomes

$$\begin{aligned} \dot{\boldsymbol{m}}' &= \dot{\boldsymbol{m}} - \bar{\dot{\boldsymbol{m}}} \\ &= (\bar{\rho} + \rho')(\bar{\boldsymbol{u}} + \boldsymbol{u}') - \bar{\rho}\bar{\boldsymbol{u}} \\ &= \bar{\rho}\boldsymbol{u}' + \rho'(\bar{\boldsymbol{u}} + \boldsymbol{u}'). \end{aligned}$$

Because $\bar{\boldsymbol{u}}$ is independent of time, a form which can be directly substituted in Eq. (5.1) is obtained by taking the time derivative of the above equation and

rearranging terms.

$$\bar{\rho}\frac{\partial \boldsymbol{u}'}{\partial t}\cdot\hat{\boldsymbol{n}} = \frac{\partial \dot{\boldsymbol{m}}'}{\partial t}\cdot\hat{\boldsymbol{n}} - \rho'\frac{\partial \boldsymbol{u}'}{\partial t}\cdot\hat{\boldsymbol{n}} - \frac{\partial \rho'}{\partial t}(\bar{\boldsymbol{u}}+\boldsymbol{u}')\cdot\hat{\boldsymbol{n}} \tag{5.2}$$

It happens that analysis and modeling of unsteady combustion leads to results for mass fluctuation, but as shown by Eq. (5.1), the gasdynamics problem within the chamber requires the unsteady velocity as the boundary condition. Thus we can include contributions from nonlinear combustion by use of Eq. (5.2). Substitution of Eq. (5.2) into the surface process term of Eq. (5.1) gives

$$\begin{aligned}-\frac{\bar{p}E_n^2}{a^2}(F_n)_{\text{comb}} = &\oint \frac{\partial \dot{\boldsymbol{m}}'}{\partial t}\cdot\hat{\boldsymbol{n}}\psi_n dS \\ &- \oint \rho'\frac{\partial \boldsymbol{u}'}{\partial t}\cdot\hat{\boldsymbol{n}}\psi_n dS - \oint \frac{\partial \rho'}{\partial t}(\bar{\boldsymbol{u}}+\boldsymbol{u}')\cdot\hat{\boldsymbol{n}}\psi_n dS.\end{aligned} \tag{5.3}$$

To evaluate the last two integrals, the linear approximation for $\boldsymbol{u}'$ expressed in terms of the admittance function A_b will be used: [21]

$$-\boldsymbol{u}'\cdot\hat{\boldsymbol{n}} = aA_b\frac{p'}{\bar{\gamma}\bar{p}} \tag{5.4}$$

Using this approximation along with the isentropic assumption, $\rho' = \bar{\rho}p'/\bar{\gamma}\bar{p}$, yields

$$-\frac{\bar{p}E_n^2}{a^2}(F_n)_{\text{comb}} = -\int \frac{\partial \dot{m}'}{\partial t}\psi_n dS + \bar{\rho}\int\left(\bar{u}_b + 2aA_b\frac{p'}{\bar{\gamma}\bar{p}}\right)\frac{\partial}{\partial t}\left(\frac{p'}{\bar{\gamma}\bar{p}}\right)\psi_n dS, \tag{5.5}$$

where we have written $\bar{u}_b = -\bar{\boldsymbol{u}}\cdot\hat{\boldsymbol{n}}$ for the average velocity of the flow inward at the burning surface and $\dot{m}' = -\dot{\boldsymbol{m}}'\cdot\hat{\boldsymbol{n}}$ for the fluctuation of inward mass flux.

5.1 Second-Order Pressure Coupling

The linear response of a solid propellant to pressure fluctuations at the flame has been treated in many analyses, usually leading to the same two parameter expression as found by Denison and Baum [10, 23] if the only unsteady process accounted for is heat conduction in the condensed phase. The form of the two parameters depends on the models chosen for the solid and gas phases. Here, the nonlinear response function will be derived by retaining terms to second-order in fluctuations using the following models for the solid and gas phases: 1) the solid is assumed to be homogeneous and nonreactive with constant properties, 2) combustion is assumed to be uniformly distributed in a small region near the surface which begins immediately at the solid-gas interface, and 3) combustion responds quasi-statically to fluctuations in pressure only. The linear response for this special case has been previously treated by Culick [11], so many of the details will not be covered here.

5.1.1 The Solid Phase and Solid-Gas Interface

We begin with the energy balance at the solid-gas interface written to second-order in fluctuations.

$$\left(k_g \frac{dT}{dx}\right)'_{s+} = \left(k_p \frac{dT}{dx}\right)'_{s-} + (c_p - c)\bar{\dot{m}} T'_s + Q_s \dot{m}' + (c_p - c)\dot{m}' T'_s \qquad (5.6)$$

where the subscript s denotes the value at the solid-gas interface. Q_s is the heat released at the surface, while c_p and c are the specific heats of the gas and solid, respectively. This will be the main equation into which the solutions from the solid and gas phases will be substituted. Under the assumptions listed above, solution for the solid phase yields the fluctuation of heat transfer from

the interface to the solid.

$$\left(k_p \frac{dT}{dx}\right)'_{s^-} = \bar{\dot{m}} c \bar{T}_s \left[\lambda \frac{T'_s}{\bar{T}_s} + \frac{1 - T_c/\bar{T}_s}{\lambda} \frac{\dot{m}'}{\bar{\dot{m}}}\right], \tag{5.7}$$

where λ is a complex function of frequency found by solving the equation $\lambda(\lambda - 1) = i\kappa_p \omega / \bar{r}_b^2$; T_c is the temperature of the cold propellant.

To complete the analysis of the solid-gas interface, an assumption regarding the rate of conversion of solid to gas must be made. As is common practice, an Arrhenius Law will be used for pyrolysis at the surface.

$$\dot{m} = B_s T_s^{\beta_1} e^{-E_s/R_0 T_s} \tag{5.8}$$

Introducing mean and fluctuating quantities, we obtain a relation between the fluctuation of mass flux at the surface and the fluctuation of the surface temperature.

$$\frac{\dot{m}'}{\bar{\dot{m}}} = (\beta_1 + \bar{E}) \frac{T'_s}{\bar{T}_s} + \left[\frac{\beta_1(\beta_1 - 1)}{2} + \beta_1 \bar{E} + \left(\frac{\bar{E}^2}{2} - \bar{E}\right)\right] \left(\frac{T'_s}{\bar{T}_s}\right)^2, \tag{5.9}$$

where

$$\bar{E} \equiv \frac{E_s}{R_0 \bar{T}_s}. \tag{5.10}$$

Combining Eqs. (5.6), (5.7), and (5.9) leads to an equation relating the heat transfer from the gas to the solid-gas interface and the surface temperature fluctuations.

$$\left(k_g \frac{dT}{dx}\right)'_{s^+} = \bar{\dot{m}} c \bar{T}_s \left[C_1 \frac{T'_s}{\bar{T}_s} + C_2 \left(\frac{T'_s}{\bar{T}_s}\right)^2\right], \tag{5.11}$$

where

$$C_1 = \lambda + \frac{A}{\lambda} + \left(\frac{c_p}{c} - 1\right) - \frac{Q_s(\beta_1 + \bar{E})}{c\bar{T}_s},$$

$$C_2 = \left(\frac{c_p}{c} - 1\right)(\beta_1 + \bar{E}) + \left(\frac{1 - T_c/\bar{T}_s}{\lambda} - \frac{Q_s}{c\bar{T}_s}\right) \times \left[\frac{\beta_1(\beta_1 - 1)}{2} + \beta_1\bar{E} + \left(\frac{\bar{E}^2}{2} - \bar{E}\right)\right],$$

$$A = (\beta_1 + \bar{E})\left(1 - \frac{T_c}{\bar{T}_s}\right).$$

5.1.2 The Gas Phase

The solution for the gas phase gives another formula for the fluctuation of heat transfer to the solid-gas interface.

$$\left(k_g \frac{dT}{dx}\right)'_{s+} = \bar{\dot{m}} c_p \bar{T}_s \Lambda^2 \left[\frac{w'}{\bar{w}} - \frac{\dot{m}'}{\bar{\dot{m}}} - \frac{w'}{\bar{w}}\frac{\dot{m}'}{\bar{\dot{m}}} + \left(\frac{\dot{m}'}{\bar{\dot{m}}}\right)^2\right], \tag{5.12}$$

where

$$\Lambda^2 = \frac{Q_f k_g \bar{w}}{\bar{\dot{m}}^2 c_p^2 \bar{T}_s}.$$

This expression introduces an additional variable, the reaction rate w. Thus, we need another relation between the pressure and the reaction rate to complete the analysis. We assume that the reaction rate can be expressed as a function of pressure only and that the linear burning rate may be approximated by $\dot{m} = ap^n$. This leads to the following equation relating the reaction rate and pressure to second order,

$$\frac{c_p}{c}\left(\frac{\Lambda^2}{1 - T_c/\bar{T}_s}\right)\frac{w'}{\bar{w}} = W_1\frac{p'}{\bar{p}} + W_2\left(\frac{p'}{\bar{p}}\right)^2, \tag{5.13}$$

where

$$W_1 = 2n(1-H) + \frac{c_p}{c}\frac{n}{A},$$
$$W_2 = (2n^2 - n)(1-H) + \frac{2n^2}{A}\frac{c_p}{c} + \frac{c_p}{c}\frac{n(n-A)}{2A^2}.$$

Substitution of Eq. (5.13) into Eq. (5.12) yields

$$\left(k_g \frac{dT}{dx}\right)'_{s+} = \frac{\bar{\dot{m}} C \bar{T}_s}{(\beta_1 + \bar{E})}\left[W_1 A \frac{p'}{\bar{p}} + W_2 A \left(\frac{p'}{\bar{p}}\right)^2 - \frac{c_p}{c}(\beta_1 + \bar{E})\Lambda^2 \frac{\dot{m}'}{\bar{\dot{m}}} - W_1 A \frac{p'}{\bar{p}}\frac{\dot{m}'}{\bar{\dot{m}}} + \frac{c_p}{c}(\beta_1 + \bar{E})\Lambda^2 \left(\frac{\dot{m}'}{\bar{\dot{m}}}\right)^2\right]. \quad (5.14)$$

Finally, equating (5.14) and (5.11) followed by substitution for T'_s from Eq. (5.9) leads to the nonlinear response function. In the linear limit, the response function can be written in the two parameter form of Denison and Baum [23].

$$R_b^{\text{linear}} = \frac{\dot{m}'/\bar{\dot{m}}}{p'/\bar{p}} = \frac{nAB}{\lambda + A/\lambda - (1+A) + AB}, \quad (5.15)$$

with

$$B = 2\left(1 - \frac{Q_s}{c(\bar{T}_s - T_c)}\right) + \frac{c_p}{c}\frac{1}{A}. \quad (5.16)$$

Using this definition, the nonlinear response function is written as a function of the linear response function.

$$R_b^{\text{NL}} = R_b^{\text{linear}} + \left[\frac{W_2}{W_1} R_b^{\text{linear}} - \left(R_b^{\text{linear}}\right)^2 - \frac{D}{AW_1}\left(R_b^{\text{linear}}\right)^3\right]\left(\frac{p'}{\bar{p}}\right), \quad (5.17)$$

where

$$D = \left(\frac{c_p}{c} - 1\right)\left(1 - \frac{C_3}{C_4^2}\right) - \lambda\frac{C_3}{C_4^2} - \frac{c_p}{c}C_4\Lambda^2,$$
$$C_3 = \frac{\beta_1(\beta_1 - 1)}{2} + \beta_1\bar{E} + \left(\frac{\bar{E}^2}{2} - \bar{E}\right),$$
$$C_4 = \beta_1 + \bar{E}.$$

Both the linear and nonlinear response functions are complex quantities. When used in calculations of time-dependent motions, an approximation to R_b^{linear} can be made for pure oscillations (see Culick and Yang [21] for details):

$$[R_b^{(r)} + iR_b^{(i)}]e^{i\omega t} = \left[R_b^{(r)} + R_b^{(i)}\frac{1}{\omega}\frac{\partial}{\partial t}\right]e^{i\omega t} \tag{5.18}$$

Hence, to incorporate the linear response functions in the analysis, we may set

$$R_b^{\text{linear}} = R_b^{(r)} + R_b^{(i)}\frac{1}{\omega}\frac{\partial}{\partial t} \tag{5.19}$$

since to zeroth-order, we have pure oscillatory motions; ω is taken to be ω_n in the n^{th} oscillator equation. It is assumed that the nonlinear response function can be handled in the same manner.

$$R_b^{\text{NL}} = \text{Re}\left(R_b^{\text{NL}}\right) + \text{Imag}\left(R_b^{\text{NL}}\right)\frac{1}{\omega}\frac{\partial}{\partial t}, \tag{5.20}$$

with

$$\text{Re}\left(R_b^{\text{NL}}\right) = R_b^{(r)} + \left\{\frac{W_2}{W_1}R_b^{(r)} - \left(R_b^{(r)}\right)^2 + \left(R_b^{(i)}\right)^2 - \frac{D}{AW_1}\left[\left(R_b^{(r)}\right)^3 - 3R_b^{(r)}\left(R_b^{(i)}\right)^2\right]\right\}\frac{p'}{\bar{p}}, \tag{5.21}$$

$$\text{Imag}\left(R_b^{\text{NL}}\right) = R_b^{(i)} + \left\{ \frac{W_2}{W_1} R_b^{(i)} - 2R_b^{(r)} R_b^{(i)} + \frac{D}{AW_1}\left[\left(R_b^{(i)}\right)^3 - 3\left(R_b^{(r)}\right)^2 R_b^{(i)} \right] \right\} \frac{p'}{\bar{p}}. \quad (5.22)$$

Finally, the nonlinear pressure coupled model can be included by substituting the following formula for $\partial \dot{m}'/\partial t$ in the surface integral.

$$\frac{\partial \dot{m}'}{\partial t} = \frac{\bar{\dot{m}}}{\bar{p}} \frac{\partial}{\partial t}(p' R_b^{\text{NL}}) \quad (5.23)$$

5.2 Velocity Coupling

Motivated by observations suggesting that the response of a burning solid likely depends on the scouring effect of flow velocity parallel to the surface, McClure and his colleagues [34, 50] treated the corresponding phenomenon for unsteady motions. The idea is that changes in the burning rate of a solid may be dependent on changes of the magnitude but not the direction of the flow past the surface. The simplest possible cause of such behavior is associated with convective heat transfer. Whatever its true physical origin, this sort of nonlinear behavior is commonly referred to as "velocity coupling." Including this effect in analysis of the unsteady burning rate introduces essentially a kinematical nonlinearity.

The first models of velocity coupling were intentionally simplistic in order to be used in the available stability analysis programs. Later, three JANNAF workshops concluded that velocity coupling is still not well understood and that all existing models had serious physical deficiencies. Due to these deficiencies, Baum and Levine [45] developed an ad hoc model which produced good agreement with experiment. This model, as well as two other ad hoc models derived from it, will be used in the present analysis.

5.2.1 The Baum and Levine Model

In the experimental and theoretical investigation of pulsed instabilities by the Air Force Propulsion Laboratory, Baum and Levine [45] introduced a model of nonlinear combustion response based on the idea of velocity coupling. To obtain agreement between predicted behavior and observations, one parameter representing the response of combustion to the velocity parallel to the burning surface was changed. By changing only this parameter, they were able to match the growth rates, the limit cycle amplitudes, the mean pressure shift, and the waveform quite accurately. This suggests that the chosen nonlinearity must be fairly close to the important physical processes present in the experiments. Therefore, the first velocity coupling model will be the model introduced by Baum and Levine.

The Baum and Levine model is an ad hoc model in which the mass burning rate is directly modified by some function of the velocity [45]. For that reason it was originally called the 'burn rate augmentation model.' The total mass burning rate is written as a combination of linear pressure coupling and nonlinear velocity coupling as

$$\dot{m} = \dot{m}_{\mathrm{pc}}[1 + R_{\mathrm{vc}}F(\boldsymbol{u})], \tag{5.24}$$

where $\dot{m}_{\mathrm{pc}}$ is the mass flux due to pressure only and R_{vc} is a constant related to the sensitivity of burning to velocity parallel to the surface. Since the evolution rate of solid to gas should depend on the magnitude but not the direction of the scouring flow, and the simplest assumption is linear dependence, $F(\boldsymbol{u})$ is taken equal to $|\boldsymbol{u}'|$.

$$\dot{m} = \dot{m}_{\mathrm{pc}}[1 + R_{\mathrm{vc}}|\boldsymbol{u}'|] \tag{5.25}$$

We ignore the possible influence of mean flow speed and assume that the fluc-

tuation of mass flux depends on $|\boldsymbol{u}'|$, not on $|\bar{\boldsymbol{u}} + \boldsymbol{u}'|$. This is not an essential approximation but does simplify the numerical calculations by avoiding complications arising from the variation of the mean flow speed along the surface.

The fluctuation of $\dot{m}$ is calculated with Eq. (5.25),

$$\begin{aligned}\dot{m}' &= \dot{m} - \bar{\dot{m}} \\ &= (\dot{m}'_{\rm pc} + \bar{\dot{m}}_{\rm pc})[1 + R_{\rm vc}|\boldsymbol{u}'|] - \bar{\dot{m}}_{\rm pc} \\ &= \dot{m}'_{\rm pc}[1 + R_{\rm vc}|\boldsymbol{u}'|] + \bar{\dot{m}}_{\rm pc} R_{\rm vc}|\boldsymbol{u}'|.\end{aligned}$$

By definition of the response function R_b for linear pressure coupling [21],

$$\frac{\dot{m}'_{\rm pc}}{\bar{\dot{m}}} = R_b \frac{p'}{\bar{\gamma}\bar{p}}, \tag{5.26}$$

and we have

$$\frac{\dot{m}'}{\bar{\dot{m}}} = R_b \left(\frac{p'}{\bar{\gamma}\bar{p}}\right) + R_b R_{\rm vc} \left(\frac{p'}{\bar{\gamma}\bar{p}}\right) |\boldsymbol{u}'| + \frac{\bar{\dot{m}}_{\rm pc}}{\bar{\dot{m}}} R_{\rm vc}|\boldsymbol{u}'|. \tag{5.27}$$

Substitution of Eq. (5.27) in (5.5) gives

$$\begin{aligned}\frac{\bar{p}E_n^2}{a^2}(F_n)^{\rm BL}_{\rm comb} = {} & \frac{\bar{\dot{m}} R_b R_{\rm vc}}{\bar{\gamma}} \int \frac{\partial}{\partial t}\left[\frac{p'}{\bar{p}}|\boldsymbol{u}'|\right]\psi_n dS + \bar{\dot{m}}_{\rm pc} R_{\rm vc} \int \frac{\partial |\boldsymbol{u}'|}{\partial t}\psi_n dS \\ & - \frac{2\bar{\rho} a A_b}{\bar{\gamma}^2} \int \left(\frac{p'}{\bar{p}}\right) \frac{\partial}{\partial t}\left(\frac{p'}{\bar{p}}\right)\psi_n dS + \left\{\frac{\bar{\dot{m}}}{\bar{\gamma}} \int (R_b - 1)\frac{\partial}{\partial t}\left(\frac{p'}{\bar{p}}\right)\psi_n dS\right\}.\end{aligned}$$

For simplicity, assume that there is no steady erosive burning, so $\bar{\dot{m}}_{\rm pc} = \bar{\dot{m}} = \bar{\rho}\bar{u}_b$ and drop the linear terms in curly brackets, with the assumption that they are combined with other linear processes. Then the formula for the nonlinear

forcing function due to combustion is

$$(F_n)^{\mathrm{BL}}_{\mathrm{comb}} = \frac{\dot{\bar{m}}a^2}{\bar{p}E_n^2}\Big\{\frac{R_b R_{\mathrm{vc}}}{\bar{\gamma}}\int\frac{\partial}{\partial t}\left(\frac{p'}{\bar{p}}|\boldsymbol{u}'|\right)\psi_n dS + R_{\mathrm{vc}}\int\frac{\partial|\boldsymbol{u}'|}{\partial t}\psi_n dS - \frac{2A_b}{\bar{\gamma}^2\bar{M}_b}\int\left(\frac{p'}{\bar{p}}\right)\frac{\partial}{\partial t}\left(\frac{p'}{\bar{p}}\right)\psi_n dS\Big\}, \quad (5.28)$$

where $\bar{M}_b = \bar{\dot{m}}/\bar{\rho}a = \bar{u}_b/a$.

With a simple assumption we can reduce the number of parameters by one. From the definition of A_b and R_b [Culick and Yang [21], Eq. (93)],

$$A_b + \bar{M}_b = \bar{M}_b\left(R_b + \bar{\gamma}\frac{\Delta T_s/\bar{T}_s}{\eta_n/\psi_n}\right).$$

For the purposes here it is sensible to ignore non-isentropic fluctuations of temperature in the flame — set $\Delta T_{\mathrm{s}} = 0$ — and

$$\frac{A_b}{\bar{M}_b} = R_b - 1. \quad (5.29)$$

Hence Eq. (5.28) becomes

$$(F_n)^{\mathrm{BL}}_{\mathrm{comb}} = \frac{\bar{u}_b}{E_n^2}\Big\{C_1\int\frac{\partial}{\partial t}\left(\frac{p'}{\bar{p}}|\boldsymbol{u}'|\right)\psi_n dS + C_2\int\frac{\partial|\boldsymbol{u}'|}{\partial t}\psi_n dS - C_3\int\frac{p'}{\bar{p}}\frac{\partial}{\partial t}\left(\frac{p'}{\bar{p}}\right)\psi_n dS\Big\}, \quad (5.30)$$

with

$$C_1 = R_b R_{\mathrm{vc}},$$
$$C_2 = \frac{R_{\mathrm{vc}}}{\bar{\gamma}},$$
$$C_3 = \frac{2}{\bar{\gamma}}(R_b - 1).$$

The pressure coupled response function R_b will again be a complex quantity in general. Here, we will set $R_b^{(i)} = 0$ so that C_1 and C_2 are real constants. Such an arbitrary choice is within the intent of this paper to investigate the qualitative behavior, in particular to determine whether or not triggering can be found.

Application of Time-Averaging

The method of time-averaging is applied to the Baum and Levine model in much the same manner as described in Chapter 2. However, as originally outlined, the method is incapable of handling discontinuities introduced by $|\boldsymbol{u}'|$. Following the procedure introduced by Greene [32], an extension to the original method of time-averaging will be made in order to deal with these discontinuities.

First, $|\boldsymbol{u}'|$ can be written in terms of the sgn function as follows:

$$|\boldsymbol{u}'| = \mathrm{sgn}(\boldsymbol{u}')\boldsymbol{u}' \tag{5.31}$$

In order to simplify the analysis, we will use an approximation to $\mathrm{sgn}(\boldsymbol{u}')$ introduced by Kim [42] and used subsequently by Greene [32]. For the case of two longitudinal modes, $\mathrm{sgn}(\boldsymbol{u}')$ can be written as

$$\mathrm{sgn}(\boldsymbol{u}') = -\mathrm{sgn}(\dot{\eta}_1)\mathrm{sgn}(1 + \frac{\dot{\eta}_2}{\dot{\eta}_1}\cos k_1 x). \tag{5.32}$$

If we assume that $|\dot{\eta}_2/\dot{\eta}_1| < 1$ for all time, we obtain a useful approximation to $\mathrm{sgn}(\boldsymbol{u}')$.

$$\mathrm{sgn}(\boldsymbol{u}') \approx -\mathrm{sgn}(\dot{\eta}_1) \tag{5.33}$$

While the assumption $|\dot{\eta}_2/\dot{\eta}_1| < 1$ is not always satisfied in general, the higher

frequency content will be averaged out when time-averaging is applied, as noted by Greene. Therefore, the approximation (5.33) should be reasonable for both the two mode case and cases involving a higher number of modes.

The main simplification introduced by using approximation (5.33) is that the term $\mathrm{sgn}(\boldsymbol{u}')$ no longer depends on both space and time; it is now only a function of time. It is also useful to note that during the period of integration, $\dot{\eta}_1$ changes sign only once. Thus, when the method of time-averaging is applied to a term involving $|\boldsymbol{u}'|$, the time integral can be split into two parts, both of which have an analytic solution.

The splitting of the time integrals is most easily accomplished if we write $\dot{\eta}_1$ in terms of r_1 and ϕ_1 so that $\mathrm{sgn}(\dot{\eta}_1)$ becomes

$$\mathrm{sgn}(\dot{\eta}_1) = \mathrm{sgn}[\cos(\omega_1 t + \phi_1)]. \tag{5.34}$$

Equivalently, this can be written as

$$\mathrm{sgn}(\dot{\eta}_1) = \begin{cases} +1 & \text{if } t_0 \leq t \leq t_1, \\ -1 & \text{if } t_1 \leq t \leq t_2, \end{cases} \tag{5.35}$$

where

$$\begin{aligned} t_0 &= (-\pi/2 - \phi_1)/\omega_1, \\ t_1 &= (\pi/2 - \phi_1)/\omega_1, \\ t_2 &= (3\pi/2 - \phi_1)/\omega_1. \end{aligned}$$

Finally, the first two terms in the Baum and Levine model can be time-averaged by rewriting the term as $\mathrm{sgn}(\dot{\eta}_1)$ times some remaining term, then

integrating the result as follows:

$$\int_t^{t+\tau_1} \mathrm{sgn}(\dot{\eta}_1)[*]dt' = \int_{t_0}^{t_1} [*]dt' - \int_{t_1}^{t_2} [*]dt', \tag{5.36}$$

where $[*]$ is the remaining part of the term to be averaged.

5.2.2 Greene's Model

Greene [32] carried out calculations with a response dependent on the absolute value of the velocity,

$$\dot{m}' = \bar{\dot{m}} C_4 |\boldsymbol{u}'|. \tag{5.37}$$

Substitution in Eq. (5.5) and omission of the linear terms as in Sec. 5.2.1 gives the result corresponding to Eq. (5.28),

$$(F_n)^{\mathrm{G}}_{\mathrm{comb}} = \frac{\bar{u}_{\mathrm{b}}}{E_n^2} \left\{ C_4 \int \frac{\partial |\boldsymbol{u}'|}{\partial t} \psi_n dS - C_3 \int \left(\frac{p'}{\bar{p}}\right) \frac{\partial}{\partial t} \left(\frac{p'}{\bar{p}}\right) \psi_n dS \right\}. \tag{5.38}$$

Thus Greene's model leads to two of the three terms appearing in the Baum and Levine model represented by Eq. (5.30).

5.2.3 Threshold Velocity Model

Threshold effects have been observed in experimental investigations of velocity coupling. Ma et al. [47] used subliming dry ice to simulate the flow in a solid propellant rocket motor. A piston was used to generate acoustic waves in the chamber. The investigation found a threshold acoustic velocity above which the mean mass flux increased linearly with the Reynold's number of the acoustic fluctuations. Below the threshold value, the mean mass flow was approximately constant. The increased mass flux was determined to be a result of increased heat transfer to the surface after transition to turbulent

flow had occurred.

To determine the possible influences of such a threshold in this investigation, Greene's model will be modified to include a threshold velocity. Instead of using a direct dependence on the magnitude of velocity, the following model for the mass flux will be used.

$$\dot{m}' = \bar{\dot{m}} R_{\text{vc}} F(\boldsymbol{u}') \tag{5.39}$$

Figure 5.1 shows the function of velocity which will be used in the threshold velocity model. This function introduces a dead zone in which the nonlinear

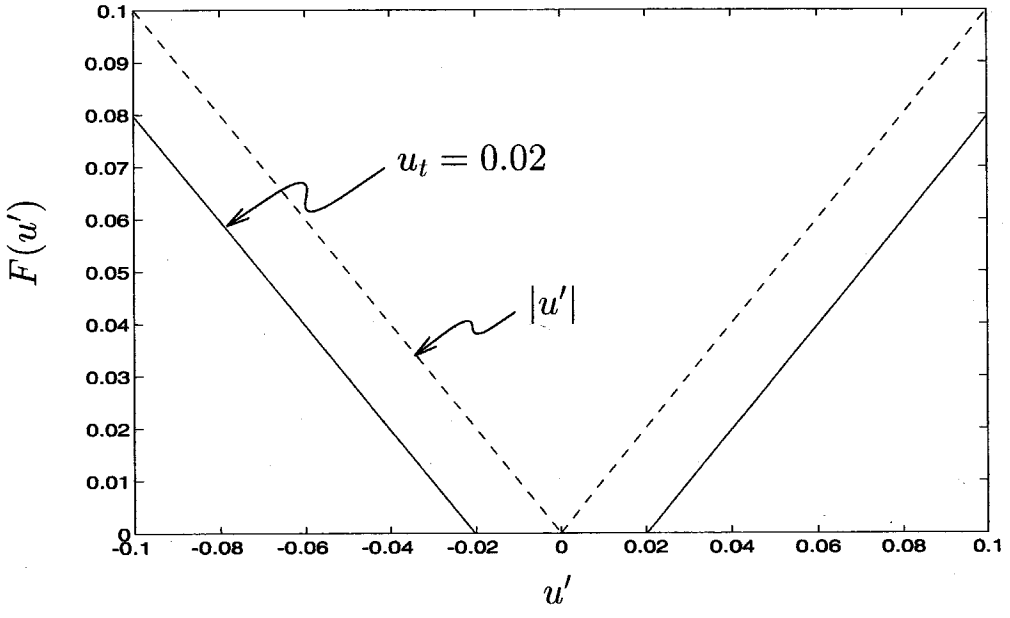

Figure 5.1 Function of velocity to be used in the threshold velocity model; $u_t = 0.02$

contribution from combustion does not affect the system. When the amplitudes of oscillations become larger than the chosen threshold value u_t, the nonlinear effects are then felt.

5.3 Discussion of Results

For solid-propellant rockets, problems of pulsed instabilities arise only in motors having relatively high L/D and involve mainly axial fluctuations. Therefore, for the numerical results in this section, we will treat the case of longitudinal modes only.

5.3.1 Nonlinear Pressure Coupling

Even for small amplitude oscillations, the nonlinear response function can differ substantially from the linear response function as shown in Figs. 5.2 and 5.3 for $A = 6.0$ and $B = 0.55$. When $p'/\bar{p} = 0.01$, the second-order terms increase the magnitudes of both the real and imaginary parts of the response function substantially. Nonetheless, no cases of triggering have been found for these parametric values, as well as other realistic values of A and B. The parameter space is large, so it is quite possible that this nonlinear model could lead to triggering for some values. So far, however, the search has been unsuccessful.

For the case of nonlinear pressure coupling, it is important to know the linear stability boundary of the propellant response. Culick [10] reported the following stability criterion for the parameters of the linear response function.

$$A < \frac{(B+1)}{(B-1)^2} \tag{5.40}$$

If this condition is not met, the propellant is intrinsically unstable and the values of A and B are not realistic.

Interestingly, triggering to stable limit cycles was found for values of A and B outside this stability limit. The values given in Appendix B yield $A = 6.0$ and $B = 0.486$, which are located just outside the stability boundary. As a result, the response functions are quite different from those when Eq. (5.40) is

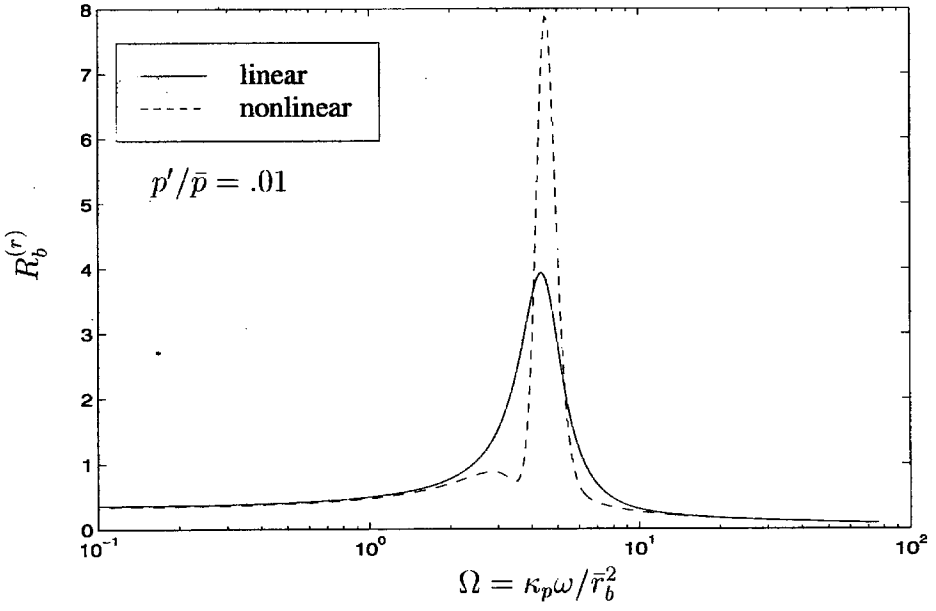

Figure 5.2 Real part of the linear and nonlinear propellant response functions vs. nondimensional frequency; $A = 6.0$, $B = 0.55$, $n = 0.3$

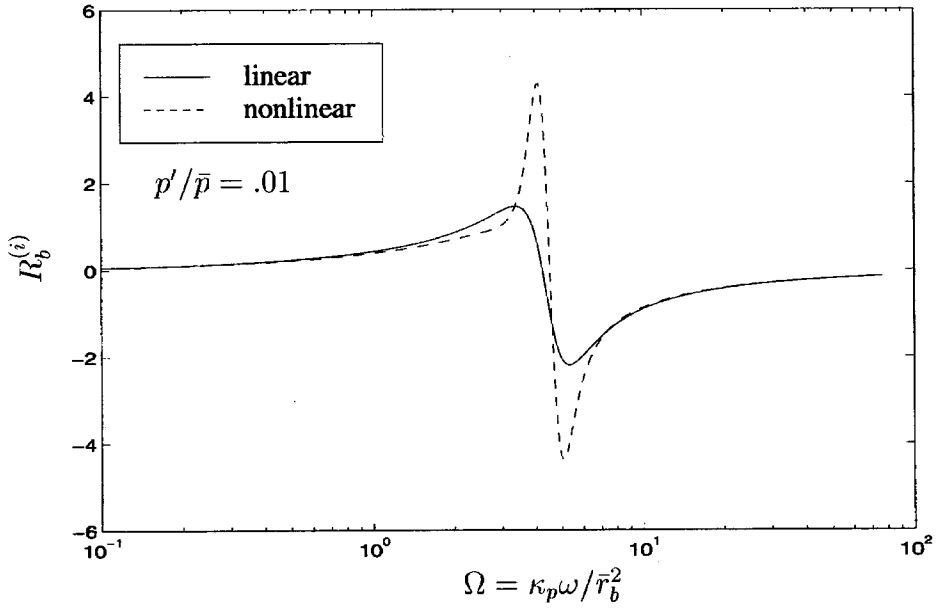

Figure 5.3 Imaginary part of the linear and nonlinear propellant response functions vs. nondimensional frequency; $A = 6.0$, $B = 0.55$, $n = 0.3$

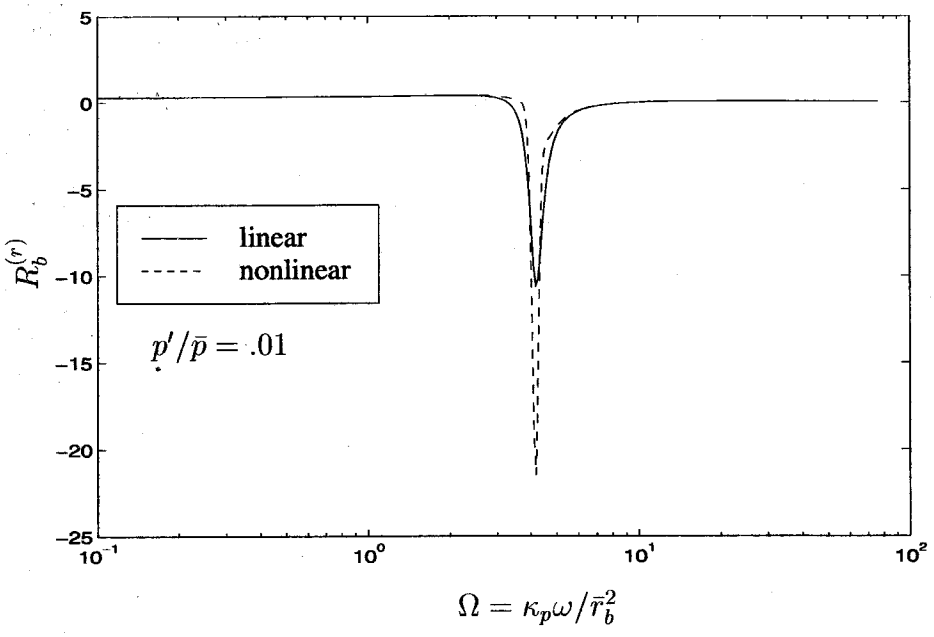

Figure 5.4 Real part of the linear and nonlinear propellant response functions vs. nondimensional frequency; $A = 6.0$, $B = 0.486$, $n = 0.3$

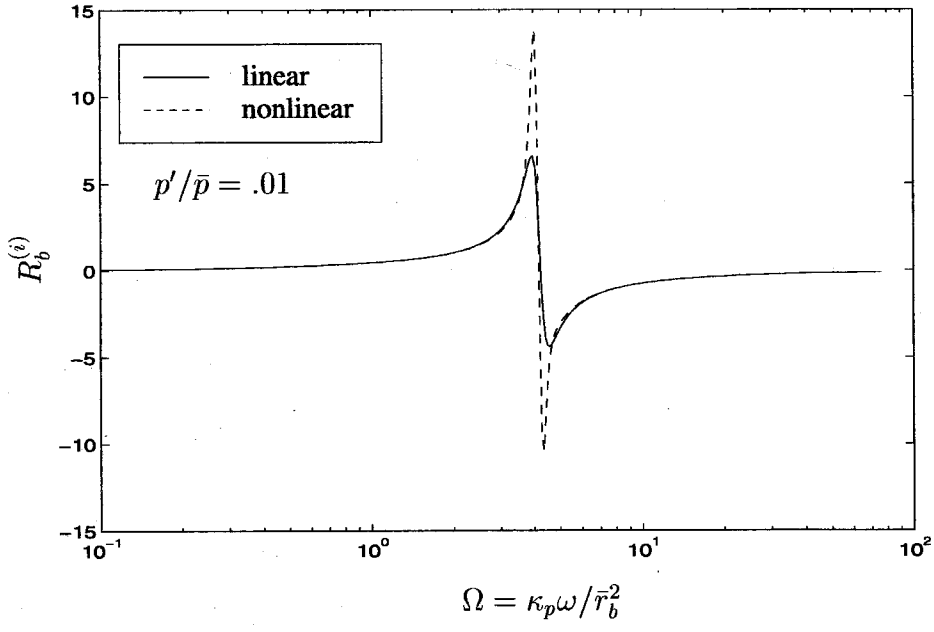

Figure 5.5 Imaginary part of the linear and nonlinear propellant response functions vs. nondimensional frequency; $A = 6.0$, $B = 0.486$, $n = 0.3$

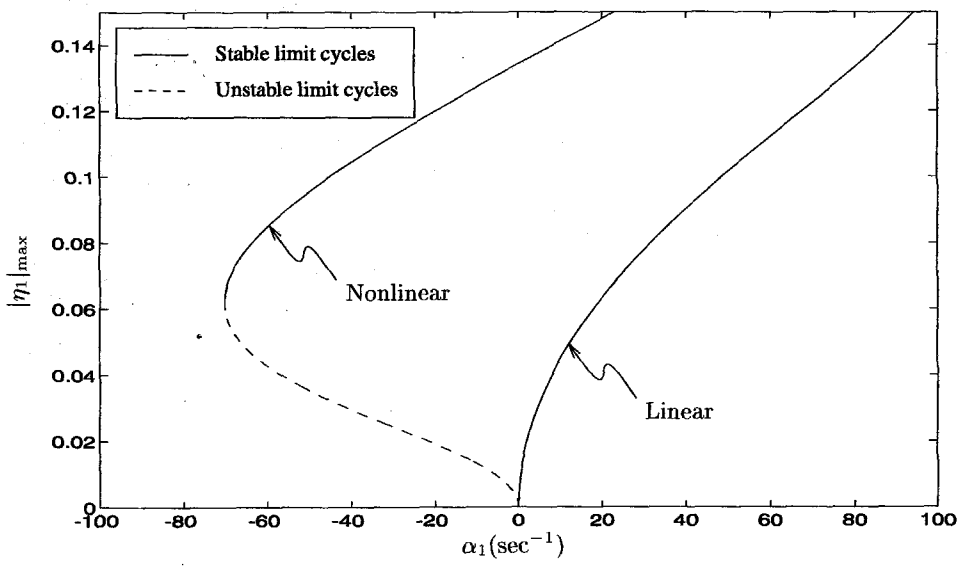

Figure 5.6 Maximum amplitude in limit cycle of first acoustic mode with linear and nonlinear pressure coupling; two modes, $A = 6.0$, $B = 0.486$

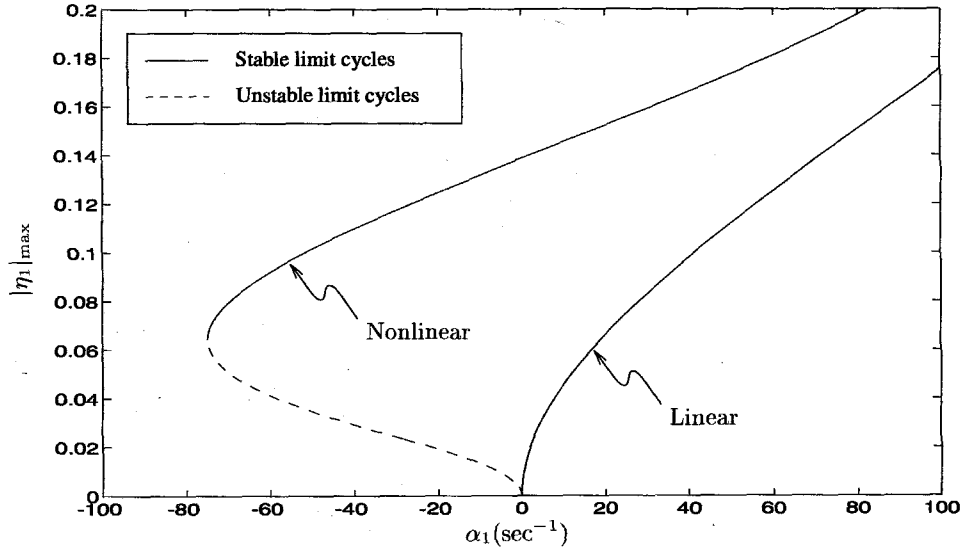

Figure 5.7 Maximum amplitude in limit cycle of first acoustic mode with linear and nonlinear pressure coupling; four modes, $A = 6.0$, $B = 0.486$

satisfied, as shown in Figs. 5.4 and 5.5. Results for truncation to two and four modes are displayed in Figs. 5.6 and 5.7. In both cases, a substantial region of possible triggering was found. We have no explanation for this behavior at the present time. Although the values of A and B are unrealistic, this case may be useful by providing a better understanding of the possible causes of triggering and should be studied in more detail in the future.

5.3.2 Velocity Coupling

We will now consider the models representing coupling to velocity oscillations. All models are derived from the Baum and Levine model, so we will begin with it. Substitution of Eqs. (2.42) and (2.43) in Eq. (5.30) yields, for longitudinal modes,

$$(F_n)^{\mathrm{BL}}_{\mathrm{comb}} = \frac{2(L/D)}{\bar{\gamma}\pi^2}\frac{\bar{u}_\mathrm{b}}{a}\Bigg\{ \underbrace{-2R_b\bar{R}_{\mathrm{vc}}\sum_{i=1}^{\infty}\sum_{j=1}^{\infty}\left[\frac{\dot{\eta}_i\dot{\eta}_j}{i} - i\omega_1^2\eta_i\eta_j\right] I^{(A)}_{nij}}_{A} + \underbrace{\frac{4\omega_1^2\bar{R}_{\mathrm{vc}}}{\bar{\gamma}}\sum_{i=1}^{\infty} i\eta_i I^{(B)}_{ni}}_{B} \underbrace{- 4\omega_1(R_b-1)\sum_{i=1}^{\infty}\sum_{j=1}^{\infty}\eta_i\dot{\eta}_j I^{(C)}_{nij}}_{C}\Bigg\}, \quad (5.41)$$

where $\bar{R}_{\mathrm{vc}} = R_{\mathrm{vc}}a$ and

$$I^{(A)}_{nij} = \int_0^\pi \cos n\tilde{x}[\sin(i-j)\tilde{x} + \sin(i+j)\tilde{x}]\mathrm{sgn}(u')d\tilde{x}, \quad (5.42a)$$

$$I^{(B)}_{ni} = \int_0^\pi \cos n\tilde{x}\sin i\tilde{x}\,\mathrm{sgn}(u')d\tilde{x}, \quad (5.42b)$$

$$I^{(C)}_{nij} = \int_0^\pi \cos n\tilde{x}[\cos(i-j)\tilde{x} + \cos(i+j)\tilde{x}]d\tilde{x}, \quad (5.42c)$$

with $\tilde{x} = \pi x/L$. Thus, the Baum and Levine model consists of three different terms, two of which make up Greene's model. Due to the discontinuity introduced by $\mathrm{sgn}(u')$, the integrals $I^{(A)}_{nij}$ and $I^{(B)}_{ni}$ will be evaluated numerically

using the trapezoidal rule.

One purpose of the following calculations is to determine what effect each term has on the system. In particular, we would like to answer the question: which terms are sufficient to produce triggering for reasonable values of $\bar{R}_{vc}$ and/or R_b? Another purpose of the present analysis is to determine the effects of truncation to a small number of modes and time-averaging.

Initial Results - The Discrepancy between the Time-Averaged and Original Oscillator Equations

The initial results for velocity coupling showed a substantial difference in the behaviors predicted by the original oscillator equations and the time-averaged equations. As shown in Fig. 5.8, the original oscillator equations produced a subcritical Hopf bifurcation at the origin with a very low amplitude unstable branch of periodic solutions. The time-averaged equations, however, produced a much different result. The Hopf bifurcation, usually found at the origin, was shifted to a negative value of α_1. Depending on the value of $\bar{R}_{vc}$ and the number of modes included, this bifurcation can be either subcritical or supercritical. An example is shown in Fig. 5.9 for four modes and several values of $\bar{R}_{vc}$. Whenever the time-averaged equations produced a subcritical bifurcation, the region of possible triggering was always much smaller than the region predicted by the original oscillator equations.

This discrepancy was a very puzzling result. The two sets of equations should, after all, produce very similar results in the linear limit. Nonetheless, it was first believed that this discrepancy was caused by application of the method of time-averaging since one of the nonlinear terms was first-order. After further consideration, it is now apparent that this discrepancy is the result of an approximation introduced while applying the continuation method to the original oscillator equations.

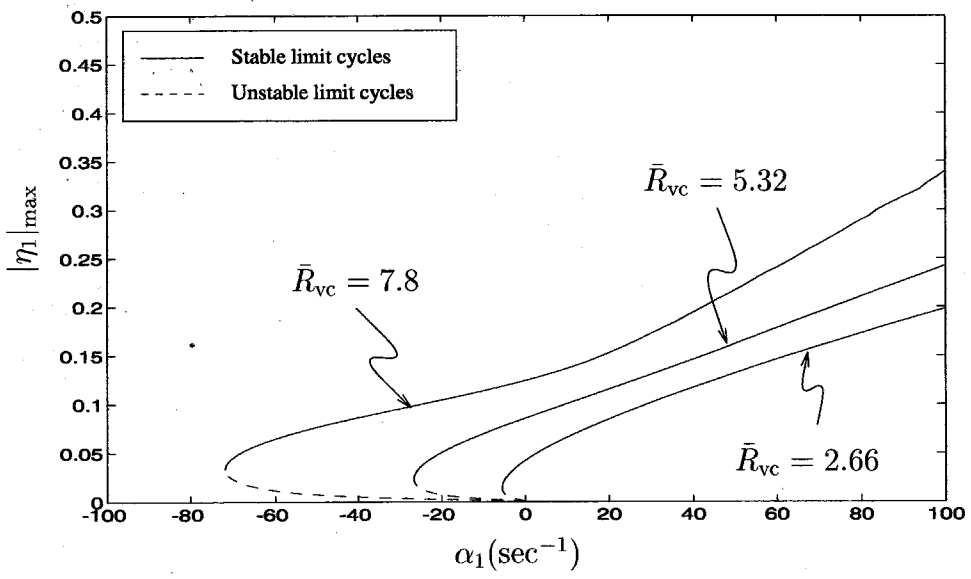

Figure 5.8 Initial results for the original oscillator equations: maximum amplitude of first acoustic mode in limit cycle using Greene's model and various values of $\bar{R}_{vc}$; four modes

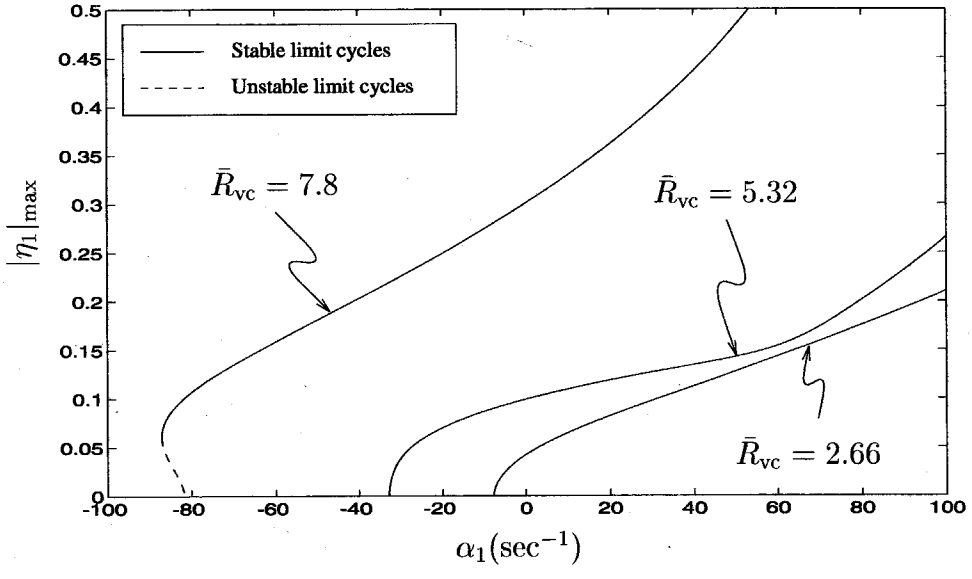

Figure 5.9 Maximum amplitude of first acoustic mode in limit cycle using Greene's model with the time-averaged equations and various values of $\bar{R}_{vc}$; four modes

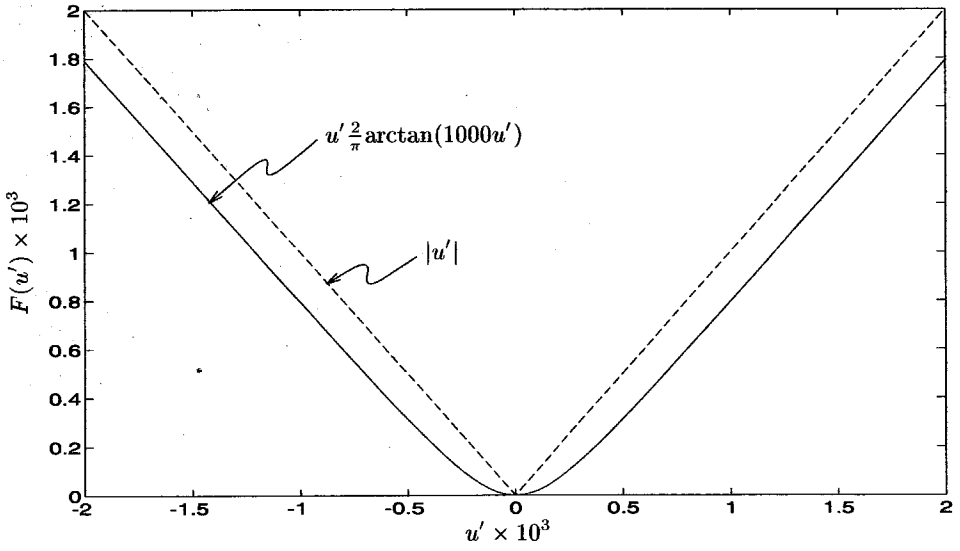

Figure 5.10 Approximation to $|\boldsymbol{u}'|$ using the arctan function

As mentioned earlier in Chapter 3, the continuation method is based on the implicit function theorem which requires that all functions are continuously differentiable. In order to meet this requirement when using either of the velocity coupled models, an approximation to $|\boldsymbol{u}'|$ is needed. The initial results such as those presented in Fig. 5.8 utilized $|\boldsymbol{u}'| \approx \boldsymbol{u}'\frac{2}{\pi}\arctan(1000\boldsymbol{u}')$. As Fig. 5.10 illustrates, the agreement is not good near $\boldsymbol{u}' = 0$. Although this approximation was necessary in order to use the continuation method, it changed the nature of the equations by introducing an "artificial" threshold velocity. This threshold, while very small, introduces a dead zone so that for very small disturbances, the effect of nonlinear combustion is absent. The behavior of the system is thus changed from a shifted spontaneous oscillation to an apparent region of possible triggering. The original oscillator equations should in fact produce results similar to those predicted by the time-averaged equations.

To prove that this was the case, a more accurate method was developed which does not require use of the sign approximation. The new method pro-

duces more accurate results for the branch of periodic solutions, but it cannot accommodate steady state calculations due to the discontinuity at $\boldsymbol{u}' = 0$. Therefore, calculations must begin at a numerically calculated limit cycle instead of at the Hopf bifurcation point. A brief description of the method will be given, although most of the programming details will be left out.

The first step is to numerically generate one complete cycle of the periodic solution using a simulation program. A cubic spline interpolation routine is used to calculate numerical values of the limit cycle at intermediate points when they are needed for the continuation method. After a properly discretized solution has been obtained, the continuation method can then proceed as normal with one modification: the integrals in the velocity coupled model will be integrated exactly instead of numerically as before.

The integrals $I_{nij}^{(A)}$ and $I_{ni}^{(B)}$ will be handled in the following manner. For a given number of modes n, there can be at most $n-1$ zero crossings of $\boldsymbol{u}'$ for x in the range of 0 to L (this depends on the current values of $\dot{\eta}_1$, $\dot{\eta}_2$, etc.). After determining the location of these zero crossings, the integral can be split into parts, each of which can be integrated exactly.

This method has been applied only for the case of two modes since the zero crossings can be determined analytically. It should work for a higher number of modes as well, although the zero crossings must be located by numerical means. Results for a two mode case using Greene's model are shown in Fig. 5.11. As suspected, the original oscillator equations produce an α-shifted Hopf bifurcation, similar to the results obtained using the time-averaged equations. Both sets of equations agree qualitatively, but the time-averaged equations predict much larger amplitudes than the original oscillator equations.

Results obtained for the four mode, time-averaged equations were also compared to the exact, two mode results, as seen in Fig. 5.12. Not only is the location of the Hopf bifurcation point more accurately predicted, but

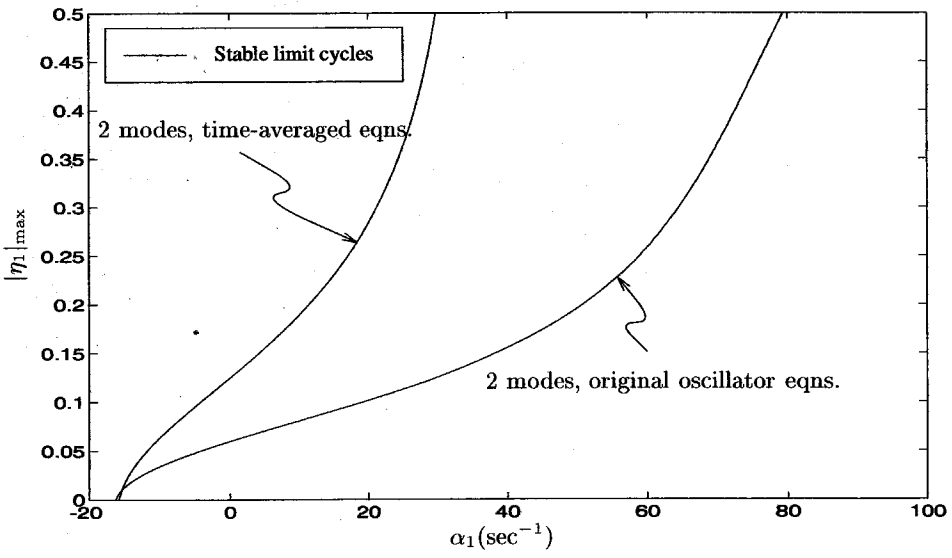

Figure 5.11 Comparison of results for the original oscillator and time-averaged equations using Greene's model; $\bar{R}_{vc} = 3.8$, two modes

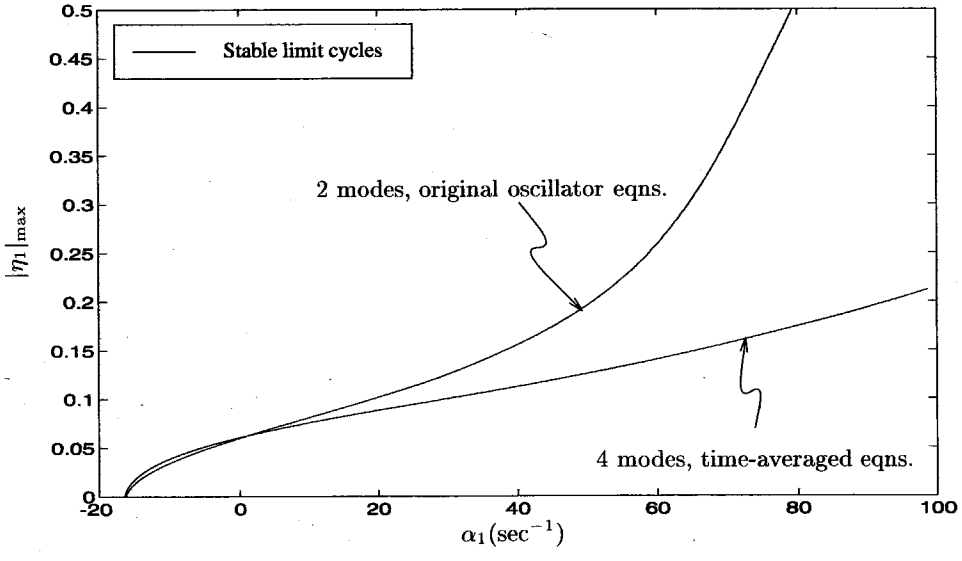

Figure 5.12 Comparison of results for the two mode, original oscillator equations and the four mode, time-averaged equations using Greene's model; $\bar{R}_{vc} = 3.8$

the agreement is better for a larger range of α_1, as we might expect. It is clear from these examples that the time-averaged equations can produce good quantitative and qualitative results, as long as a sufficient number of modes is included. We will therefore use the time-averaged equations to obtain further results for the velocity coupled models.

Although the initial results obtained using the original oscillator equations were misleading, the discrepancy between the two results suggested that a threshold velocity might be important in triggering. This was the motivation behind the threshold velocity model: to study the effects of a true threshold velocity. Results obtained using the threshold velocity model will be discussed in a later section.

This discussion of the initial results for the velocity coupled models illustrates the usefulness of dynamical systems theory in the study of combustion instabilities. Using only numerical simulations, it would have been extremely difficult to find the cause of this discrepancy. Bifurcations and accurate prediction of their locations are fundamental in understanding the behavior of a nonlinear system.

Further Results for the Velocity Coupled Models

We will now study the two velocity coupled models in more detail. Previous investigations have found regions of possible triggering using variations of these two models, but only when the system was truncated to two modes.

The investigation by Kim [42] used the Baum and Levine model to study triggering in solid propellant rocket motors. The manner in which the model was developed led to only one of the three terms in the Baum and Levine model. Therefore, in the investigation, only term A of Eq. (5.41) was included. Regions of possible triggering were found using this term, although the amplitudes of the limit cycles were quite high, perhaps outside the range

of validity of the approximate analysis.

The model introduced by Greene [32] consists of the remaining two terms of the Baum and Levine model. However, in the development of the original equations, Greene kept some higher order terms which should have been dropped in order to be consistent. As a result, term C of Eq. (5.41), which should be included in his model, was not taken into account. Using only term B in the analysis, limited cases of triggering were reported for the two mode, time-averaged equations. Therefore, we will now investigate the three terms, both individually and together, to determine which, if any, are capable of producing pulsed oscillations. In addition, we will study the effects of truncation to two modes, an approximation used by both Kim and Greene without proper consideration of the possible consequences.

The Effects of Individual Terms

The three terms of the Baum and Levine model, labeled A, B, and C in Eq. (5.41), represent three different types of nonlinear combustion response. By using each of these terms individually with the time-averaged equations and/or the original oscillator equations, their effect and relative importance will be determined.

The first term in the Baum and Levine model, term A, represents coupling to both pressure and velocity oscillations and thus depends on both R_b and $\bar{R}_{\mathrm{vc}}$. Figure 5.13 indicates that for truncation to two and four modes, this term produces the possibility of triggering, shown by a region of stable limit cycles for $\alpha_1 < 0$ sec^{-1}. A value of 2.18 was used for the linear pressure coupled response function, R_b. This value was used in the study by Baum, Levine, and Lovine[5] and seems to be a reasonable choice. The value of 16.15 for the velocity coupled response function was chosen to give a sizable region of triggering. This value seems high based on results obtained by Levine

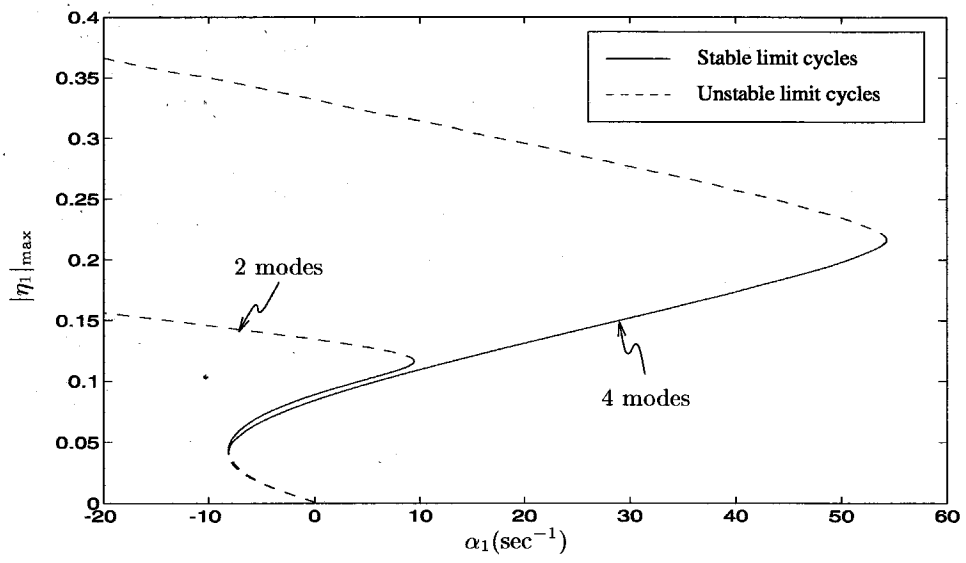

Figure 5.13 Maximum amplitude of first acoustic mode using term A with the original oscillator equations; two and four modes; $\bar{R}_{vc} = 16.15$, $R_b = 2.18$

and Baum [45]. In their study, $\bar{R}_{vc} = 5$ produced acceptable amplitudes, while $\bar{R}_{vc} = 13$ yielded amplitudes well outside the range of validity of the approximate analysis.

If the value of $\bar{R}_{vc}$ is increased even higher, it was found that eventually, the coupling to combustion processes becomes so strong that triggering is no longer possible. In order to explain this observation, a two parameter continuation using $\bar{R}_{vc}$ as a second free parameter was employed to plot the loci of turning points. The result is shown in Fig. 5.14. As $\bar{R}_{vc}$ is increased from zero, a turning point defining the lower limit of possible triggering is created at $\alpha_1 = 0$ sec^{-1} and shifts to the left. The upper turning point also shifts to the left as $\bar{R}_{vc}$ is increased. At a value of $\bar{R}_{vc} = 22.8$, the loci of turning points meet. Above this value, the coupling of velocity oscillations to combustion processes becomes so strong that nonlinear gasdynamics is not able to transfer energy at a sufficient rate to maintain a stable limit cycle. Therefore, the possibility of triggering does not exist above this value. The

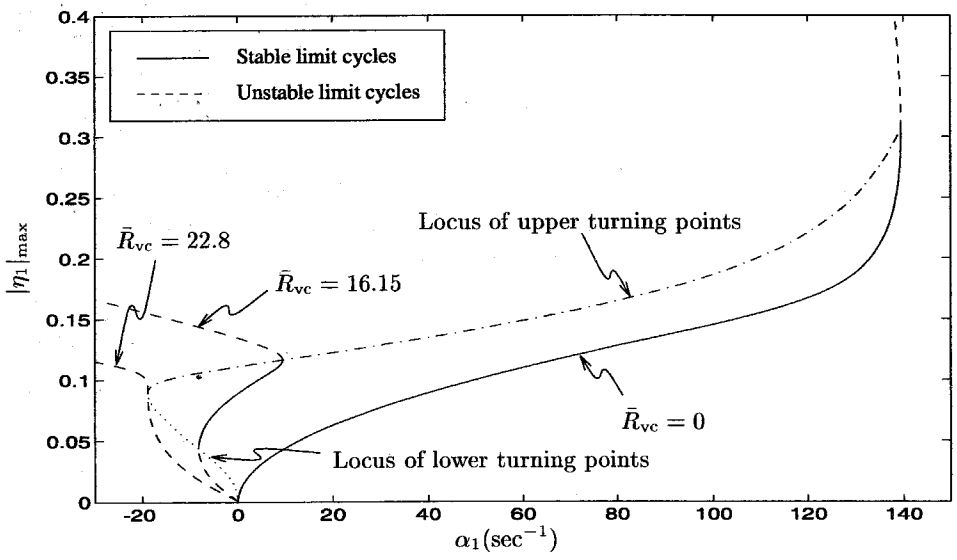

Figure 5.14 Loci of turning point bifurcations for the first acoustic mode, original oscillator equations using term A; two modes; $R_b = 2.18$

four mode case produced similar results, although the loci met at a higher value of $\bar{R}_{vc}$. It will be shown later that for more reasonable values of $\bar{R}_{vc}$, the term A, the first term in Eqs. (5.30) and (5.41), will have a rather small effect on the system.

The second term in Eq. (5.41), labeled B, represents coupling to velocity oscillations only. Using only this term, Greene [32] showed that regions of possible triggering occur when the system is truncated to two modes. The present results are consistent with Greene's findings, as seen in Fig. 5.15 for $\bar{R}_{vc} = 5.32$. A two parameter continuation was used to plot the locus of turning point bifurcations as $\bar{R}_{vc}$ is increased. Term B is a first-order term, and as such, it introduces an α-shift as $\bar{R}_{vc}$ is increased from 0. The Hopf bifurcation is initially supercritical so that pulsed oscillations are not possible. However, as the linear cross-coupling becomes stronger, the Hopf bifurcation can change from supercritical to subcritical, depending on the number of modes and other parameters of the system. For the two mode case, all values of $\bar{R}_{vc}$ greater

than 0.94 produce a subcritical bifurcation, thus yielding the possibility of triggering to a stable limit cycle.

When four modes are included in the analysis, the transition point at which the Hopf bifurcation changes from supercritical to subcritical occurs at a higher value of $\bar{R}_{vc}$. Inspection of Fig. 5.16 shows that this transition occurs at $\bar{R}_{vc} = 5.93$. Above this value, regions of possible triggering are found, although the regions are quite small for reasonable values of $\bar{R}_{vc}$. It is interesting to note that some values of α_1 and $\bar{R}_{vc}$, which led to the possibility of pulsed oscillations in the two mode case, now predict only spontaneous oscillations when four modes are included.

For a higher number of modes, the behavior is similar to the four mode case; see Fig. 5.17 for a six mode approximation and several values of $\bar{R}_{vc}$. Small values of $\bar{R}_{vc}$ produce only spontaneous oscillations, while larger values lead to small regions of possible triggering. A two parameter continuation shows that the behavioral transition occurs at a slightly higher value of $\bar{R}_{vc}$ compared with the four mode case, as illustrated in Fig. 5.18. As $\bar{R}_{vc}$ is increased above 6.53, a small region of possible triggering is created and shifts to the left.

The final term, C in Eq. (5.41), is a nonlinear pressure coupling term. For very high values of R_b, this term produced a subcritical bifurcation leading to unstable limit cycles for a linearly stable system. However, for the conditions examined so far, it did not produce the right type of coupling to nonlinear gasdynamics to produce a fold that could lead to stable limit cycles. Hence, this term does not lead to triggering. Furthermore, for reasonable values of R_b, term C had little effect on the system and can be neglected if we restrict ourselves to small perturbations.

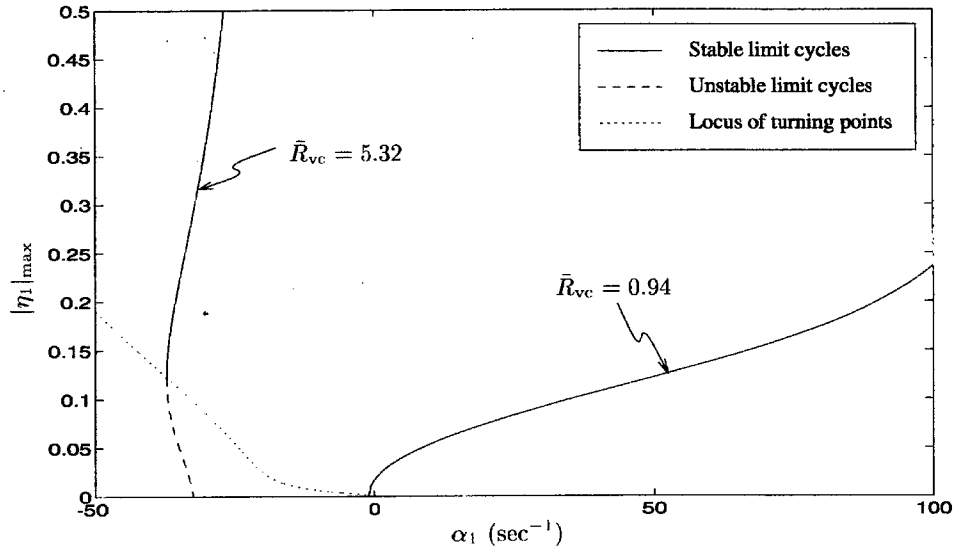

Figure 5.15 Locus of turning point bifurcations as $\bar{R}_{vc}$ is varied; time-averaged equations with term B; two modes

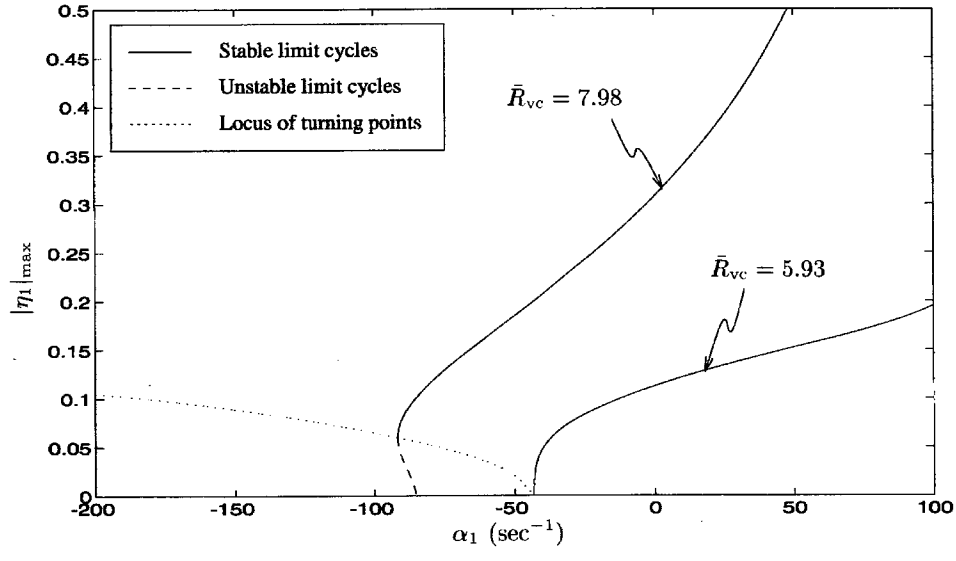

Figure 5.16 Locus of turning point bifurcations as $\bar{R}_{vc}$ is varied; time-averaged equations with term B; four modes

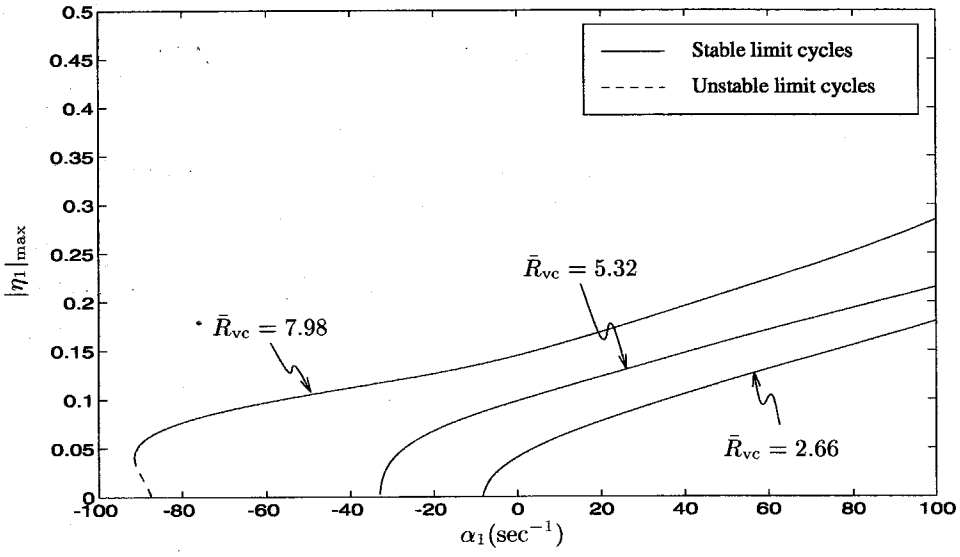

Figure 5.17 Maximum amplitude of first acoustic mode in limit cycle using term B with the time-averaged equations and various values of $\bar{R}_{vc}$; six modes

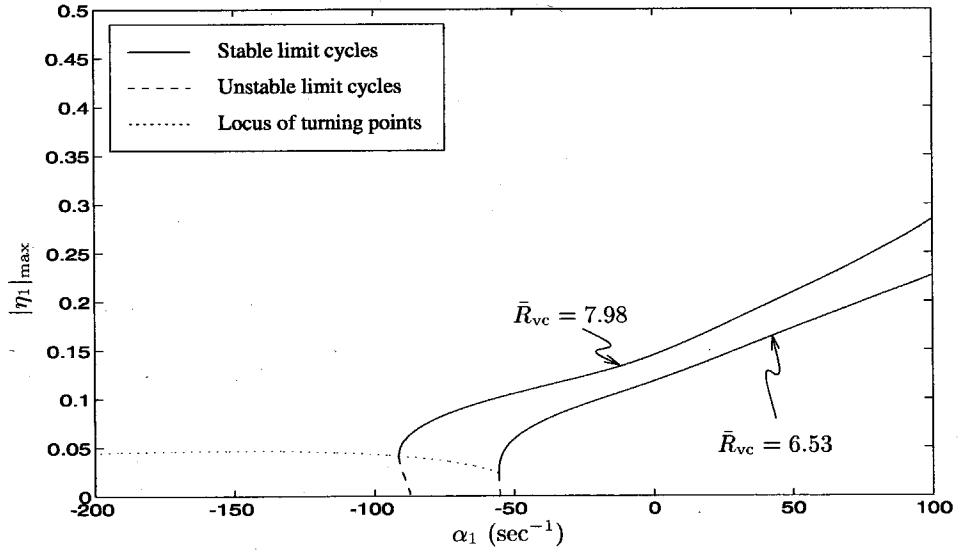

Figure 5.18 Locus of turning point bifurcations as $\bar{R}_{vc}$ is varied; time-averaged equations with term B; six modes

The Effects of Truncation

When solving Eqs. (2.46), it is necessary to truncate the system of equations to a finite number of modes. For the purposes of the approximate analysis, it is desirable to use the smallest number of modes which still provides accurate results. Many previous studies involving nonlinear gasdynamics only have used truncation to two modes, the minimum number of modes required to produce a limit cycle. Ås Jahnke and Culick [39] have shown, this approximation does not always produce good results for highly unstable systems. This approximation may become invalid for linearly stable systems as well when nonlinear combustion is also taken into account.

In the previous section, the effects of truncation were apparent in the results for the term B. This is better illustrated in Fig. 5.19 which compares results for two, four, and six mode approximations directly. Truncation to a small number of modes can thus change the qualitative behavior when only term B is used. In addition, we would like to determine the effects of truncation on the Baum and Levine model, i.e., when all terms are included.

When the Baum and Levine model is used, the system of equations appears to be more sensitive to truncation errors, as illustrated in Fig. 5.20 for $\bar{R}_{vc} = 3.75$. This is caused by the upper turning point introduced by term A. If an insufficient number of modes is included in the analysis, this turning point increases the limit cycle amplitudes. Figure 5.21 shows that for two modes, values of $\bar{R}_{vc}4.22$ no longer lead to the possibility of triggering. This is clearly a result of truncation, as comparison with the four mode case in Fig. 5.22 shows. When four modes are included, the results are good for higher ranges of $\bar{R}_{vc}$. Therefore, as the coupling to combustion processes becomes stronger, more modes must be included to obtain satisfactory results.

In general, the inclusion of a nonlinear combustion model seems to make the system more sensitive to truncation effects. Depending on the strength and

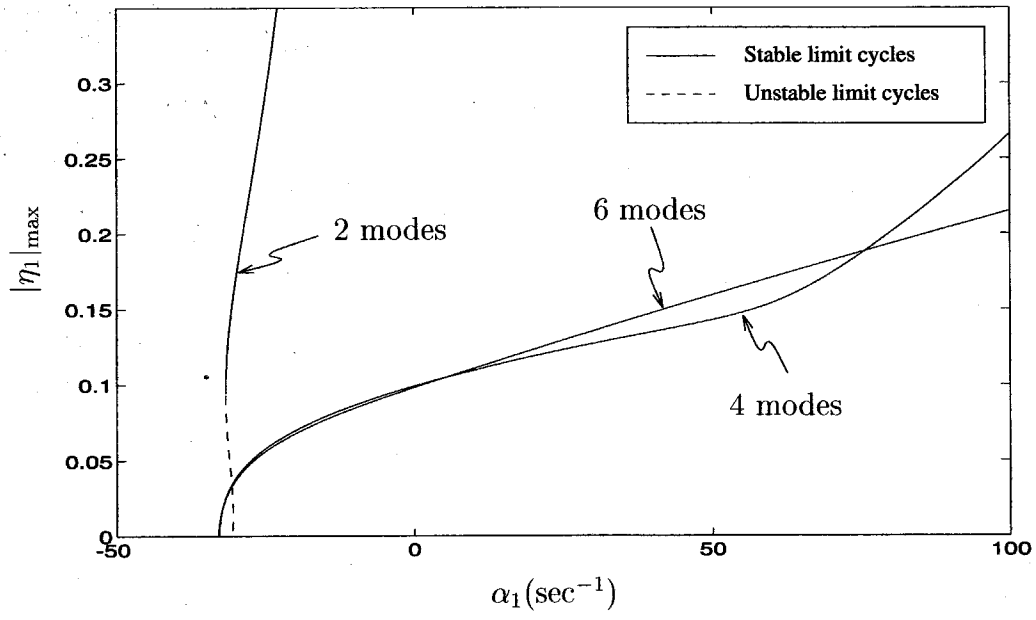

Figure 5.19 An example showing the effect of truncation to a small number of modes; time-averaged equations with Greene's nonlinear combustion model, $\bar{R}_{vc} = 5.32$

form of the nonlinear combustion model, more or less modes may be required to obtain accurate results. It does not appear that the required number of modes can be predicted in advance. Instead, this depends on the strength of the combustion response, as well as all parameters of the system.

While this section has not ruled out velocity coupling with no threshold velocity as a possible explanation for pulsed oscillations, it has shown that the models of velocity coupling adopted here produce regions of possible triggering only for very limited ranges of parameters and high values of $\bar{R}_{vc}$. In all cases treated, the region of possible triggering predicted by both the Baum and Levine model and Greene's model is extremely small if a sufficient number of modes is included. Both models are ineffective at producing large regions of possible triggering. The main influence of these models appears to be an α-shift. A system which is linearly stable without the model of velocity coupling can become unstable if the velocity coupled response function is large enough.

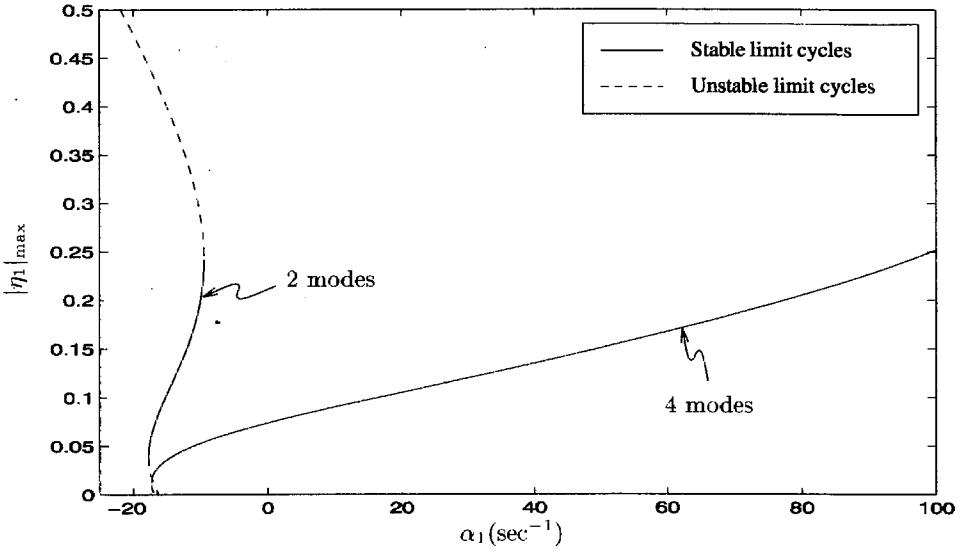

Figure 5.20 Illustration of the effect of truncation on results obtained using the Baum and Levine model; $R_b = 2.18$, $\bar{R}_{\rm vc} = 3.75$

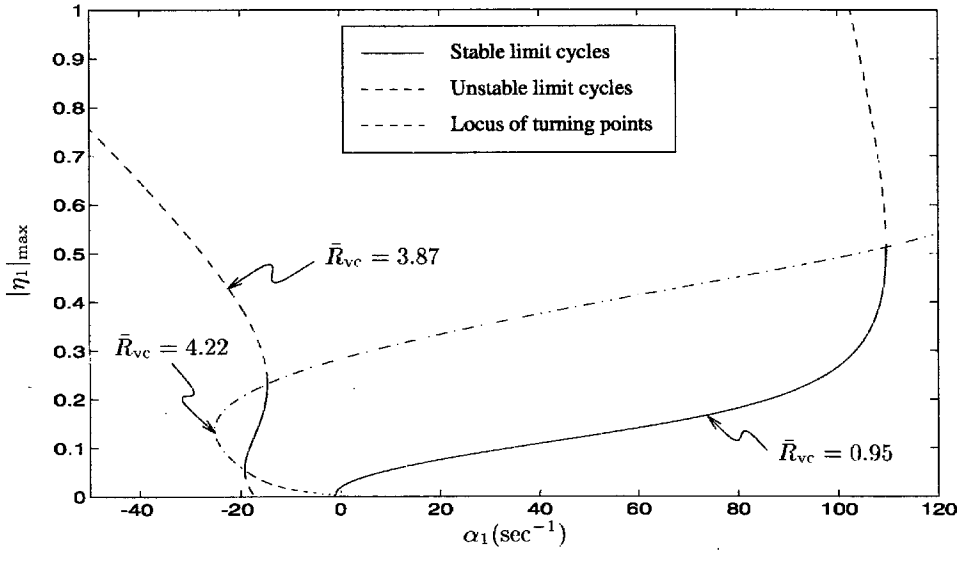

Figure 5.21 Loci of turning point bifurcations for the first acoustic mode, time-averaged equations using the Baum and Levine model; two modes, $R_b = 2.18$

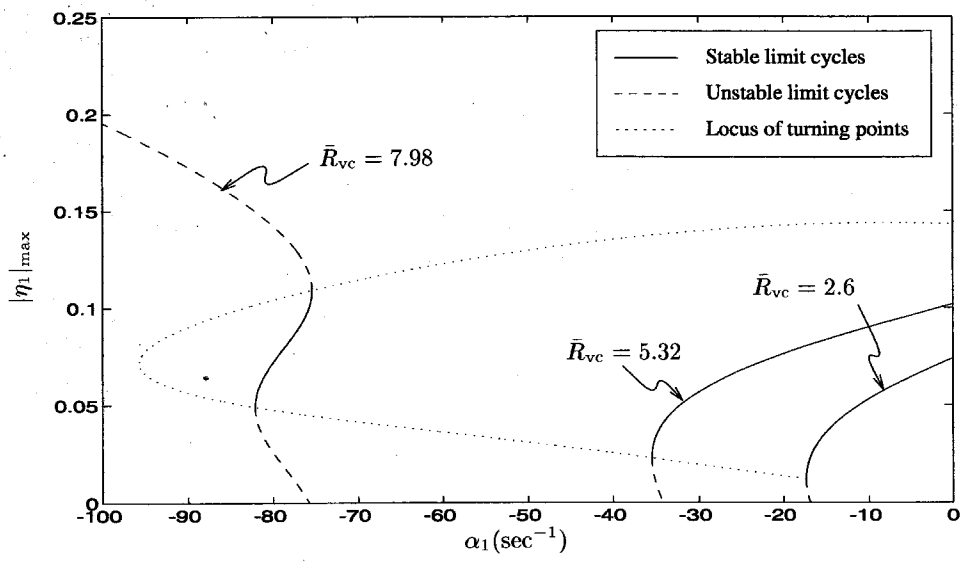

Figure 5.22 Loci of turning point bifurcations for the first acoustic mode, time-averaged equations using the Baum and Levine model; four modes, $R_b = 2.18$

This is especially true for reasonable values of R_b. Thus, we will now study the effects of a threshold velocity to determine its possible role in triggering.

5.3.3 Threshold Velocity Effects

As suggested by the earlier discrepancy between results for the time-averaged and original oscillator equations, the threshold model was developed in order to study the effects of a "true" threshold velocity. Greene's model was chosen as a base for this model because it is less sensitive to truncation to a small number of modes than the Baum and Levine model. While the second-order term A may increase the region of possible triggering slightly, it can be neglected for reasonable values of $\bar{R}_{vc}$ and R_b.

Application of the method of time-averaging does not readily allow the threshold velocity model to be used. Therefore, results will be obtained using the original oscillator equations. As explained earlier for the models of

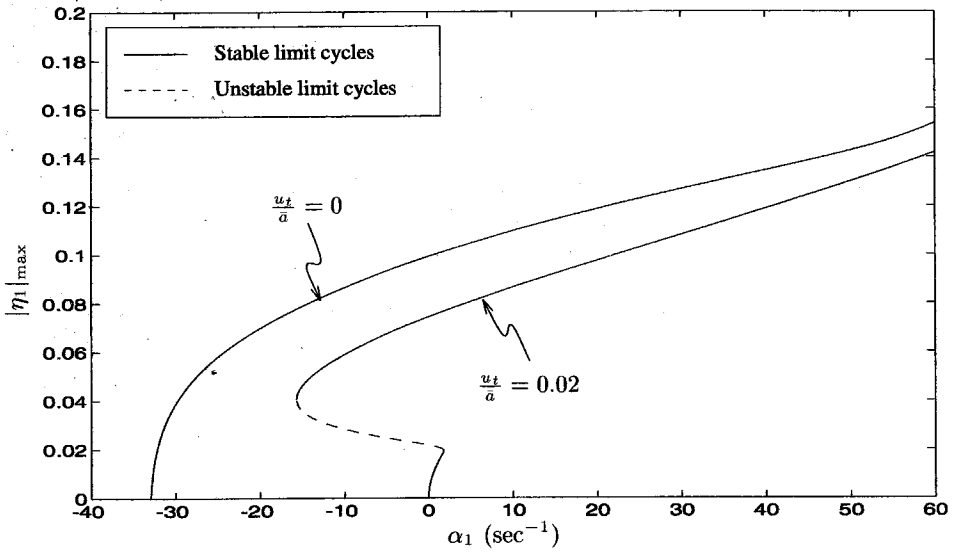

Figure 5.23 Maximum amplitude in limit cycle of first acoustic mode with and without a normalized threshold velocity of 0.02; four modes; $\bar{R}_{vc} = 5.32$

velocity coupling, the threshold velocity function shown in Fig. 5.1 must also be smoothed to be used with the continuation methods. This approximation of the threshold velocity function will affect the quantitative accuracy of the results slightly, although the qualitative behavior will be correct.

A normalized threshold velocity ($u_t/\bar{a}$) of 0.02 was chosen for initial results. This corresponds to a velocity of 21.5 m/s and is comparable to the threshold velocity used by Levine and Baum [45]. In Fig. 5.23, results for this value are compared to the case of zero threshold velocity. As expected, the threshold velocity model produces a large region of possible triggering for a reasonable value of $\bar{R}_{vc}$.

For velocity oscillations with amplitudes less than the chosen threshold velocity, the effect of nonlinear combustion is nonexistent. Therefore, the path of periodic solutions should be identical to the case of linear pressure coupling, i.e., a supercritical bifurcation occurring at the origin. This is precisely the behavior shown in Fig. 5.23. Once the magnitude of the velocity oscillations

reaches the threshold value, nonlinear combustion quickly becomes important, and a fold in the path is produced. The unstable path remains nearly horizontal until other nonlinear contributions become strong enough to produce a second fold, thereby producing a path of stable periodic solutions. Another observation from Fig. 5.23 is that the amplitudes of oscillations are lower than the amplitudes for a zero threshold velocity. This is a direct result of the dead zone introduced by the threshold velocity function.

Compared with the previous results for both the Baum and Levine model and Greene's model, the threshold velocity model produces a much larger region of possible triggering. It is thus interesting to see how this region is affected by the magnitude of the threshold velocity.

Using a two parameter continuation with u_t as the second parameter, the influence of the magnitude of the threshold velocity on the region of possible triggering will be determined by plotting the location of the lower limit of possible triggering. The turning point on the left-hand side of Fig. 5.23 represents the lower limit, while the upper limit is simply $\alpha_1 = 0$ sec^{-1} since the system must be linearly stable for triggering to occur.

The result of the two parameter continuation for $\bar{R}_{\text{vc}} = 5.32$ is provided in Fig. 5.24.* There is actually no triggering for $u_t/\bar{a} = 0$, although a large region of possible triggering exists for $u_t/\bar{a}$ infinitesimally greater than zero. As u_t is increased, the region becomes increasingly smaller until finally, a critical value is reached above which triggering is no longer possible. This phenomenon was noted by Levine and Baum [45], but no possible explanations were given.

An example of a case in which the threshold velocity is greater than u_t^{crit} is given in Fig. 5.25. For such a high threshold velocity, the rate of energy production by nonlinear combustion cannot equal the rate at which energy is

*Note that there is a discrepancy between Figs. 5.23 and 5.24 for $u_t = 0$. This is due to the quantitative inaccuracy of the original oscillator equations when using the threshold velocity model in the continuation method. The plot of $u_t = 0$ in Fig. 5.23 was generated using the time-averaged equations which are more accurate in this case.

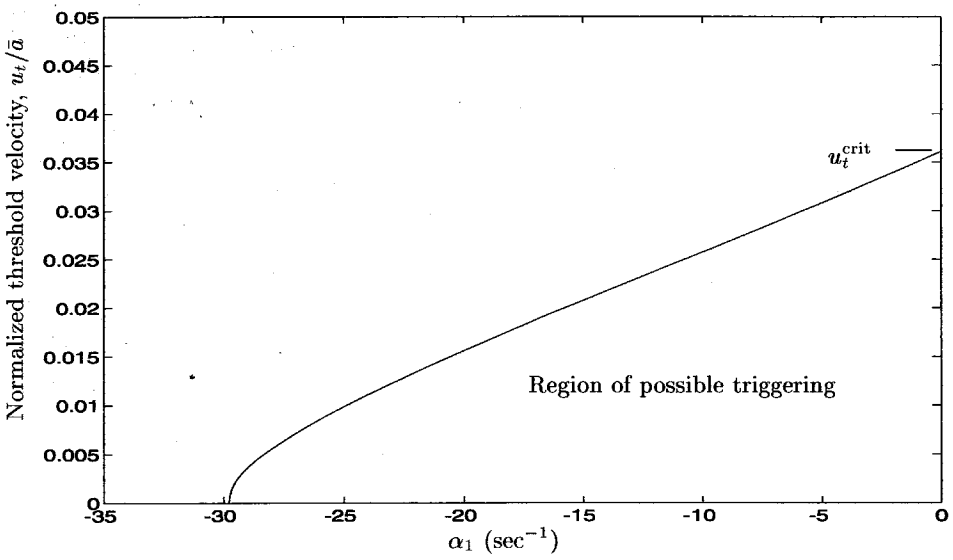

Figure 5.24 Influence of the threshold velocity u_t on the region of possible triggering; $\bar{R}_{\text{vc}} = 5.32$

transferred to higher modes by nonlinear gasdynamics. Therefore, for a stable limit cycle to exist, additional energy must be provided by linear processes, i.e., $\alpha_1 > 0$. For this reason, a propellant with a very high threshold velocity will be impossible to trigger. The critical value of u_t depends directly on the value of the velocity coupled response function, as one would expect. The rate of energy production is proportional to $\bar{R}_{\text{vc}}$. As the coupling to velocity oscillations becomes stronger, i.e., $\bar{R}_{\text{vc}}$ increases, u_t^{crit} increases accordingly, as demonstrated in Fig. 5.26.

Although no region of possible triggering exists when u_t^{crit} is exceeded, it is possible that more than one stable limit cycle may exist for the same value of α_1, as Fig. 5.25 demonstrates. When this is the case, the limiting amplitude that is reached depends on the initial conditions. Previous results for nonlinear contributions from gasdynamics only proved that when a limit cycle exists, it is unique. It appears that this may not be true when nonlinear combustion is also included in the analysis.

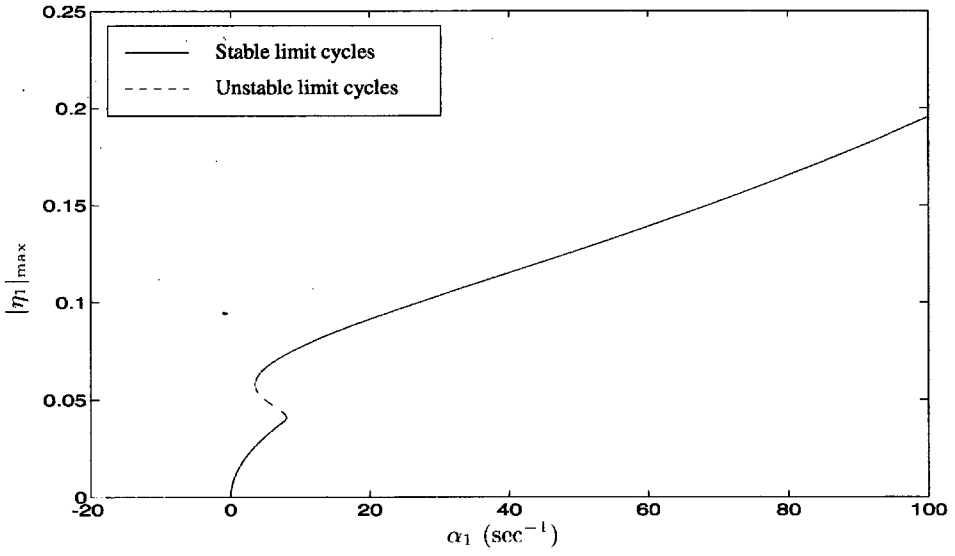

Figure 5.25 An example of a bifurcation diagram for a threshold velocity greater than u_t^{crit}; $\bar{R}_{\text{vc}} = 5.32$, $u_t/\bar{a} = 0.04$

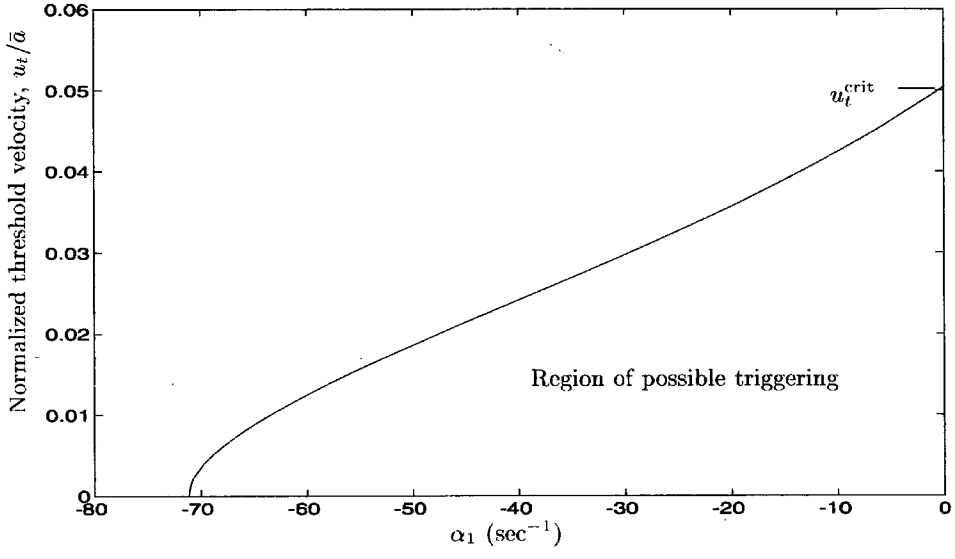

Figure 5.26 Influence of the threshold velocity u_t on the region of possible triggering; $\bar{R}_{\text{vc}} = 7.8$

An Example Demonstrating the Effects of Pulse Shape and Location

When only nonlinear contributions from gasdynamics are taken into account, there is at most one stationary state. The limiting solution is therefore independent of the initial pulse shape [3, 55]. When nonlinear combustion is also included, more than one stationary state may exist and the pulse shape is therefore important.

To illustrate this point, we will perform simulations using several different rectangular pressure pulses which are initially at rest. The first pulse is nonzero only in the range $0 \leq x \leq .25L$ where it has a magnitude of 0.1. The two and ten mode approximations to this wave are shown in Fig. 5.27. Although two modes do not provide a good approximation to the intended waveform, the simulations will show that the final results are the same as the ten mode case.

For the two mode approximation to the rectangular pulse, the initial conditions are $\eta_1(0) = 0.045$, $\eta_2(0) = 0.032$, $\dot{\eta}_1(0) = 0$, and $\dot{\eta}_2(0) = 0$ [14]. The linear growth rate was chosen to be -20 sec^{-1}, and the initial conditions are plotted on the bifurcation diagrams shown in Fig. 5.28. The initial conditions for both η_1 and η_2 are in the regions of attraction of the stable limit cycle, i.e., the magnitudes are larger than the magnitudes of the branches of the unstable limit cycles. However, the initial conditions for $\dot{\eta}_1$ and $\dot{\eta}_2$ are in the regions of attraction of the trivial steady state, so it is difficult to say whether the final solution will be the trivial steady state or the periodic limit cycle. As shown in Fig. 5.29, the system is drawn to the periodic limit cycle, and the pulse is said to be "unstable." The ten mode approximation produced the same behavior although the amplitudes are smaller due to truncation effects; see Fig. 5.30.

An interesting result is obtained if we increase the width of the pulse to 75% of the chamber length so that the pressure perturbation is nonzero in the range $0 \leq x \leq .75L$. For the two mode case, the initial conditions are $\eta_1(0) = 0.045$, $\eta_2(0) = -0.032$, $\dot{\eta}_1(0) = 0$, and $\dot{\eta}_2(0) = 0$. These initial

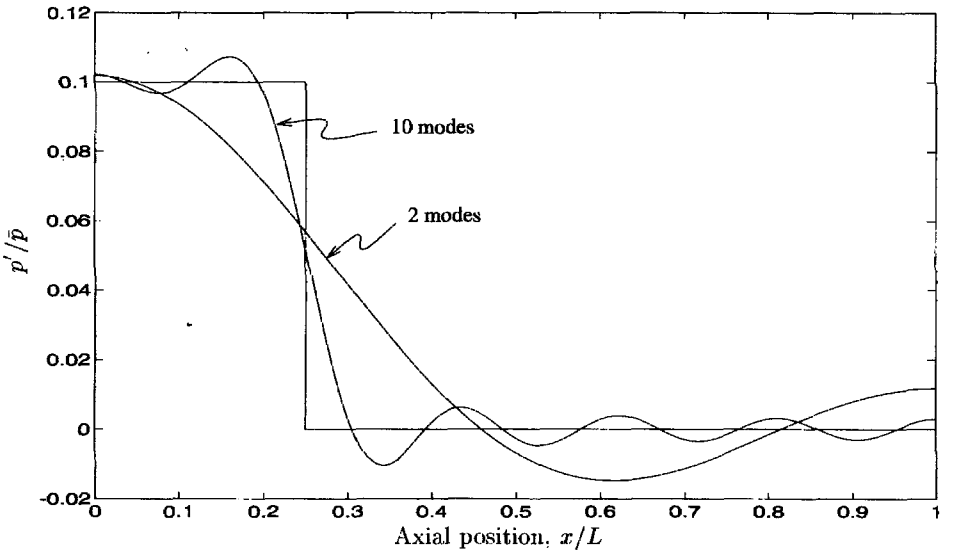

Figure 5.27 Two and ten mode approximations to a rectangular initial pulse in the range $0 \leq x \leq .25L$

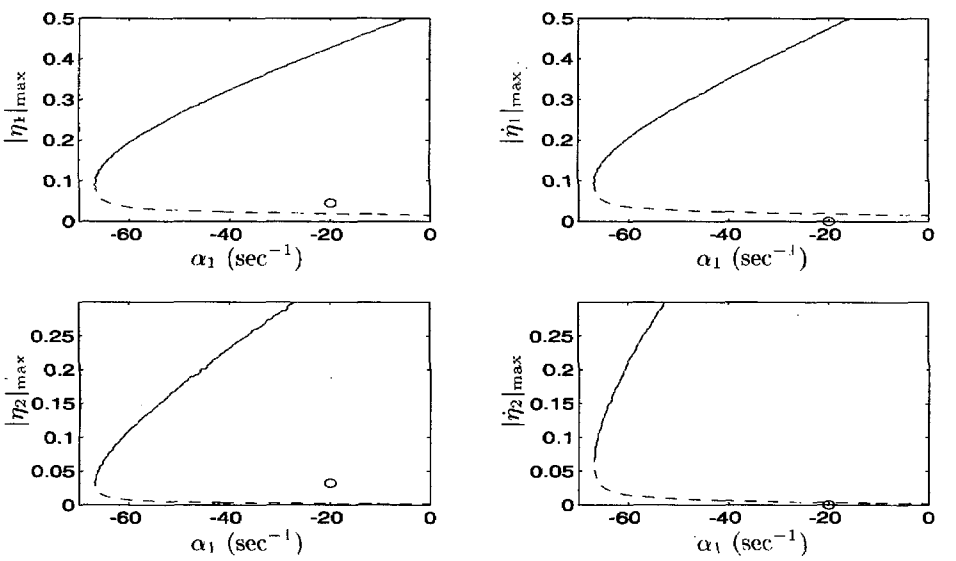

Figure 5.28 Bifurcation diagrams for all dependent variables; two modes, threshold velocity model, $\bar{R}_{vc} = 7.98$, $u_t/\bar{a} = 0.015$

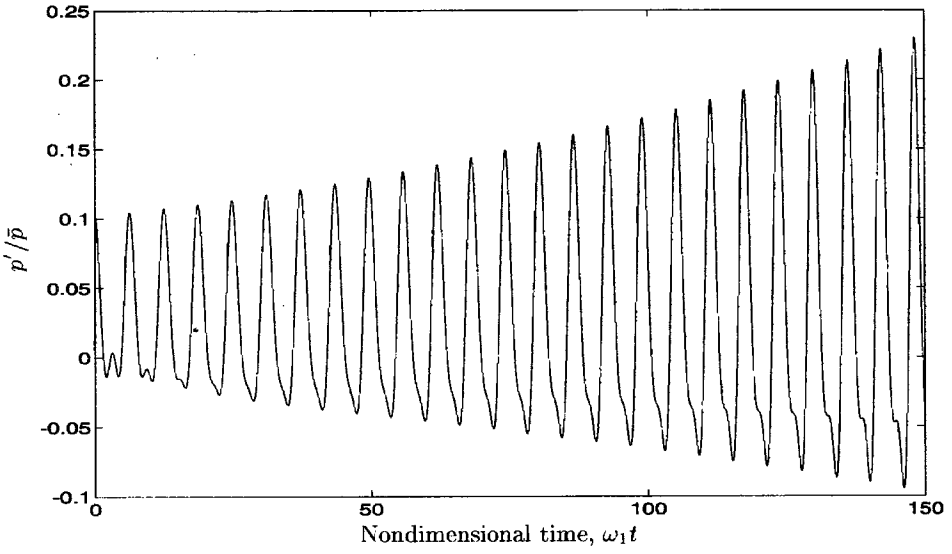

Figure 5.29 Time history of the pressure at the head end after a rectangular initial pulse in the range $0 \leq x \leq .25L$; two modes, $\alpha_1 = -20$ sec^{-1}

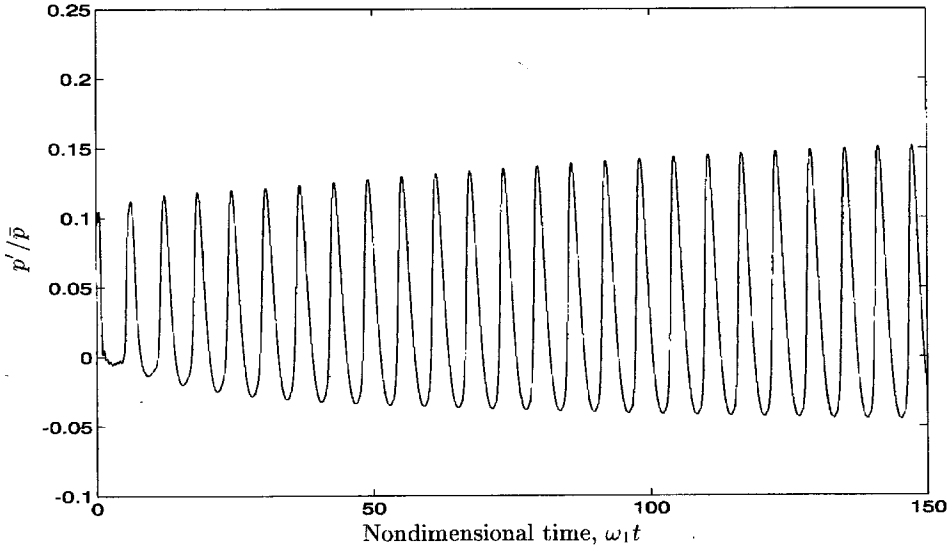

Figure 5.30 Time history of the pressure at the head end after a rectangular initial pulse in the range $0 \leq x \leq .25L$; ten modes, $\alpha_1 = -20$ sec^{-1}

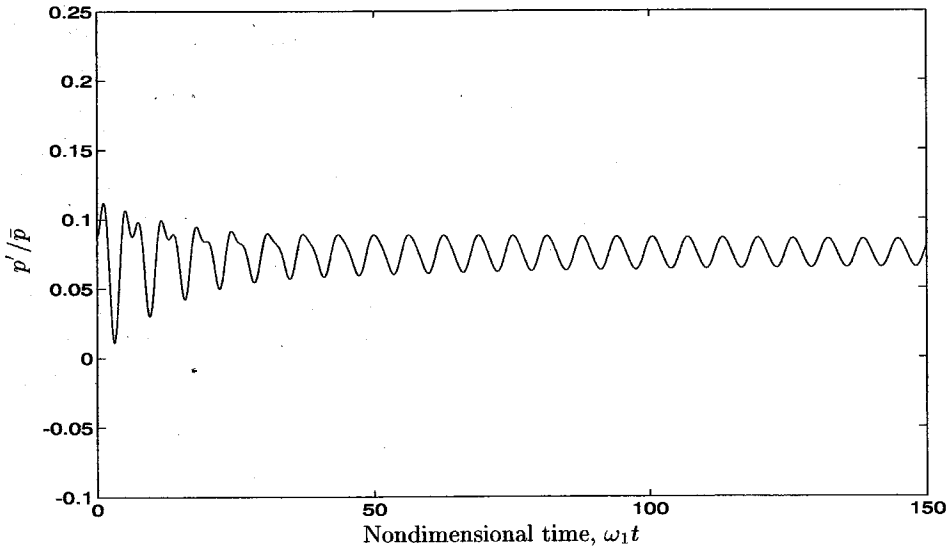

Figure 5.31 Time history of the pressure at the head end after a rectangular initial pulse in the range $0 \leq x \leq .75L$; two modes, $\alpha_1 = -20$ sec^{-1}

conditions are the same as the previous pulse with the exception of η_2, which has changed sign. In the bifurcation diagrams, the initial conditions are located at the same points. Nonetheless, the perturbations decay over time, and the pulse is stable. Simulations of the two and ten mode approximations are shown in Figs. 5.31 and 5.32, respectively.

It is apparent that the size of a pulse can affect the behavior of a system. In addition, the location of the pulse is also important. To demonstrate this observation, a rectangular pulse with a width of $.25L$ will be introduced at two different locations in the chamber. The first location is in the range $0 \leq x \leq .25L$, i.e., the same location as the first pulse. As already shown, the pulse is unstable, and a periodic solution is attained. The spatial and temporal variations of pressure and velocity for a ten mode simulation are shown in Figs. 5.33 and 5.34. If the pulse is placed sufficiently far from a wall, the pulse is found to be stable. The pressure and velocity oscillations produced a pulse in the range $.40L \leq x \leq .65L$ are presented in Figs. 5.35

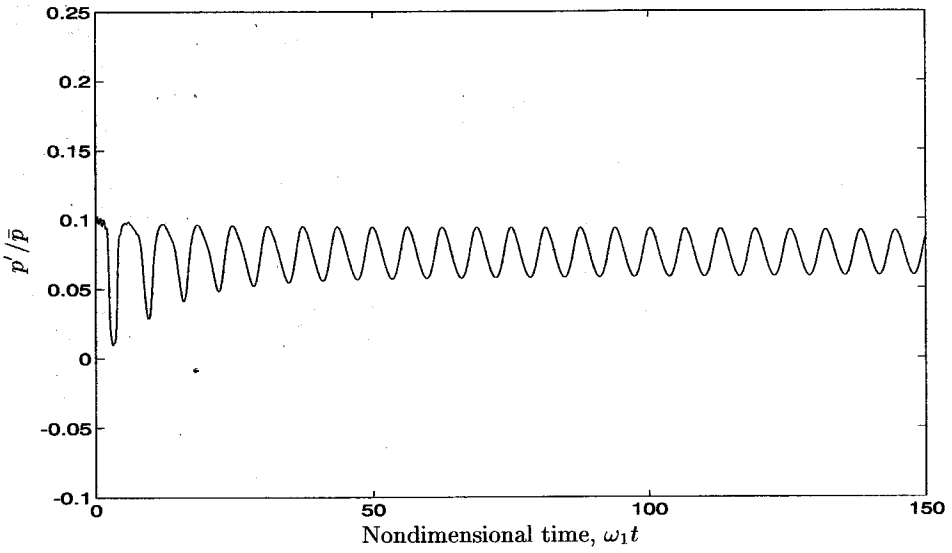

Figure 5.32 Time history of the pressure at the head end after a rectangular initial pulse in the range $0 \leq x \leq .75L$; ten modes, $\alpha_1 = -20$ sec^{-1}

and 5.36. It was determined that if the pulse was closer to a wall than $\sim .12L$, the resulting motions would be unstable. This result only applies to a pulse with a width of $.25L$ and a magnitude of 0.1.

To understand the reason for the different results, we need to look closely at the waves produced by the initial pulse. For $t > 0$, a pulse which is initially at rest splits into two waves moving in opposite directions. When a wave encounters a solid boundary, the wave is reflected and continues in the opposite direction. The wave shapes and amplitudes are affected by all linear and nonlinear processes in the system until a stationary state is reached.

The pulse located at the head end of the chamber is a special case. One of the waves is immediately reflected, and a large wave is produced instead of two distinct waves. This is shown in Fig. 5.37. Comparison of this wave pattern with the pressure distribution in the limit cycle (Fig. 5.38) shows that the basic wave structure is the same. Very little energy is thus required to change the wave from its initial shape to the final shape in the limit cycle.

The second pulse is introduced in the interior of the chamber, and two distinct waves are produced. The initial wave pattern for this pulse is much different than the waves in the limit cycle, as displayed in Fig. 5.39. The dynamics of the system attempt to change the shape of this wave to that of the limit cycle wave. However, as energy is extracted from the system, the velocity fluctuations decrease below the threshold value. Without this additional source of energy, the oscillations cannot be sustained, and the pulse is stable.

5.4 Concluding Remarks

In the current chapter, several models of nonlinear combustion response have been used to study the effects of nonlinear contributions from combustion processes. The first model, which represents coupling of combustion processes to pressure oscillations, model, was produced by extending the derivation of a linear response function to include terms to second-order. For parametric values corresponding to realistic propellants, this model did not produce the possibility of triggering.

The next two models were used in previous investigations by Kim [42] and Greene [32] and represent coupling of combustion processes to velocity oscillations. Both of these studies, however, did not develop the system of equations consistently and terms which should be included were left out. We have corrected the inconsistencies, and the resulting equations were used to study the effects of velocity coupling on combustion instabilities.

The investigations by Kim and Greene concluded that velocity coupling can produce substantial regions of possible triggering. Unfortunately, both of those studies used the approximation of truncation to two modes without regard to the possible consequences. In the present chapter, the effects of truncation

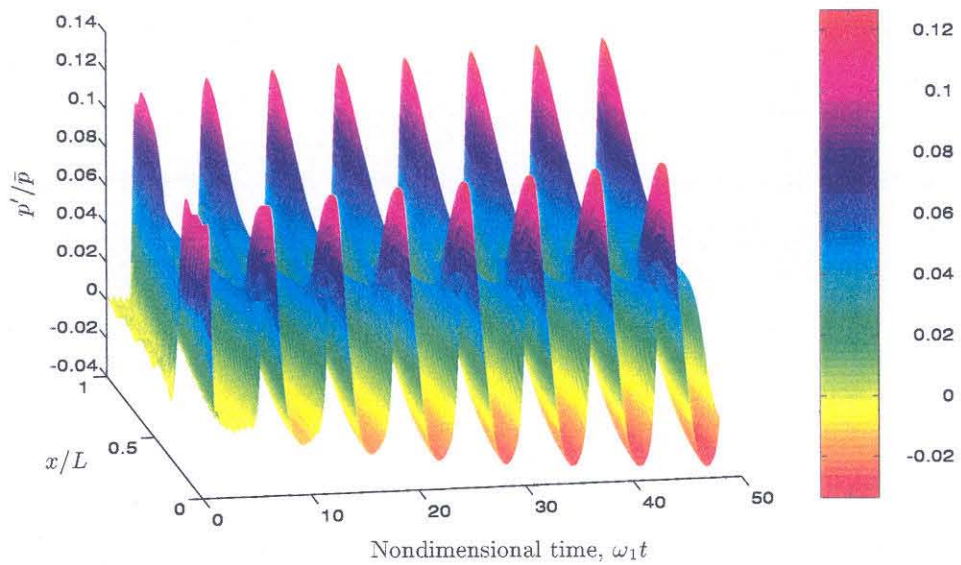

Figure 5.33 Spatial and temporal variation of pressure after a rectangular initial pulse in the range $0 \leq x \leq .25L$; ten modes, $\alpha_1 = -20 \text{ sec}^{-1}$

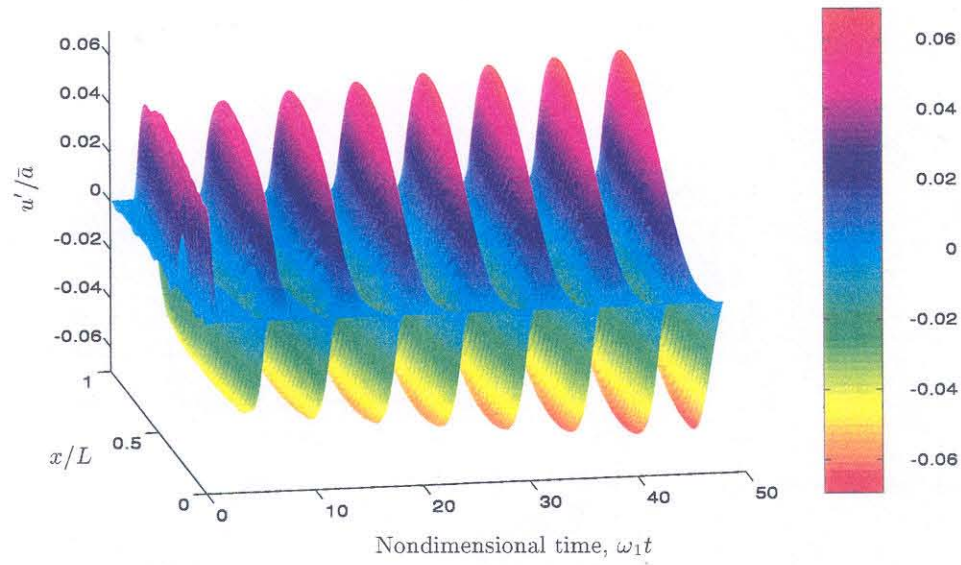

Figure 5.34 Spatial and temporal variation of velocity after a rectangular initial pulse in the range $0 \leq x \leq .25L$; ten modes, $\alpha_1 = -20 \text{ sec}^{-1}$

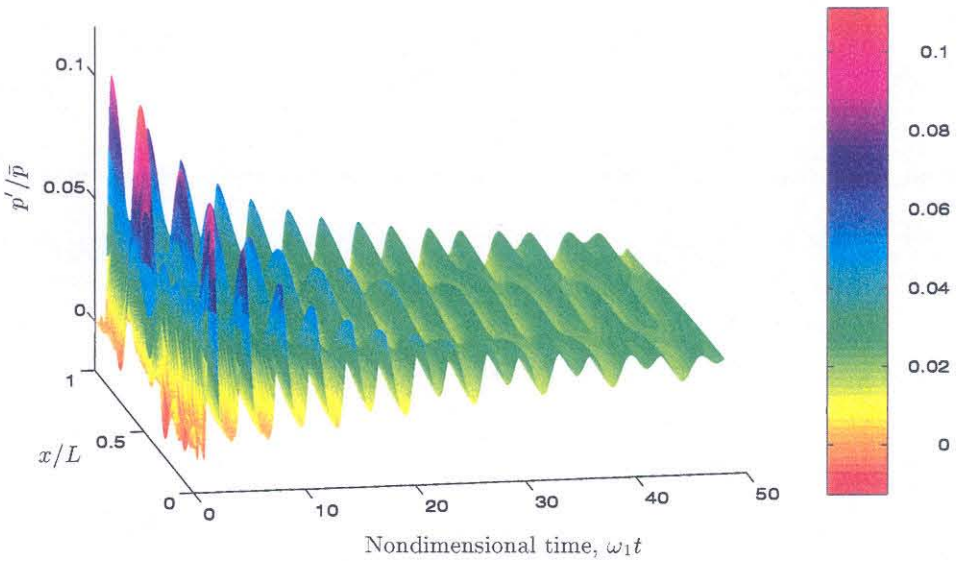

Figure 5.35 Spatial and temporal variation of pressure after a rectangular initial pulse in the range $.40L \leq x \leq .65L$; ten modes, $\alpha_1 = -20$ sec^{-1}

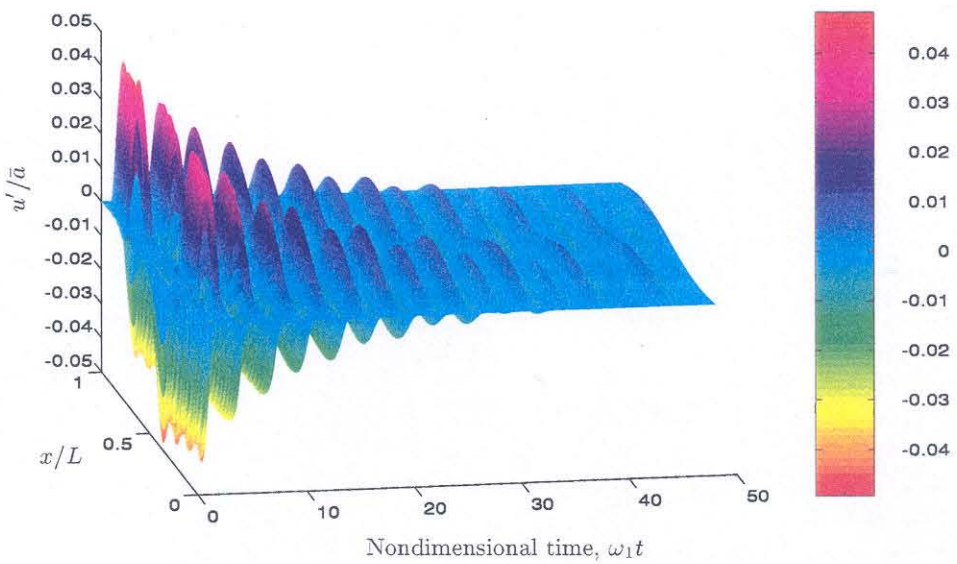

Figure 5.36 Spatial and temporal variation of velocity after a rectangular initial pulse in the range $.40L \leq x \leq .65L$; ten modes, $\alpha_1 = -20$ sec^{-1}

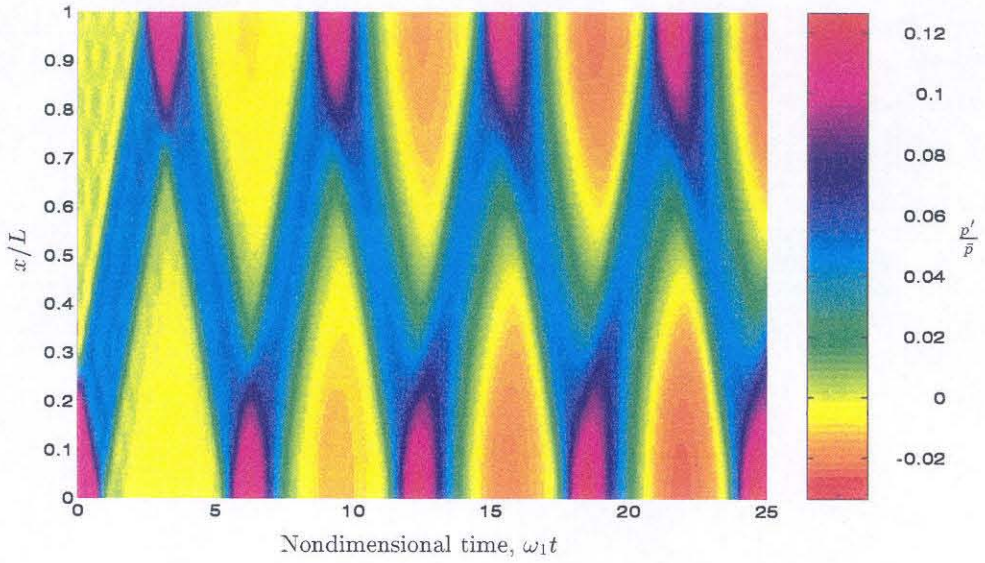

Figure 5.37 Detail of pressure waves after a rectangular initial pulse in the range $0 \leq x \leq .25L$; ten modes, $\alpha_1 = -20$ sec^{-1}

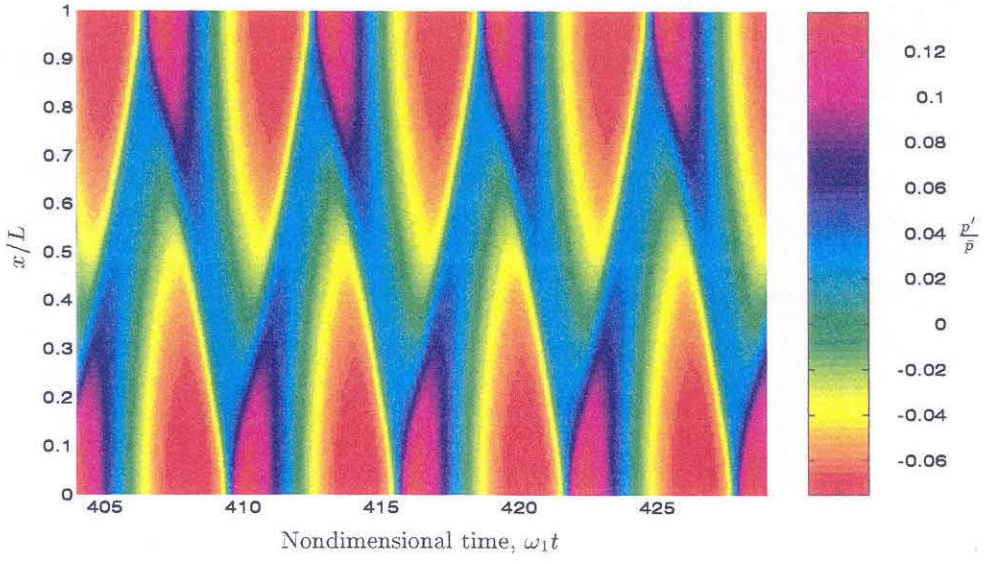

Figure 5.38 Pressure waves once the limit cycle has been reached; ten modes, $\alpha_1 = -20$ sec^{-1}

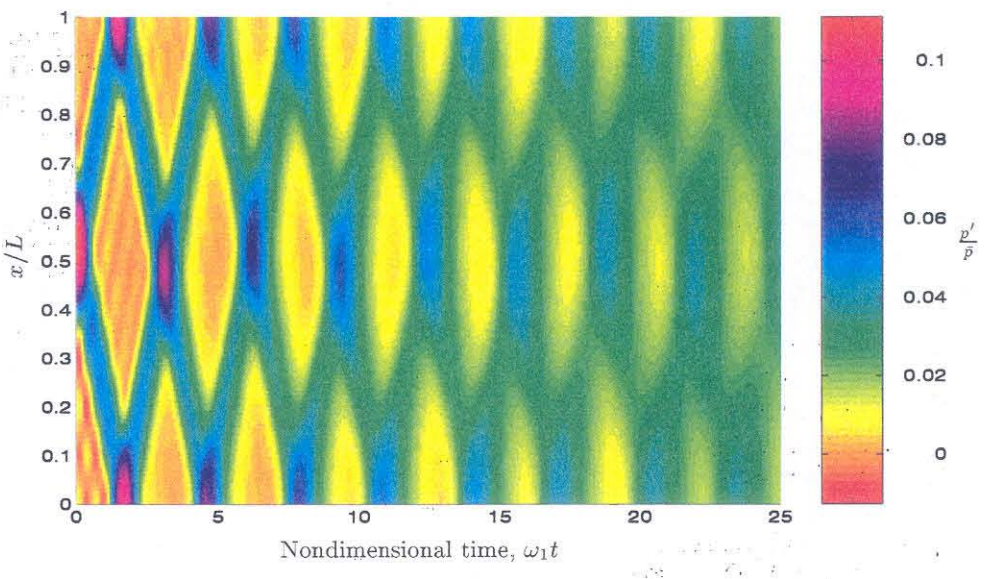

Figure 5.39 Detail of pressure waves after a rectangular initial pulse in the range $.40L \leq x \leq .65L$; ten modes, $\alpha_1 = -20$ sec^{-1}

to a small number of modes were also studied. Although the present results for two modes are consistent with the findings of Kim and Greene, the region of possible triggering is either greatly reduced or eliminated altogether when more than two modes are included. When the possibility of triggering still exists, it is only for very restrictive values of the parameters.

As the previous three models did not produce substantial regions of possible triggering, a final model was introduced to study the effects of a threshold velocity. This phenomenon has been observed experimentally and may be important in pulsed instabilities. When a threshold velocity is taken into account, a large region of possible triggering may be found. The size of the region depends on the magnitude of the threshold and the strength of the coupling between combustion and velocity oscillations. Finally, an example was presented which shows the effects of pulse shape on the behavior of the system when more than one stationary solution is present.

Chapter 6

The Influence of Combustion Noise

Combustion chambers are inherently noisy environments. This is apparent from listening and from inspection of the power spectra of pressure records from test firings. When a combustion instability is present, the power spectrum exhibits well-defined peaks in addition to background noise over the entire range of frequencies. Substantial noise sources in rocket motors include flow separation, turbulence, and combustion processes. It is expected that the presence of noise will affect in some way the amplitudes and possibly the qualitative behavior of organized oscillations. That is precisely the purpose of this chapter: to determine the influence of noise on combustion instabilities.

Only a small amount of work has been done on the interactions between noise and acoustic instabilities. Culick et al. [20] studied the influence of noise on combustion instabilities, but only for a very simple case: two acoustic modes with noise present only in the first mode. In addition, the formulation was flawed, and the form of the resulting noise terms is not quite correct. Clavin et al. [8] studied the influence of turbulence on instabilities in liquid rocket motors. Using only one mode in the analysis and third-order nonlinearities, it was reported that the inclusion of noise can lead to the possibility of triggering. It is a well-known result that a single third-order equation may produce a subcritical bifurcation. When more acoustic modes are considered,

this may not be the case, as demonstrated by Yang et al. [56] for third-order gasdynamics. Therefore, the results of Clavin et al. may not be applicable in general.

The present analysis is an extension of the previous work by Culick et al. [20]. We will first decompose the flow field into acoustic and non-acoustic parts using a method developed by Chu and Kovásznay [6]. This will allow the general form of the noise terms to be developed. Finally, we will simplify the equations in order to study the possible influences of noise on combustion instabilities.

6.1 Splitting the Unsteady Flow Field Into Acoustic, Vortical, and Entropic Modes of Propagation

Fluctuations in a compressible fluid can be decomposed into three types of waves: acoustic waves, vorticity waves, and entropy waves. A thorough discussion of this idea is presented by Chu and Kovásznay [6]. The three waves propagate independently in linearized theory of a uniform mean flow, but are coupled when the mean flow is non-uniform [18]. For example, the pressure in an acoustic wave is changed slightly by the presence of a vorticity or entropy wave if the mean flow is not uniform. Coupling between modes may also occur at the boundaries of the chamber.

Although noise is detected as pressure waves, the *sources* of noise are associated with the presence of vorticity fluctuations (e.g., turbulence, flow separation, etc.) and entropy or non-isentropic temperature fluctuations. Therefore, decomposing the unsteady flow field into the three types of waves allows both noise and acoustic instabilities to be handled in the same analytical frame-

work that was developed in Chapter 2. The contributions from vorticity and entropy waves will appear as additional force terms on the right-hand side of the acoustic equation.

Following the analysis of Chu and Kovásznay [6], the thermodynamic and kinematic variables can be written as a sum of fluctuations in the three waves as follows.

$$p' = p'_a + p'_\Omega + p'_s \tag{6.1}$$

$$\boldsymbol{\Omega}' = \boldsymbol{\Omega}'_a + \boldsymbol{\Omega}'_\Omega + \boldsymbol{\Omega}'_s \tag{6.2}$$

$$s' = s'_a + s'_\Omega + s'_s \tag{6.3}$$

$$\boldsymbol{u}' = \boldsymbol{u}'_a + \boldsymbol{u}'_\Omega + \boldsymbol{u}'_s \tag{6.4}$$

In general, all of the fluctuations will be nonzero, but not all terms are the same order. If we restrict the analysis to small amplitude motions, the three waves have the following characteristics [6]:

$(\ )_a$ acoustic waves: pressure and velocity fluctuations, no entropy change

$(\ )_\Omega$ vorticity waves: velocity fluctuations, no pressure or entropy changes

$(\ )_s$ entropy waves: entropy and velocity fluctuations, no pressure change

Thus, to zeroth-order, the fluctuations in the three waves are given by

$$p' = p'_a, \tag{6.5}$$

$$\boldsymbol{\Omega}' = \boldsymbol{\Omega}'_\Omega, \tag{6.6}$$

$$s' = s'_s, \tag{6.7}$$

$$\boldsymbol{u}' = \boldsymbol{u}'_a + \boldsymbol{u}'_\Omega + \boldsymbol{u}'_s. \tag{6.8}$$

An equation for the density fluctuation is obtained by expanding the formula for the entropy of a perfect gas.

$$\frac{\rho'}{\bar{\rho}} = \frac{1}{\bar{\gamma}}\frac{p'_a}{\bar{p}} - \frac{1}{\bar{c}_p}s' \tag{6.9}$$

The acoustic pressure and velocity can be expanded as a superposition of the classical acoustic modes so that

$$p'_a = \bar{p}\sum_{m=1}^{\infty}\eta_m(t)\psi_m(\boldsymbol{r}), \tag{6.10}$$

$$\boldsymbol{u}'_a = \sum_{m=1}^{\infty}\frac{\dot{\eta}_m(t)}{\bar{\gamma}k_m^2}\nabla\psi_m(\boldsymbol{r}). \tag{6.11}$$

Substitution of Eq. (6.5) in the left-hand side of the nonlinear wave equation (2.32), followed by application of Galerkin's method, leads to a set of coupled nonlinear oscillator equations.

$$\ddot{\eta}_n + \omega_n^2\eta_n = F_n \tag{6.12}$$

The right-hand side will be slightly different from the previous derivation since the isentropic relation between p' and ρ' was not used. The general form of the forcing function F_n, including gasdynamics to second-order, is [18]

$$-\frac{\bar{p}E_n^2}{\bar{a}^2}F_n = \bar{\rho}I_1 + \frac{1}{\bar{a}^2}I_2 + \bar{\rho}I_3 + \frac{1}{\bar{a}^2}I_4 + \int\bar{\rho}\frac{\partial\boldsymbol{u}'}{\partial t}\cdot\hat{\boldsymbol{n}}dS - \int\left[\frac{1}{\bar{a}^2}\frac{\partial\mathcal{P}'}{\partial t}\psi_n + \boldsymbol{\mathcal{F}}'\cdot\nabla\psi_n\right]dV, \tag{6.13}$$

where

$$I_1 = \int (\bar{\boldsymbol{u}} \cdot \nabla \boldsymbol{u}' + \boldsymbol{u}' \cdot \nabla \bar{\boldsymbol{u}}) \cdot \nabla \psi_n dV, \tag{6.14a}$$

$$I_2 = \frac{\partial}{\partial t} \int (\bar{\gamma} p' \nabla \cdot \bar{\boldsymbol{u}} + \bar{\boldsymbol{u}} \nabla \cdot p') \psi_n dV, \tag{6.14b}$$

$$I_3 = \int \left(\boldsymbol{u}' \cdot \nabla \boldsymbol{u}' + \frac{\rho'}{\bar{\rho}} \frac{\partial \boldsymbol{u}'}{\partial t} \right) \cdot \nabla \psi_n dV, \tag{6.14c}$$

$$I_4 = \frac{\partial}{\partial t} \int (\bar{\gamma} p' \nabla \cdot \boldsymbol{u}' + \boldsymbol{u}' \cdot \nabla p') \psi_n dV. \tag{6.14d}$$

Recall that the zeroth-order approximations for pressure and velocity were used to evaluate F_n in the development of the approximate analysis. The same idea will be applied here, although there are additional contributions to the velocity fluctuation from coupling to vorticity and entropy waves which will be included. We will now substitute Eqs. (6.5), (6.8), and (6.9) to determine the form of the additional forcing terms.

The first integral I_1 is linear in the velocity fluctuation and therefore gives rise to three integrals, one associated with each of the waves. Some simplification is gained by using a vector identity to rewrite the integrand of I_1 as

$$\bar{\boldsymbol{u}} \cdot \nabla \boldsymbol{u}' + \boldsymbol{u}' \cdot \nabla \bar{\boldsymbol{u}} = \nabla (\bar{\boldsymbol{u}} \cdot \boldsymbol{u}') - (\bar{\boldsymbol{u}} \times \nabla \times \boldsymbol{u}' + \boldsymbol{u}' \times \nabla \times \bar{\boldsymbol{u}}). \tag{6.15}$$

Then after substitution for $\boldsymbol{u}'$, I_1 can be written as

$$I_1 = I_1^a + I_1^\Omega + I_1^s, \tag{6.16}$$

with

$$I_1^a = \int [\nabla(\bar{\boldsymbol{u}} \cdot \boldsymbol{u}_a') - \boldsymbol{u}_a' \times \nabla \times \bar{\boldsymbol{u}}] \cdot \nabla \psi_n dV, \tag{6.17}$$

$$I_1^\Omega = \int [\nabla(\bar{\boldsymbol{u}} \cdot \boldsymbol{u}_\Omega') - \boldsymbol{u}_\Omega' \times \nabla \times \bar{\boldsymbol{u}} - \bar{\boldsymbol{u}} \times \boldsymbol{\Omega}'] \cdot \nabla \psi_n dV, \tag{6.18}$$

$$I_1^s = \int [\nabla(\bar{\boldsymbol{u}} \cdot \boldsymbol{u}_s') - \boldsymbol{u}_s' \times \nabla \times \bar{\boldsymbol{u}} - \bar{\boldsymbol{u}} \times \nabla \times \boldsymbol{u}_s'] \cdot \nabla \psi_n dV. \tag{6.19}$$

The integral I_2 is linear in the pressure fluctuation and hence produces only one integral.

$$I_2 = I_2^a = \frac{\partial}{\partial t} \int [\bar{\gamma} p_a' \nabla \cdot \bar{\boldsymbol{u}} + \bar{\boldsymbol{u}} \cdot \nabla p_a'] \, \psi_n dV \tag{6.20}$$

The integrals I_1^a and I_2^a are the gasdynamical contributions to the linear stability problem. For the same reasons given in Section 2.4, the linear coupling resulting from gasdynamics will be ignored. Therefore, we obtain the familiar result

$$-\frac{\bar{a}^2}{\bar{p} E_n^2} \left\{ \bar{\rho} I_1^a + \frac{1}{\bar{a}^2} I_2^a \right\} = 2\alpha_n \dot{\eta}_n + 2\omega_n \theta_n \eta_n. \tag{6.21}$$

On the other hand, the integrals I_1^Ω and I_1^s contain $\boldsymbol{u}_\Omega'$ and $\boldsymbol{u}_s'$ which act as source terms for the 'noise' part of the acoustic field. They are independent of the acoustic field and schematically can be written in Eq. (6.13) as

$$-\frac{\bar{a}^2}{\bar{p} E_n^2} \left\{ \bar{\rho} (I_1^\Omega + I_1^s) \right\} = \Xi_n^{(1)}(t). \tag{6.22}$$

The last two integrals are second-order in fluctuations and, as such, produce

up to nine distinct integrals each. After substitution for $\boldsymbol{u}'$, I_3 becomes

$$\begin{aligned} I_3 =& I_3^{aa} + I_3^{a\Omega} + I_3^{as} \\ &+ I_3^{\Omega a} + I_3^{\Omega\Omega} + I_3^{\Omega s} \\ &+ I_3^{sa} + I_3^{s\Omega} + I_3^{ss}, \end{aligned} \tag{6.23}$$

where

$$I_3^{aa} = \int \left[\boldsymbol{u}'_a \cdot \nabla \boldsymbol{u}'_a + \frac{\rho'_a}{\bar{\rho}} \frac{\partial \boldsymbol{u}'_a}{\partial t} \right] \cdot \nabla \psi_n dV, \qquad I_3^{a\Omega} = \int [\boldsymbol{u}'_a \cdot \nabla \boldsymbol{u}'_\Omega] \cdot \nabla \psi_n dV,$$

$$I_3^{as} = \int \left[\boldsymbol{u}'_a \cdot \nabla \boldsymbol{u}'_s + \frac{\rho'_a}{\bar{\rho}} \frac{\partial \boldsymbol{u}'_s}{\partial t} \right] \cdot \nabla \psi_n dV, \qquad I_3^{\Omega a} = \int [\boldsymbol{u}'_\Omega \cdot \nabla \boldsymbol{u}'_a] \cdot \nabla \psi_n dV,$$

$$I_3^{sa} = \int \left[\boldsymbol{u}'_s \cdot \nabla \boldsymbol{u}'_a + \frac{\rho'_s}{\bar{\rho}} \frac{\partial \boldsymbol{u}'_a}{\partial t} \right] \cdot \nabla \psi_n dV, \qquad I_3^{\Omega\Omega} = \int [\boldsymbol{u}'_\Omega \cdot \nabla \boldsymbol{u}'_\Omega] \cdot \nabla \psi_n dV,$$

$$I_3^{ss} = \int \left[\boldsymbol{u}'_s \cdot \nabla \boldsymbol{u}'_s + \frac{\rho'_s}{\bar{\rho}} \frac{\partial \boldsymbol{u}'_s}{\partial t} \right] \cdot \nabla \psi_n dV, \qquad I_3^{s\Omega} = \int [\boldsymbol{u}'_s \cdot \nabla \boldsymbol{u}'_\Omega] \cdot \nabla \psi_n dV,$$

$$I_3^{\Omega s} = \int [\boldsymbol{u}'_\Omega \cdot \nabla \boldsymbol{u}'_s] \cdot \nabla \psi_n dV.$$

Both terms in the integral I_4 depend on pressure. Since $p'_\Omega = p'_s = 0$, only five of the nine integrals are nonzero after substitution for p' and $\boldsymbol{u}'$.

$$I_4^{aa} = \frac{\partial}{\partial t} \int (\bar{\gamma} p'_a \nabla \cdot \boldsymbol{u}'_a + \boldsymbol{u}'_a \cdot \nabla p'_a) \psi_n dV$$

$$I_4^{a\Omega} = \frac{\partial}{\partial t} \int (\bar{\gamma} p'_a \nabla \cdot \boldsymbol{u}'_\Omega) \psi_n dV$$

$$I_4^{as} = \frac{\partial}{\partial t} \int (\bar{\gamma} p'_a \nabla \cdot \boldsymbol{u}'_s) \psi_n dV$$

$$I_4^{\Omega a} = \frac{\partial}{\partial t} \int (\boldsymbol{u}'_\Omega \cdot \nabla p'_a) \psi_n dV$$

$$I_4^{sa} = \frac{\partial}{\partial t} \int (\boldsymbol{u}'_s \cdot \nabla p'_a) \psi_n dV$$

Using the isentropic relation $\rho'_a/\bar{\rho} = p'_a/\bar{\gamma}\bar{p}$, the integrals I_3^{aa} and I_4^{aa} can be combined to produce the second-order gasdynamics terms developed in

Chapter 2. The remaining terms in I_3 and I_4 are either linear in acoustic fluctuations or second-order in non-acoustic fluctuations. The final form of the two integrals is thus

$$-\frac{\bar{a}^2}{\bar{p}E_n^2}\left\{\bar{\rho}I_3+\frac{1}{\bar{a}^2}I_4\right\}=-\sum_{i=1}^{\infty}\sum_{j=1}^{\infty}\left[A_{nij}\dot{\eta}_i\dot{\eta}_j+B_{nij}\eta_i\eta_j\right] + \sum_{i=1}^{\infty}\left[\left(\xi_{ni}^{v(3)}+\xi_{ni}^{v(4)}\right)\dot{\eta}_i+\xi_{ni}^{(3)}\eta_i\right]+\Xi_n^{(3)}, \quad (6.24)$$

where $\Xi_n^{(3)}$ has been defined as

$$\Xi_n^{(3)}\equiv-\frac{\bar{a}^2}{\bar{p}E_n^2}\left\{\bar{\rho}(I_3^{\Omega\Omega}+I_3^{\Omega s}+I_3^{s\Omega}+I_3^{ss})\right\}. \quad (6.25)$$

Schematically, then, after Eqs. (6.21), (6.22), and (6.24) are substituted in the right-hand side, the set of forced oscillator equations takes the form

$$\ddot{\eta}_n+\omega_n^2\eta_n=2\alpha_n\dot{\eta}_n+2\omega_n\theta_n\eta_n-\sum_{i=1}^{\infty}\sum_{j=1}^{\infty}\left[A_{nij}\dot{\eta}_i\dot{\eta}_j+B_{nij}\eta_i\eta_j\right] + (F_n)_{\text{other}}^{\text{NL}}+\sum_{i=1}^{\infty}\left[\xi_{ni}^{v}\dot{\eta}_i+\xi_{ni}\eta_i\right]+\Xi_n, \quad (6.26)$$

where we have defined

$$\xi_{ni}^{v}=\xi_{ni}^{v(3)}+\xi_{ni}^{v(4)}, \quad (6.27)$$

$$\xi_{ni}=\xi_{ni}^{(3)}, \quad (6.28)$$

$$\Xi_n=\Xi_n^{(1)}+\Xi_n^{(3)}. \quad (6.29)$$

This system of equations is very complex and there are many free parameters. For instance, if we truncate the system to N modes, there are $2N$ linear parameters and an additional $2N^2+N$ unknown functions. In order to simplify the equations somewhat, we will therefore neglect cross-coupling terms in

ξ^v_{ni} and ξ_{ni}, i.e., terms with $n \neq i$. These terms may turn out to be important, but neglecting them will allow for easier initial computation of results and will suffice for the purposes here. The simplified set of equations is

$$\ddot{\eta}_n + \omega_n^2 \eta_n = 2\alpha_n \dot{\eta}_n + 2\omega_n \theta_n \eta_n - \sum_{i=1}^{\infty}\sum_{j=1}^{\infty}[A_{nij}\dot{\eta}_i\dot{\eta}_j + B_{nij}\eta_i\eta_j] + (F_n)^{\mathrm{NL}}_{\mathrm{other}} + \xi^v_n(t)\dot{\eta}_n + \xi_n(t)\eta_n + \Xi_n(t). \quad (6.30)$$

6.2 Modeling of the Stochastic Sources

The problem has now been reduced to solving Eq. (6.30) for the time-dependent amplitudes $\eta_n(t)$. The source terms $\xi^v_n(t)$, $\xi_n(t)$, and $\Xi_n(t)$ represent stochastic processes of some sort and are responsible, in this formulation, for the background noise found in the power spectra of test firings. The problem of modeling these processes, however, remains. This requires specification of both the spatial and temporal distribution of the velocity and the entropy. At the present time, no models exist for these fluctuations.

There are several other paths that can be followed at this point which include obtaining approximate representations for the velocity and entropy fluctuations based on experimental data or numerical simulations. The approach that will be taken here is to assume forms for the source terms which are based on observations of experiments. By inspection of the pressure traces of test firings, it is apparent that the stochastic processes in real systems are broadband with very small correlation times*, τ_c. The limit $\tau_c \to 0$ represents a delta correlated process, i.e., a process which is totally uncorrelated with itself. It is thus interesting to study this limiting case and assume that the stochastic terms are represented by *white noise.*

*The correlation time is the time above which the autocorrelation function is zero. This is a measure of the dependence of the process on its past.

The definition of a white noise process is a process whose spectral density is flat, i.e., all frequencies are present at the same amplitude. Although such a process cannot occur in a real system, white noise can be a very useful tool for studying real processes which have very small correlation times compared to the macroscopic times of the system. This is true of the random processes and systems of interest [20]. Therefore, we will approximate ξ_n^v, ξ_n, and Ξ_n by mutually independent white noise processes with zero mean values and intensities $\sigma_n^{\xi^v}$, σ_n^{ξ}, and σ_n^{Ξ}.

By defining $\zeta_n(t) = \dot{\eta}_n(t)$, the second-order system (6.30) can be rewritten as an equivalent first-order system.

$$d\eta_n = \zeta_n dt \tag{6.31}$$
$$d\zeta_n = 2\alpha_n\zeta_n dt + 2\omega_n\theta_n\eta_n dt + F_n^{\mathrm{NL}}dt + \zeta_n\xi_n^v dt + \eta_n\xi_n dt + \Xi_n dt$$

The forcing function F_n^{NL} contains nonlinear contributions from gasdynamics and other processes, such as combustion. Since we are approximating the stochastic processes by white noise, the following substitutions can be made [31].

$$dW_n^{\xi^v}(t) \equiv \xi_n^v dt, \tag{6.32}$$
$$dW_n^{\xi}(t) \equiv \xi_n dt, \tag{6.33}$$
$$dW_n^{\Xi}(t) \equiv \Xi_n dt, \tag{6.34}$$

where $W_n^{\xi^v}(t)$, $W_n^{\xi}(t)$, and $W_n^{\Xi}(t)$ are independent Wiener processes. Using this new notation, the system of equations becomes

$$d\eta_n = \zeta_n dt, \tag{6.35}$$
$$d\zeta_n = 2\alpha_n\zeta_n dt + 2\omega_n\theta_n\eta_n dt + F_n^{\mathrm{NL}}dt + \zeta_n dW_n^{\xi^v}(t) + \eta_n dW_n^{\xi}(t) + dW_n^{\Xi}(t).$$

Thus, we are now interested in solving a system of stochastic differential equations with both additive and multiplicative noise. Throughout the rest of this chapter, these two types of noise will be referred to as external excitations and parametric excitations, respectively.

6.2.1 Stochastic Differential Equations

Unlike differential equations in ordinary calculus, there is an infinite number of ways to interpret differential equations with stochastic source terms. This is due to the highly erratic nature of white noise. Of the infinite possibilities, however, there are only two commonly used interpretations: the Ito and the Stratonovich representations. While the Ito representation has a better mathematical basis, the Stratonovich representation allows the use of the rules of ordinary calculus and often has more physical meaning. Which representation is best depends upon the physics of the particular case under investigation.

This is best illustrated through a simple example taken from Gardiner [31, page 103]. Consider the stochastic differential equation

$$dx = xdW(t), \tag{6.36}$$

with the initial condition

$$x(0) = 1. \tag{6.37}$$

If this equation is interpreted in the Stratonovich sense, the solution is

$$x(t) = e^{[W(t)-W(0)]}. \tag{6.38}$$

The expected value of $x(t)$ can be calculated using the formula

$$E(e^z) = e^{\{E(z^2)/2\}} \tag{6.39}$$

and the expected value of the square of the Wiener process, which is of course

$$E\left([W(t) - W(0)]^2\right) = t. \tag{6.40}$$

Therefore, the expected value of $x(t)$ is

$$\begin{aligned} E(x(t)) &= E\left(e^{[W(t)-W(0)]}\right) && (6.41)\\ &= e^{\left\{E\left([W(t)-W(0)]^2\right)/2\right\}} && (6.42)\\ &= e^{t/2}, && (6.43) \end{aligned}$$

For the same equation, the Ito sense yields

$$x(t) = e^{\{[W(t)-W(0)]-\frac{1}{2}t\}}, \tag{6.44}$$

with an expected value of

$$\begin{aligned} E(x(t)) &= E\left(e^{[W(t)-W(0)]-t/2}\right) && (6.45)\\ &= e^{\left\{E\left([W(t)-W(0)]^2\right)-t\right\}/2} && (6.46)\\ &= 0. && (6.47) \end{aligned}$$

Thus, the Ito and Stratonovich representations give two vastly different answers for this problem. In the Ito case, the variable fluctuates near zero, while in the Stratonovich case, it grows without bound.

The reason for this discrepancy is that the Stratonovich representation is anticipating, while the Ito representation is nonanticipating. This can be

shown using the equivalent difference equation.

$$\Delta x = x\Delta W(t) \tag{6.48}$$

In the definition of the Stratonovich integral, the integrand is evaluated at the midpoint between the lower and upper limits of integration. Therefore, the difference equation can be written

$$x_{i+1} = x_i + \frac{x_{i+1} + x_i}{2}(W_{i+1} - W_i). \tag{6.49}$$

Due to the multiplicative term $x_{i+1}(W_{i+1} - W_i)$, the system anticipates the next value of the Wiener process. However, the evaluation point for the Ito integral is at the lower limit of integration, and the difference equation becomes

$$x_{i+1} = x_i + x_i(W_{i+1} - W_i). \tag{6.50}$$

In this case, the right-hand side does not depend on x_{i+1}, and the system is nonanticipating. Therefore, the reason for the discrepancy is that in the Stratonovich case, the variable $x(t)$ anticipates the next value of the Wiener process, while in the Ito case, it does not.

The choice between the two representations is then as follows. If there is a correlation between the noise and the system, i.e. the system is anticipating, then the Stratonovich representation should be used. On the other hand, if the actual noise process is in fact truly random, i.e., the system does not anticipate its next value, then the Ito representation is the correct choice.

Here, the terms ξ_n^v, ξ_n, and Ξ_n represent real noise processes with small but finite correlation times. In the limit $\tau_c \to 0$, we are approximating these real processes by white noise. In the actual system, the acoustics of the chamber will anticipate the real noise processes due to nonzero correlation times.

Therefore, the Stratonovich representation is a more appropriate choice due to its anticipating nature [31, page 105]. We will thus assume that the system (6.35) is composed of Stratonovich differential equations and treat them accordingly. For more information on the intricacies of stochastic differential equations, see Gardiner [31] or Horsthemke and Lefever [35].

In our study, it will be necessary to numerically simulate the system of stochastic differential equations. Euler's method is the most common procedure used to simulate Ito stochastic differential equations. However, in order to use this method with Stratonovich differential equations, the system must first be transformed to an equivalent system of Ito equations using the Wong-Zakai theorem. This complicates matters unnecessarily. If instead we use a second-order Runge-Kutta method, the Stratonovich differential equations can be simulated directly. This can be shown by writing the differential equations as equivalent difference equations and then substituting them into the second-order Runge-Kutta algorithm. We will approximate the Wiener processes using variates generated by the Box-Muller transformation [30, page 309].

An example of a simulation using this method is presented in Fig. 6.1. A sample pressure trace is shown along with the corresponding normalized spectrum. Inspection of the spectrum shows the distinct frequencies which are associated with an acoustic instability, along with broadband background noise. This is characteristic of actual test data of a case when an instability is present.

6.3 Monte-Carlo Simulations

In the previous chapters, we have studied only deterministic systems. Since we are now interested in nondeterministic systems, it is natural to use the

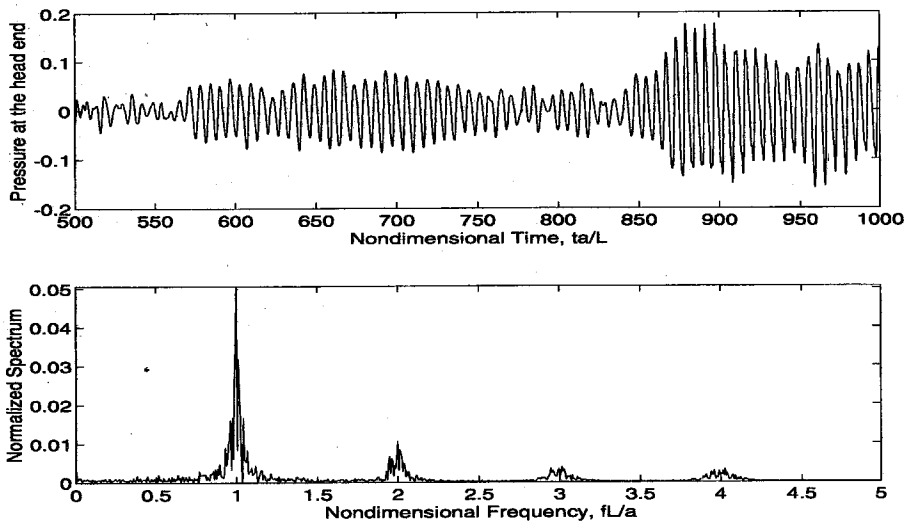

Figure 6.1 Sample pressure trace and normalized spectrum for one simulation

probability density functions of the amplitudes of acoustic modes to investigate the dynamics of the system. There are two main ways of determining these probability density functions: solution of the corresponding Fokker-Planck equation and through the use of Monte-Carlo simulations.

The Fokker-Planck equation describes the time evolution of the probability density functions of the acoustic amplitudes. It can be constructed using the coefficients of the system of stochastic differential equations. Even for relatively simple systems, however, the Fokker-Planck is extremely difficult to solve; see, e.g., Franklin and Rodemich [28]. Therefore, we will use the second method to calculate results for this chapter.

The Monte-Carlo method provides a means of approximating the probability density functions without the difficulty of solving the Fokker-Planck equation. In this method, a series of numerical "experiments" is conducted, usually in the same manner that one would conduct actual experiments. After the flow field has become well-developed (say 1000 periods of the fundamental mode or so), the amplitudes of the acoustic modes are sampled. The results

are then used to construct histograms which, after normalization, approximate the instantaneous probability density functions of the modal amplitudes. The approximation becomes better as the number of experiments is increased.

In the current study, each Monte-Carlo simulation will consist of 10000 numerical experiments. The linear parameters will be fixed throughout a series of experiments, while the initial conditions for the simulations will be varied systematically. In particular, a square initial pulse which is nonzero from $0 \leq x/L \leq .25$ will be used. The size of the pressure pulse $p'/\bar{p}$ will be varied from 0 to .2 linearly so as to include all likely values.

6.4 Results

For initial results, we will use the simplest possible set of equations. The system will be truncated to two modes with noise included explicitly only in the fundamental mode. In addition, we will assume initially that the only nonlinear contributions are associated with gasdynamics. These simplifications were used by Culick et al. [20] and will allow the effects of each type of stochastic process to be determined. In Sec. 6.4.4, some of these simplifications will be relaxed to investigate the effects of noise when nonlinear contributions from combustion are also included.

Note that for the results given in this chapter, it is more convenient to work in terms of the amplitude r_n instead of η_n. By utilizing this variable, all attractive states of the system will be either stable or unstable steady states. This allows us to avoid dealing with limit cycles which are not as well-defined for stochastic dynamical systems.

6.4.1 The Effects of an External Excitation

The term Ξ_1 is an external excitation, i.e., it does not depend on the current state of the system. As a result, this type of excitation does not change the qualitative behavior of the system from that of the original deterministic system [35]. No matter how large the intensity, the addition of an external excitation does not affect the locations or types of attractors in the system. Instead, an external excitation provides only a random perturbation from these states; the dynamics of the system are constantly striving to bring the system back to a state of equilibrium.

To better understand the effects of an external excitation, it is useful to treat the deterministic case as the limit of $\Xi_1 \to 0$. For a deterministic system with nonlinear gasdynamics only, the stationary probability density functions will be delta functions in terms of r_n. For example, the probability density functions of a linearly stable system will be delta functions at $r_n = \eta_n = 0$, for all n. When an external excitation is introduced, the effect is to broaden the delta peaks about the mean value. This broadening effect can be seen in Figs. 6.2 and 6.3 for linearly stable and unstable systems, respectively. It should be noted that the nonzero mean value seen in Fig. 6.2 is a result of the transformation from η_1 to r_1. The amplitude η_1 will still have a mean value of zero, as expected.

To demonstrate the effect of noise intensity on the probability density, the value used in Fig. 6.3 was doubled, and the result plotted in Fig. 6.4. As the intensity of the noise increases, the variance of the probability density function increases so that a larger range of modal amplitudes is likely. The mean value of the amplitude, however, remains unchanged.

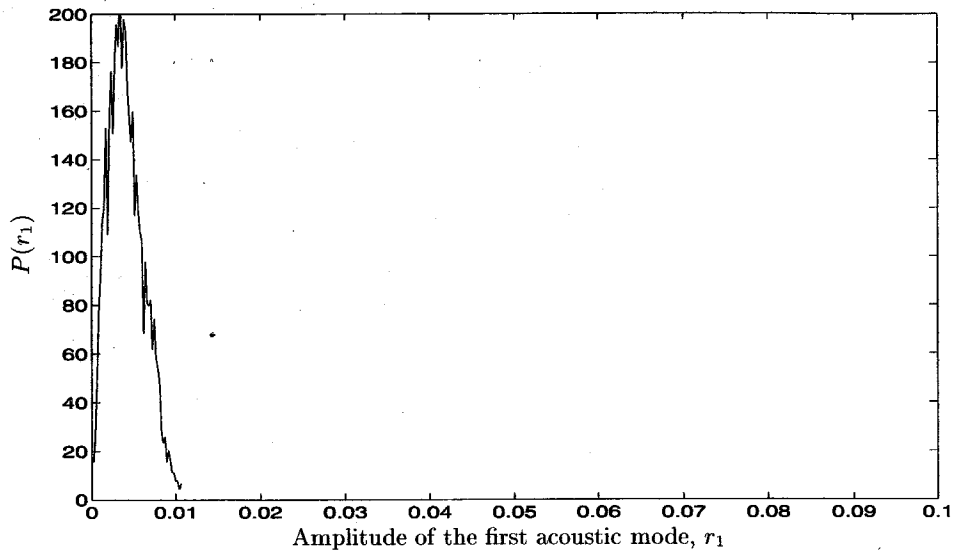

Figure 6.2 The influence of an external excitation of the fundamental mode only on a linearly stable system; 2 modes, $\sigma_1^{\Xi} = 0.0005 \text{ sec}^{-3/2}$, $\alpha_1 = -25 \text{ sec}^{-1}$

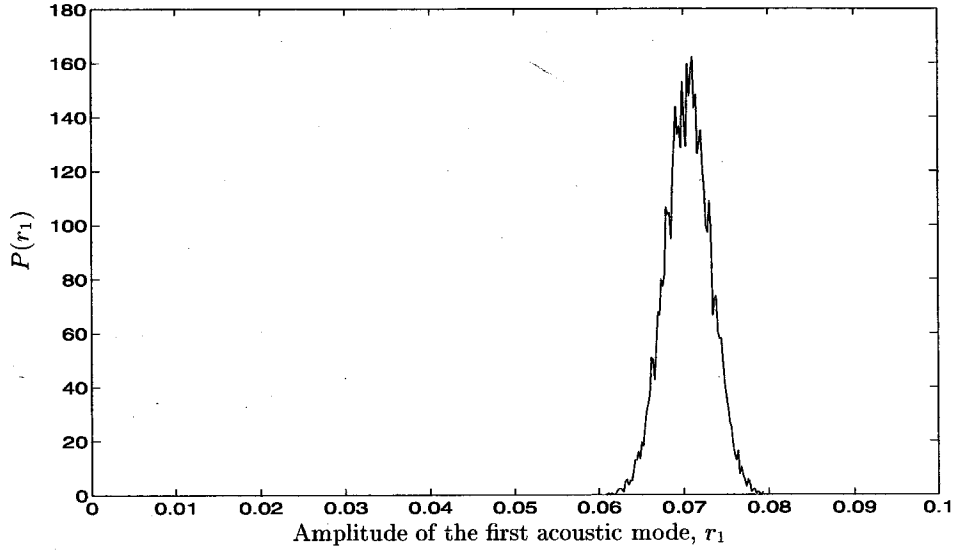

Figure 6.3 The influence of an external excitation of the fundamental mode only on a linearly stable system; 2 modes, $\sigma_1^{\Xi} = 0.0005 \text{ sec}^{-3/2}$, $\alpha_1 = 25 \text{ sec}^{-1}$

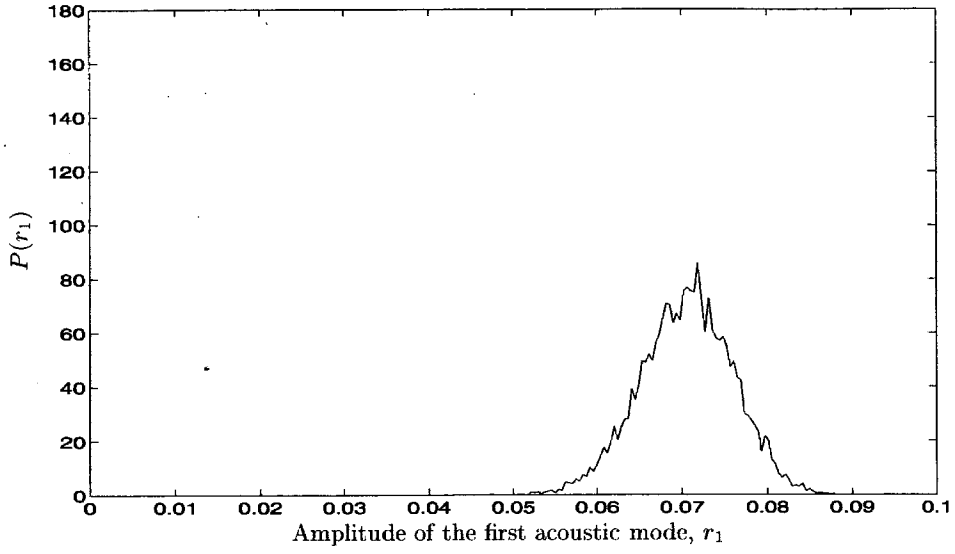

Figure 6.4 The influence of increasing the intensity of an external excitation of the fundamental mode only; 2 modes, $\sigma_1^{\Xi} = 0.001$ $\sec^{-3/2}$, $\alpha_1 = 25$ $\sec^{-1}$

6.4.2 The Effects of a Noisy Linear Growth Rate

Unlike the external excitations covered in the previous section, the parametric excitations $\xi_1^v \dot{\eta}_1$ and $\xi_1 \eta_1$ depend upon the current state of the system. In a more illuminating form, the system (6.30) can be rewritten as

$$\ddot{\eta}_1 + \omega_1^2 \eta_1 = 2\left(\alpha_1 + \frac{1}{2}\xi_1^v\right)\dot{\eta}_1 + 2\omega_1\left(\theta_1 + \frac{1}{2\omega_1}\xi_1\right)\eta_1 + (F_1)^{\mathrm{NL}} + \Xi_1(t),$$
$$\ddot{\eta}_2 + \omega_2^2 \eta_2 = 2\alpha_2\dot{\eta}_2 + 2\omega_2\theta_2\eta_2 + (F_2)^{\mathrm{NL}}. \tag{6.51}$$

By inspection of the above system, it is easy to see that ξ_1^v is a random perturbation of the linear growth rate of the first acoustic mode. Similarly, ξ_1 is a random perturbation of the linear frequency shift. In this section, we will study the effects of a noisy linear growth rate on the dynamics of the system, while the effects of a noisy linear frequency shift will be handled in the next section.

There are two main effects which are caused by the noisy linear growth rate ξ_1^v. The first is a result of approximating a real noise process by white noise. Since no real process is truly white, the system will have a small but finite memory, i.e., there will be some correlation between the noise and the system. This correlation is taken into account by the Stratonovich representation through its definition of the stochastic integral [35]. As a result, the linear growth rate is increased to an apparent value given by

$$(\alpha_1)_{\text{apparent}} = \alpha_1 + \left(\frac{\sigma_1^{\xi^v}}{2}\right)^2 . \tag{6.52}$$

Thus, one effect of a noisy linear growth rate is to shift the bifurcation diagram by an amount proportional to the square of the intensity of the noise. This is also known as noise-induced drift [35]. The second effect of the noisy linear growth rate is similar to the effect of an external excitation. It is basically a disorganizing effect which tends to spread the peak of the probability density functions about the mean value.

This type of parametric excitation was studied by Horsthemke and Lefever [35] on a first-order nonlinear equation. In that study, the Verhulst model with a noisy growth rate was shown to have two transition points at which the probability density function changes qualitatively. Thus, there are three ranges of linear growth rate which produce three different types of probability density function. The same types of probability density functions were found in the acoustic equations with a noisy linear growth rate. However, in our system, it is difficult to predict the exact location of the transition due to the highly nonlinear nature of the equations.

For highly stable systems, i.e., $\alpha_1 \ll 0$ sec^{-1}, the attractor at $r_n = 0$ is so strong that the solution will always be drawn back to this steady state. As a result, the stationary probability density functions for highly stable systems

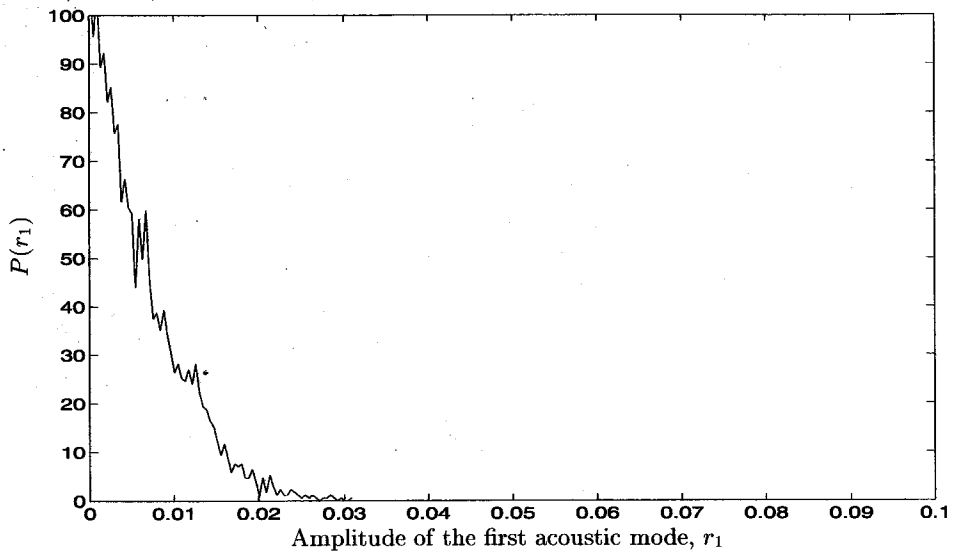

Figure 6.5 Probability density function for a system with a noisy linear growth rate in the fundamental mode only; 2 modes, $\sigma_1^{\xi^v} = 0.01$ sec$^{-3/2}$, $\alpha_1 = -8$ sec^{-1}

will be delta functions at $r_n = 0$ for all n. For mildly stable and/or unstable systems, a second type of probability density function occurs. While the most probable value is still zero, the mean value is not. This type of probability density function was shown previously in the study by Culick et al. [20]. An example is shown here in Fig. 6.5 for $\alpha_1 = -8$ sec^{-1}.

The final type of probability density occurs in systems which are more unstable. In that case, the linear growth rate α_1 is so large that it is unlikely that the noise will be strong enough for a sufficient amount of time to drive the solution back to the trivial state. Therefore, both the mean value and the most probable value are nonzero. Figure 6.6 shows an example of such a probability density function for $\alpha_1 = 25$ sec^{-1}. Note that the mean value is slightly from the deterministic value of 0.07. This is an example of noise-induced drift..

Recall that in the deterministic system, only two qualitatively different regions are found. When noise of a parametric nature is added, three distinct regions arise because $r_n = 0$ is a stationary point of the system for all values

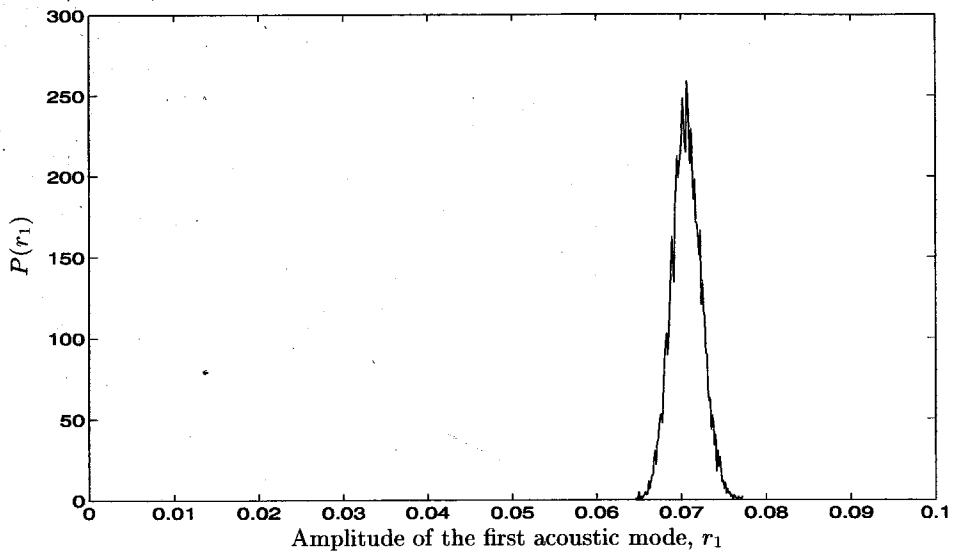

Figure 6.6 Probability density function for a system with a noisy linear growth rate in the fundamental mode only; 2 modes, $\sigma_1^{\xi^v} = 0.005$ sec$^{-3/2}$, $\alpha_1 = 25$ sec^{-1}

of α_1 and σ^{ξ^v} [35]. However, if an external excitation is also included in the system, r_n is no longer a stationary state, and only two different regions are found.

6.4.3 The Effects of a Noisy Linear Frequency Shift

The effects of a noisy linear frequency shift are very similar to the effects of ξ_1^v, so only a brief discussion is necessary. Since ξ_1 is also a parametric excitation, a stationary state occurs once again for $r_n = 0$, and three regions of distinct types of probability density functions are produced. The three types are qualitatively similar to those in the previous section, although the transition points may occur at different values of α_1. A sample probability density function for a linearly unstable system with a noisy linear frequency shift is plotted in Fig. 6.7.

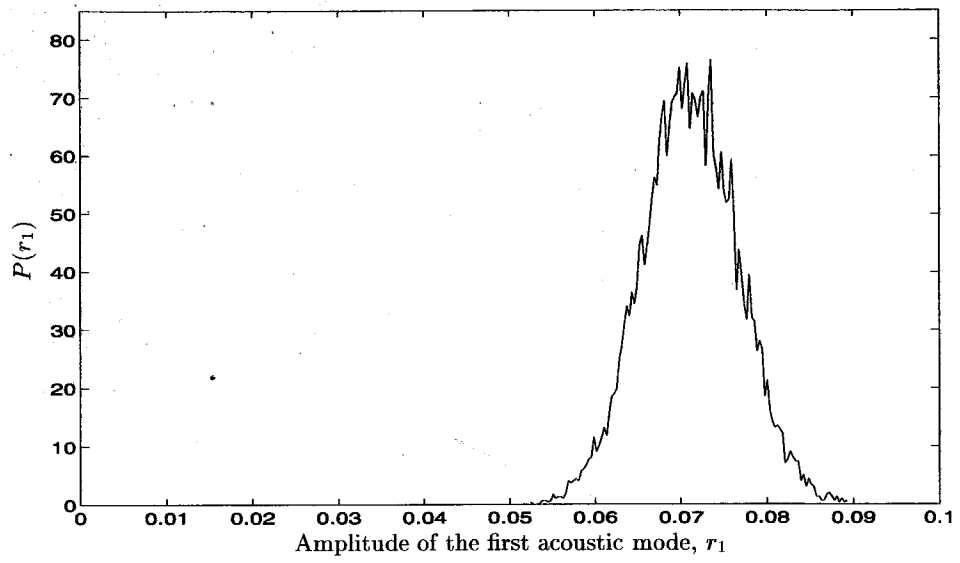

Figure 6.7 Probability density function for a system with a noisy linear frequency shift in the fundamental mode only; 2 modes, $\sigma_1^{\xi} = 0.025 \text{ sec}^{-1/2}$, $\alpha_1 = 25 \text{ sec}^{-1}$

6.4.4 The Effects of Noise and Nonlinear Combustion

In the previous sections, it was assumed that the only nonlinear processes present in the system were associated with gasdynamics. We will now study the case in which nonlinear contributions from both gasdynamics and combustion are included. Two additional assumptions will also be relaxed in this section. First, we will include four modes in the simulations instead of only two. Second, we will include stochastic sources explicitly in both the first and second acoustic modes.

When nonlinear combustion is added to the stochastic system (6.30), the resulting probability density functions can be quite different, as one might expect. In order to investigate the possible influences of nonlinear combustion processes in the presence of noise, we will introduce the threshold velocity model into the system. We have previously shown in Chapter 5 that this model can produce regions of possible triggering in which two stable solutions

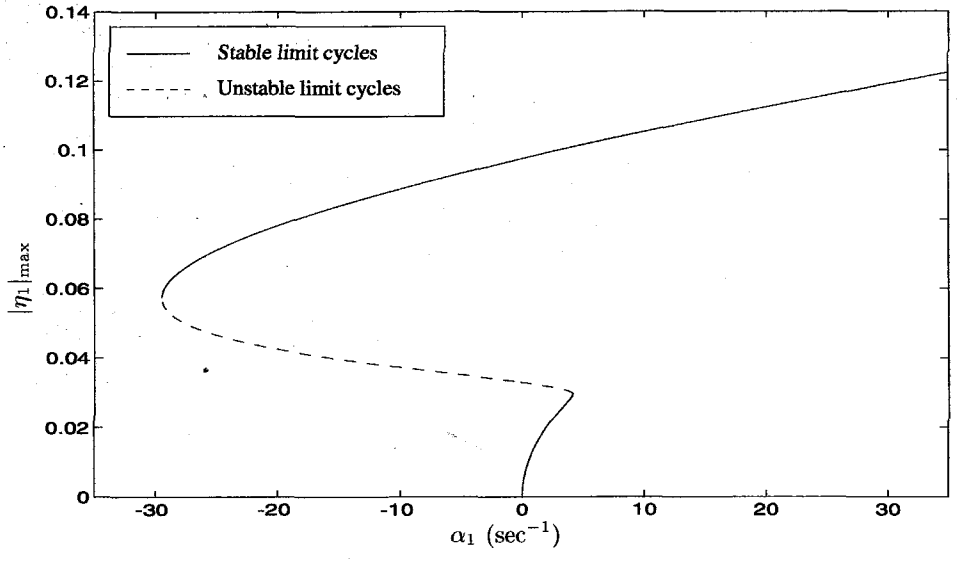

Figure 6.8 Bifurcation diagram for the deterministic system; threshold velocity model, $u_t/\bar{a} = 0.03$, $\bar{R}_{\rm vc} = 7.8$, 4 modes

exist simultaneously. In a stochastic system, this corresponds to a bimodal probability density function such that there is a high probability of low and high amplitudes and a low probability of intermediate values.

For the results in this section, we will use $u_t/\bar{a} = 0.03$ and $\bar{R}_{\rm vc} = 7.8$ for the parameters in the threshold velocity model. Using these values along with the linear parameters from Table 4.1, the bifurcation diagram for the deterministic system is shown in Fig. 6.8. This diagram will be useful in the discussion of results. In addition, the following values were chosen for the intensities of the stochastic sources: $\sigma_n^{\xi^v} = 0.005$ sec$^{-3/2}$, $\sigma_n^{\xi} = 0.025$ sec$^{-1/2}$, and $\sigma_n^{\Xi} = 0.0005$ sec$^{-3/2}$, for $n = 1, 2$. In the figures of this section, we will vary only α_1 while keeping all other parameters fixed. By changing this parameter, we will demonstrate a variety of the possible forms of the probability density functions.

From inspection of Fig. 6.8, we see that the region of possible triggering begins at approximately $\alpha_1 = -30$ sec^{-1} for the deterministic system. Below

this value, the system is stable to any size perturbation. To illustrate the effect of noise on such a system, a linear growth rate of -35 sec^{-1} was chosen. Figure 6.9 shows the resulting probability density function for the first acoustic mode. Note that this closely resembles Fig. 6.2 in which only an external excitation was included. For this case, the attractor of the deterministic system, i.e., the trivial steady state, is so strong that the amplitudes never reach large values. Therefore, the parametric excitations have a very small effect on the system. Most of the noise contribution is a result of the external excitation.

As the linear growth rate is increased to a value above -30 sec^{-1}, we enter the region of possible triggering where an additional attractive state is present. Three values of α_1 were chosen in order to show how the probability density of the fundamental mode changes throughout this region; see Figs. 6.10–6.12. As the value of α_1 is varied, the regions of attraction of the stationary states will change. This will have a noticeable effect on the probability density functions.

The first value of α_1 was chosen very near the lower boundary of the region of possible triggering. For a value of $\alpha_1 = -25$ sec^{-1}, Figure 6.10 shows the probability density function of the fundamental mode. The low amplitude attractive state is dominant because the region of attraction for this state is larger. However, the effect of the high amplitude attractive state is still present, resulting in a long tail in the probability density function.

As we increase α_1 further to a value of -20 sec^{-1}, the effect of the high amplitude state becomes more noticeable, as shown in Figure 6.11. The regions of attraction of the two states are becoming more equal so that amplitudes surrounding both states have high probabilities. Note that the probability density function is continuous, and the intermediate values are nonzero. This means that the background noise can lead to a qualitative change in the behavior of the system. This is not consistent with the usual definition of triggering in which a larger amplitude perturbation is necessary.

Figure 6.12 corresponds to $\alpha_1 = -10$ sec^{-1}. This figure is a good example of triggering in the presence of noise. The background noise is generally insufficient to cause transition from the low amplitude state to the high amplitude state.. However, since we are assuming Gaussian distributed noise, even large amplitude perturbations are possible, and the stationary probability density function will in fact be continuous. The probability of intermediate amplitudes will, nonetheless, be very small.

The last two figures illustrate the changes in the probability density function as the deterministic system becomes linearly unstable. For a linear growth rate of $\alpha_1 = 5$ sec^{-1}, there are two stable limit cycles in the deterministic system. This is apparent in the probability density function shown in Fig. 6.13. The region of attraction of the low amplitude state is small, and the higher amplitude state is more likely. Finally, Fig. 6.14 shows a case in which only one stable state is present.

6.5 Concluding Remarks

The current chapter has investigated some of the intricacies of systems involving stochastic excitations. First, the flow field was split into acoustic and nonacoustic parts in order to determine the general form of noise processes in the context of combustion instabilities. The resulting terms depend on the spatial and temporal distribution of both velocity and entropy fluctuations. As no models of these processes are available, we have chosen to represent them by Gaussian white noise.

The system of stochastic differential equations is very complex with many free parameters. In order to obtain initial results, we have ignored cross-coupling noise terms, as well as noise terms in higher modes. In general, these processes may be important and should actually be included. However, the

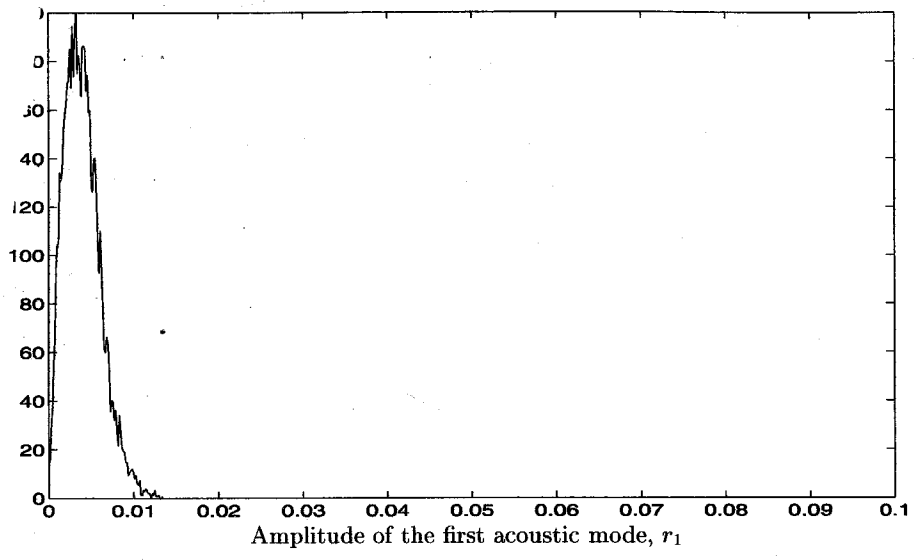

Figure 6.9 Probability density function for the first acoustic mode for $\alpha_1 = -35$ sec^{-1} using the threshold velocity model; $u_t/\bar{a} = 0.03$, $\bar{R}_{\text{vc}} = 7.8$, 4 modes

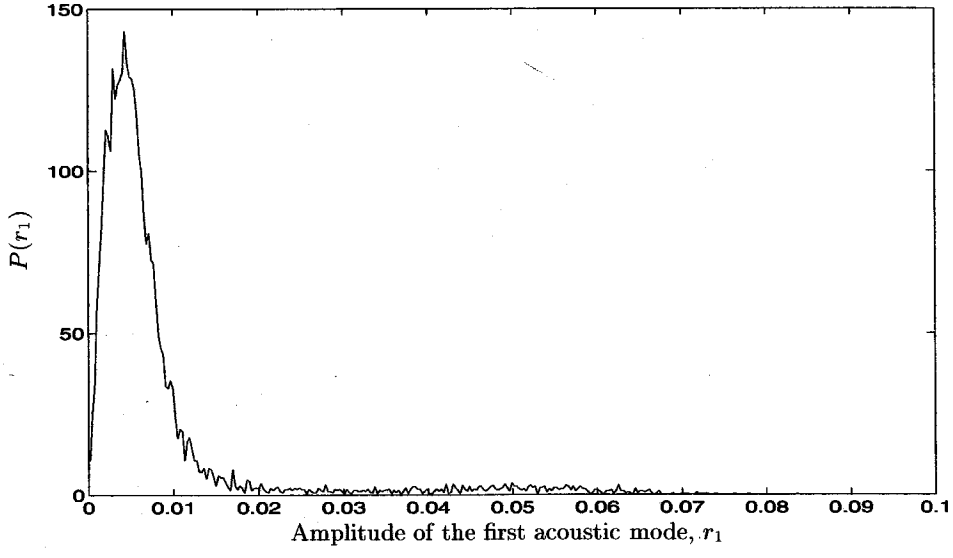

Figure 6.10 Probability density function for the first acoustic mode for $\alpha_1 = -25$ sec^{-1} using the threshold velocity model; $u_t/\bar{a} = 0.03$, $\bar{R}_{\text{vc}} = 7.8$, 4 modes

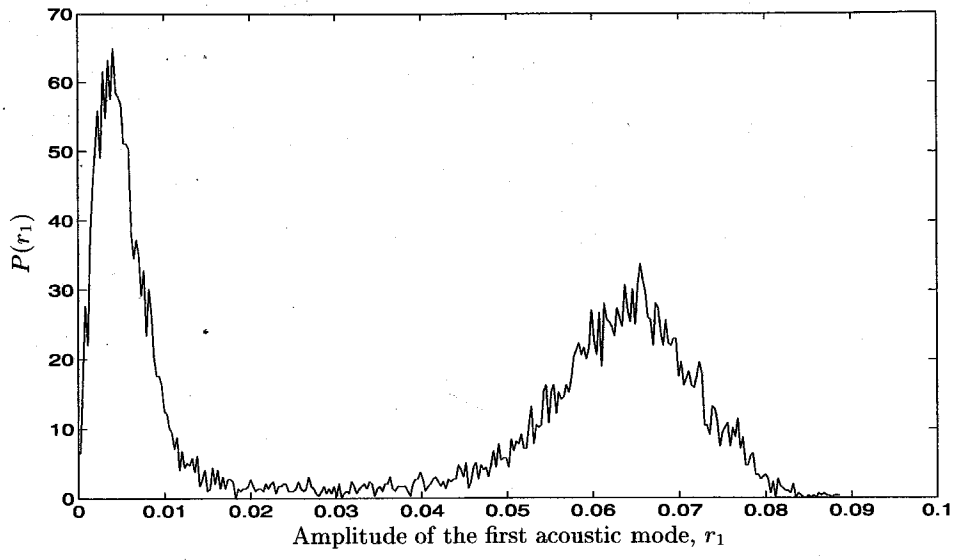

Figure 6.11 Probability density function for the first acoustic mode for $\alpha_1 = -20$ sec^{-1} using the threshold velocity model; $u_t/\bar{a} = 0.03$, $\bar{R}_{\text{vc}} = 7.8$, 4 modes

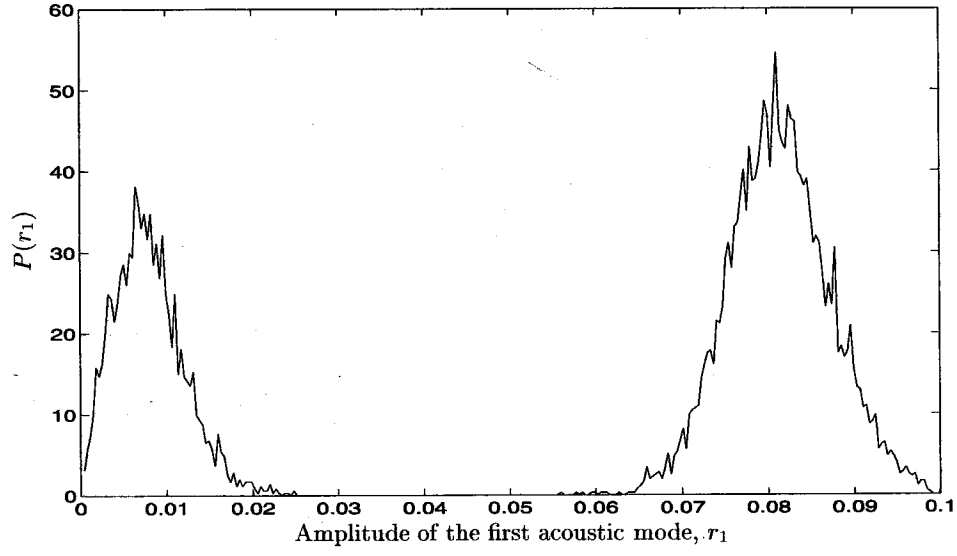

Figure 6.12 Probability density function for the first acoustic mode for $\alpha_1 = -10$ sec^{-1} using the threshold velocity model; $u_t/\bar{a} = 0.03$, $\bar{R}_{\text{vc}} = 7.8$, 4 modes

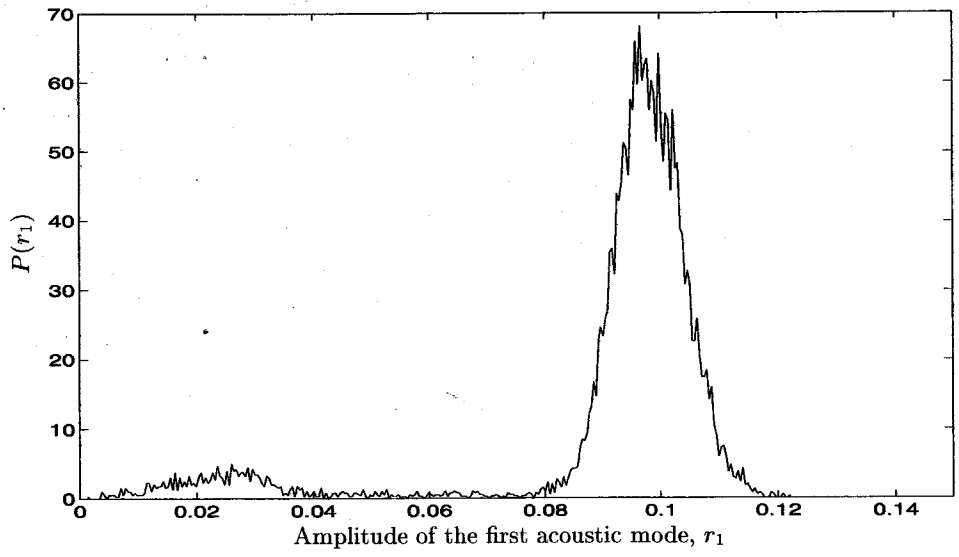

Figure 6.13 Probability density function for the first acoustic mode for $\alpha_1 = 5$ sec^{-1} using the threshold velocity model; $u_t/\bar{a} = 0.03$, $\bar{R}_{\text{vc}} = 7.8$, 4 modes

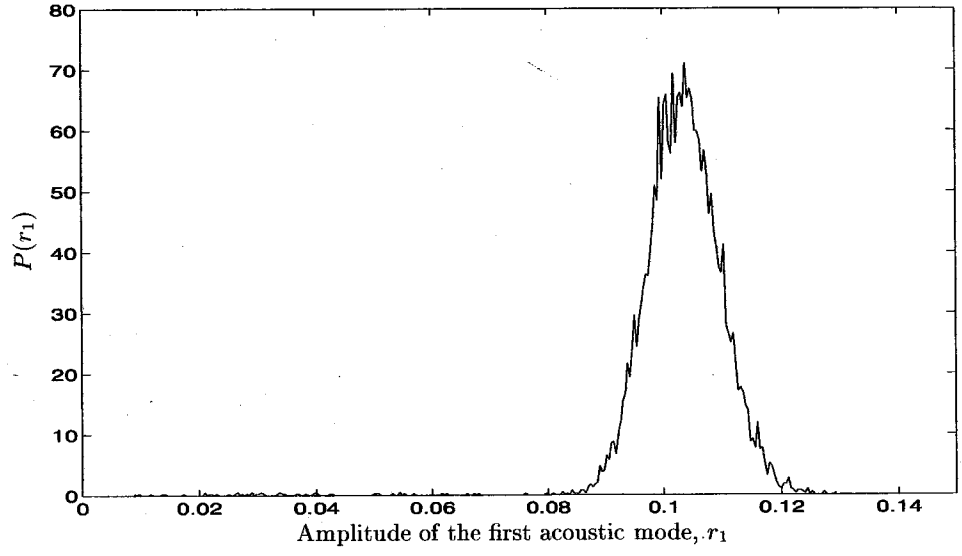

Figure 6.14 Probability density function for the first acoustic mode for $\alpha_1 = 10$ sec^{-1} using the threshold velocity model; $u_t/\bar{a} = 0.03$, $\bar{R}_{\text{vc}} = 7.8$, 4 modes

purpose here was mainly to investigate the possible influences of the types of excitations which are present in the system.

Using Monte-Carlo simulations, we have determined the effects of the three types of stochastic excitations on the acoustic amplitudes. This was performed for the case of nonlinear contributions from gasdynamics only. In addition, nonlinear contributions from combustion processes were added in order to determine the effects of noise on a system with more than one stationary state. In this case, bimodal probability density functions are possible.

The current investigation has only scratched the surface of this field of study. We have, in fact, treated only a limited number of specialized cases, and much work remains to be done. Most importantly, more realistic models of the actual stochastic processes are needed. This involves collecting statistical data of vorticity and entropy waves, either by experiment and/or computer simulation. Until this is achieved, models with nonzero correlation times, i.e., colored noise, should be used to better approximate the actual processes.

Chapter 7

Final Remarks

In the present work, many aspects of nonlinear combustion instabilities have been studied within the framework of an approximate analysis introduced by Culick [12]. This analysis leads to a set of coupled nonlinear equations which allows general trends to be obtained at a minimum of time and expense. In addition, any physical processes can easily be incorporated into this analysis.

In many past investigations, the method of time-averaging has been applied to the nonlinear oscillator equations without complete consideration of the possible consequences of this approximation. By applying the methods of dynamical systems theory, we have determined the effects of application of the method of time-averaging and truncation to a small number of modes. It was determined that the stability boundary found previously in the two mode, time-averaged equations is a result of time-averaging and is not an artifact of truncation to two modes as previously reported [38]. It was shown that this boundary limits the range in which there is good agreement between the time-averaged equations and the original oscillator equations. In particular, results will only be valid sufficiently far from the stability boundary. As more modes are included, the boundary shifts to a higher value of α but is still present. The results are thus valid for more highly unstable systems.

It is a well-established result that nonlinear gasdynamics is a source of energy transfer between acoustic modes. By studying the energy balance in the limit cycle, the present study has established that nonlinear gasdynamics also provides a means of shifting frequencies which are not initially integral multiples of the fundamental so that a periodic limit cycle may be reached. This is important in transverse oscillations because the frequencies of transverse oscillations are usually quite different from integral multiples. This additional role reduces the efficiency of energy transfer between modes, and higher amplitudes are required to produce a periodic limit cycle.

This finding suggests a way to decrease the amplitudes of transverse oscillations, and an example was presented showing this possibility. By suitable tuning of the linear frequency shifts θ_n, the efficiency of energy transfer between modes can be increased, thereby decreasing the modal amplitudes. Previous works have concentrated on reducing the linear growth rates as a method to decrease the amplitudes. The present results suggest that a change in the linear frequency shifts can have a more pronounced effect on the limiting amplitudes of spontaneous oscillations.

The effects of nonlinear combustion response were studied using several models. The first model represented nonlinear coupling to pressure oscillations. For parametric values corresponding to realistic propellants, the possibility of pulsed oscillations was not found. Two models representing coupling to velocity oscillations were also investigated. Although these models produce small regions of possible triggering for limited ranges of parametric values, both models seem to be inefficient at the type of coupling to nonlinear gasdynamics which leads to true nonlinear instabilities. Therefore, a new model was developed to determine the effect of a threshold velocity, a phenomenon that has been observed experimentally. The threshold velocity model was the only model which produced considerable regions of possible triggering. This

suggests that a threshold velocity may be important in pulsed instabilities.

In the last chapter, the assumptions that entropy and vorticity waves are negligible were relaxed. By including these contributions, the general forms for the sources of noise in a combustion chamber were developed. From the power spectra of motor tests, it is apparent that these processes are broad-band with very small correlation times. Therefore, the limiting case of white noise was investigated. Under this assumption, the effects of each of the three types of stochastic excitations were determined.

A previous work by Clavin et al. [8] had reported the possibility of pulsed oscillations, i.e., bimodal probability density functions, when multiplicative white noise was included in a single mode approximation to the acoustic field. However, in this study, no cases were located in which the addition of noise produced regions of possible triggering. Bimodal probability density functions were found only when the threshold velocity model was included in the analysis.

Appendix A

An Overview of Floquet Theory

In the present study, we are mainly interested in periodic solutions which are the result of bifurcation from a steady state solution of an autonomous problem. Therefore, we will restrict the current discussion accordingly.

Let us consider an n-dimensional system of the form

$$\dot{\boldsymbol{V}} = \boldsymbol{F}(\boldsymbol{V}), \tag{A.1}$$
$$\boldsymbol{F}(0) \neq 0,$$

which has steady solutions $\boldsymbol{V} = \boldsymbol{V}_0$. For the case $n > 1$, T-periodic solutions may bifurcate from the steady solutions. Define these T-periodic solutions as $\boldsymbol{u}(t) = \boldsymbol{u}(t+T)$. Now consider an arbitrary disturbance $\boldsymbol{v}$ of the solution $\boldsymbol{V}$ in the neighborhood of the bifurcation:

$$\boldsymbol{V} = \boldsymbol{V}_0 + \boldsymbol{u}(t) + \boldsymbol{v} \tag{A.2}$$

The derivative of the disturbance vector $\boldsymbol{v}$ is as follows:

$$\begin{aligned} \dot{\boldsymbol{v}} &= \boldsymbol{F}(\boldsymbol{V}_0 + \boldsymbol{u}(t) + \boldsymbol{v}) - \boldsymbol{F}(\boldsymbol{V}_0 + \boldsymbol{u}(t)) \\ &\equiv \boldsymbol{f}(\boldsymbol{u}(t), \boldsymbol{v}) \end{aligned} \tag{A.3}$$

where $\boldsymbol{f}(\boldsymbol{u}(t), \boldsymbol{v}) = \boldsymbol{f}(\boldsymbol{u}(t+T), \boldsymbol{v})$ and $\boldsymbol{f}(\boldsymbol{u}(t), 0) = 0$. Expanding $\boldsymbol{f}(\boldsymbol{u}(t), \boldsymbol{v})$ in a Taylor series about $\boldsymbol{v} = 0$ and keeping only first order terms, we find that

$$\boldsymbol{f}(\boldsymbol{u}(t), \boldsymbol{v}) = \boldsymbol{f}_{\boldsymbol{v}}(\boldsymbol{u}(t) \,|\, \cdot)\boldsymbol{v},$$

or

$$\dot{\boldsymbol{v}} = \boldsymbol{A}(t)\boldsymbol{v}, \tag{A.4}$$

where $\boldsymbol{A}(t)$ is a T-periodic vector which is defined as $\boldsymbol{A}(t) = \boldsymbol{f}_{\boldsymbol{v}}(\boldsymbol{u}(t) \,|\, \cdot)$.

The system of equations (A.4) is a linear, T-periodic, n-dimensional set of differential equations. It has n linearly independent solutions which we will denote as $\boldsymbol{v}_1(t), \ldots, \boldsymbol{v}_n(t)$. Arranging these solutions into a matrix whose columns are the vectors $\boldsymbol{v}_i(t)$, we obtain a fundamental solution matrix, $\boldsymbol{\Phi}(t)$. Furthermore, we impose that $\boldsymbol{\Phi}(0) = \boldsymbol{I}$, where $\boldsymbol{I}$ is the identity matrix.

The periodicity of the solution vectors $\boldsymbol{v}_i$ implies that the column vectors of $\boldsymbol{\Phi}(t+T)$ are linear combinations of the columns of $\boldsymbol{\Phi}(t)$, i.e.,

$$\boldsymbol{\Phi}(t+T) = \boldsymbol{\Phi}(t) \cdot \boldsymbol{C}, \tag{A.5}$$

where $\boldsymbol{C}$ is an $n \times n$ constant matrix. Substituting for $t = 0$, it follows that $\boldsymbol{C} = \boldsymbol{\Phi}(T)$. It is also easy to prove by induction that $\boldsymbol{\Phi}$ satisfies the equality [36].

$$\boldsymbol{\Phi}(nT) = \boldsymbol{\Phi}^n(T) \tag{A.6}$$

The eigenvalues of the fundamental solution matrix $\boldsymbol{\Phi}(T)$ are commonly

referred to as *Floquet multipliers*. They are found by solving the problem

$$\mathbf{\Phi}(T) \cdot \mathbf{\Psi} = \lambda(T)\mathbf{\Psi}, \tag{A.7}$$

where $\mathbf{\Psi}$ are the eigenvectors and $\lambda(T)$ are the eigenvalues or Floquet multipliers. Using Eqs. (A.6) and (A.7), we find that the Floquet multipliers satisfy the relation

$$\lambda^n(T) = \lambda(nT). \tag{A.8}$$

Therefore, $\lambda(T)$ can be written in the following form.

$$\lambda(T) = e^{\sigma T} \tag{A.9}$$

It can be shown that the solutions of $\dot{\boldsymbol{v}} = \boldsymbol{A}(t)\boldsymbol{v}(t)$ are given by [36]

$$\boldsymbol{v}(t) = \mathbf{\Phi}(t) \cdot \mathbf{\Psi}. \tag{A.10}$$

In order to study the stability of the solution $\boldsymbol{v}(t)$, consider the following.

$$\boldsymbol{v}(t + nT) = \mathbf{\Phi}(t + nT) \cdot \mathbf{\Psi} \tag{A.11}$$

$$= \mathbf{\Phi}(t)\mathbf{\Phi}^n(T)\mathbf{\Psi} \tag{A.12}$$

$$= \lambda^n \mathbf{\Phi}(t)\mathbf{\Psi} \tag{A.13}$$

Therefore, if $|\lambda| < 1$, then $\boldsymbol{v}(t) \to 0$ as $t \to \infty$, and the solution is stable. On the other hand, if $|\lambda| > 1$, $\boldsymbol{v}(t)$ grows over time, and the solution is unstable.

Appendix B

Solid Propellant Physical Properties

Geometrical properties:	
length	$L = 0.5969$ m
radius	$r_c = 0.0253$ m
Combustion properties:	
linear burning rate	$\bar{r}_b = .01145$ m/sec
Physical properties:	
Propellant temperature	$T_c = 300$ K
Surface temperature	$T_s = 880$ K
Flame temperature	$T_f = 3539$ K
Thermal conductivity of propellant	$k_p = .41868$ J/m·s·K
Thermal conductivity of gas	$k_g = .083736$ J/m·sec·K
Thermal diffusivity of propellant	$\kappa_p = 1.0 \times 10^{-7}$ m^2/sec
Activation energy	$E_s/R_0 = 8011$ K
Heat release on surface	$Q_s = 700687$ J/kg
Heat release in gas phase	$Q_f = 2512080$ J/kg
Average reaction rate	$\bar{w} = 10657.1$ kg/m^3·sec
Average mass burn rate	$\bar{m} = 3.4$ kg/m^2·sec

Physical properties (cont.):

Specific heat of gas	$c_p = 2020$ J/kg·K
Specific heat of propellant	$c = 1373.6$ J/kg·K
Average specific heat ratio	$\bar{\gamma} = 1.1787$
Pressure exponent in burning rate law	$n = .3$
Temperature exponent in pyrolysis law	$\beta_1 = 0$

Bibliography

[1] Arrowsmith, D. K. and Place, C. M., *Ordinary Differential Equations*, Chapman and Hall, London, 1982.

[2] Awad, E., *Nonlinear Acoustic Instabilities in Combustion Chambers*, Ph.D. thesis, California Institute of Technology, Pasadena, CA, 1983.

[3] Awad, E. and Culick, F. E. C., "On the Existence and Stability of Limit Cycles for Longitudinal Acoustic Modes in a Combustion Chamber," *Combustion Science and Technology*, Vol. 46, No. 6, 1986, pp. 195-222.

[4] Baum, J. D. and Levine, J. N., "Numerical Techniques for Solving Nonlinear Instability Problems in Solid Rocket Motors," *AIAA Journal*, Vol. 20, No. 7, 1982, pp. 955 961.

[5] Baum, J. D., Levine, J. N., and Lovine, R. L., "Pulsed Instability in Rocket Motors; A Comparison Between Predictions and Experiments," *Journal of Propulsion and Power*, Vol. 4, No. 4, 1988, pp. 308–316.

[6] Chu, B.-T. and Kovásznay, L. S. G., "Nonlinear Interactions in a Viscous Heat-conducting Compressible Gas," *Journal of Fluid Mechanics*, Vol. 3, No. 5, 1958, pp. 494–514.

[7] Chu, B. T. and Ying, S. J., "Thermally Driven Nonlinear Oscillations in a Pipe with Traveling Shock Waves," *Physics of Fluids*, Vol. 6, No. 11, 1963, pp. 1625 1637.

[8] Clavin, P., Kim, J. S., and Williams, F. A., "Turbulence-Induced Noise Effects on High-Frequency Combustion Instabilities," *CST*, Vol. 96, 1994, pp. 61–84.

[9] Culick, F. E. C. "Oscillatory and Unsteady Processes in Liquid Rocket Engines," *ESA/ESTEC Short Course on Combustion Instabilities in Liquid Propellant Rocket Engines*, Portugal, Sept. 1993.

[10] Culick, F. E. C., "A Review of Calculations of Unsteady Burning of a Solid Propellant," *AIAA Journal*, Vol. 6, No. 12, 1968, pp. 2241–2255.

[11] Culick, F. E. C., "Some Problems in the Unsteady Burning of Solid Propellants," Naval Weapons Center, Research Report NWC TP 4668, China Lake, CA, 1969.

[12] Culick, F. E. C., "Nonlinear Growth and Limiting Amplitude of Acoustic Oscillations in Combustion Chambers," *Combustion Science and Technology*, Vol. 3, No. 1, 1971, pp. 1–16.

[13] Culick, F. E. C., "Nonlinear Behavior of Acoustic Waves in Combustion Chambers, Parts I and II," *Acta Astronautica*, Vol. 3, 1976, pp. 714–757.

[14] Culick, F. E. C., "Some Problems of Nonlinear Waves in Solid Propellant Rocket Motors," in *AGARD 53rd Meeting of the Propulsion and Energetics Panel*, 1979.

[15] Culick, F. E. C., "Combustion Instabilities in Liquid-Fueled Propulsion Systems - An Overview," in *AGARD 72B PEP Meeting*, 1988.

[16] Culick, F. E. C., "Some Recent Results for Nonlinear Acoustics in Combustion Chambers," in *AIAA 13th Aeroacoustics Conference*, 1990, AIAA Paper 90-3927.

[17] Culick, F. E. C., "Some Recent Results for Nonlinear Acoustics in Combustion Chambers," *AIAA Journal*, Vol. 32, No. 1, 1994, pp. 146–169.

[18] Culick, F. E. C., "Nonlinear Acoustics in Combustion Chambers With Stochastic Sources," Guggenheim Jet Propulsion Center, California Institute of Technology, Documents on Active Control of Combustion Instabilities CI95-6, 1995.

[19] Culick, F. E. C. and Levine, J. N., "Comparison of Approximate and Numerical Analyses of Nonlinear Combustion Instability," in *AIAA 12th Aerospace Sciences Meeting*, 1974, AIAA Paper 74-201.

[20] Culick, F. E. C., Paparizos, L., Sterling, J., and Burnley, V., "Combustion Noise and Combustion Instabilities in Propulsion Systems," in *Proceedings of the AGARD Conference on Combat Aircraft Noise*, 1992, AGARD CP 512.

[21] Culick, F. E. C. and Yang, V., "Prediction of the Stability of Unsteady Motions in Solid Propellant Rocket Motors," Chapter 18 in *Nonsteady Burning and Combustion Stability of Solid Propellants*, Progress in Astronautics and Aeronautics, Vol. 143, 1992.

[22] Culick, F. E. C. and Yang, V., *Combustion Instabilities in Propulsion Systems*, Agardograph, 1997, to be published.

[23] Denison, M. R. and Baum, E. A., "A Simplified Model of Unstable Burning in Solid Propellants," *ARS Journal*, Vol. 31, 1961, pp. 1112–1122.

[24] Doedel, E., Keller, H. B., and Kernevez, J. P., "Numerical Analysis and Control of Bifurcation Problems, (I) Bifurcation in Finite Dimensions," *Intl. Journal of Bifurcation and Chaos*, Vol. 1, No. 3, 1991, pp. 493–520.

[25] Doedel, E., Keller, H. B., and Kernevez, J. P., "Numerical Analysis and Control of Bifurcation Problems, (II) Bifurcation in Infinite Dimensions," *Intl. Journal of Bifurcation and Chaos*, Vol. 1, No. 4, 1991, pp. 745–772.

[26] Doedel, E. and Kernévez, J. P., "AUTO: Software for Continuation and Bifurcation Problems in Ordinary Differential Equations," California Institute of Technology, Pasadena, California, 1986.

[27] Doedel, E. and Wang, X., "AUTO94: Software for Continuation and Bifurcation Problems in Ordinary Differential Equations," California Institute of Technology, Pasadena, California, 1994.

[28] Franklin, J. N. and Rodemich, E. R., "Numerical Analysis of an Elliptic-Parabolic Partial Differential Equation," *SIAM Journal on Numerical Analysis*, Vol. 5, No. 4, 1968, pp. 680–716.

[29] Gadiot, G. M. H. J. L. and Gany, A., "Instability Modeling With Nonlinear Pressure Coupling," *Recherche Aérospatiale*, Vol. 5, 1988, pp. 23–37.

[30] Garcia, A. L., *Numerical Methods for Physics*, Prentice-Hall, Inc., New Jersey, 1994.

[31] Gardiner, C. W., *Handbook of Stochastic Methods for Physics, Chemistry, and the Natural Sciences*, Springer-Verlag, Berlin, 1985.

[32] Greene, W. D., *Triggering of Longitudinal Combustion Instabilities in Rocket Motors*, Master's thesis, The Pennsylvania State University, 1990.

[33] Guckenheimer, J. and Holmes, P., *Nonlinear Oscillations, Dynamical Systems, and Bifurcations of Vector Fields*, Springer-Verlag, New York, 1983.

[34] Hart, R. W., Bird, J. F., and McClure, F. T., "The Influence of Erosive Burning on Acoustic Instability in Solid Propellant Rockets," in *Solid*

Propellant Rocket Research, Progress in Astronautics and Rocketry, Vol. 1, pp. 423–499, Academic Press, 1960.

[35] Horsthemke, W. and Lefever, R., *Noise-Induced Transitions*, Springer-Verlag, Berlin, 1984.

[36] Iooss, G. and Joseph, D. D., *Elementary Stability and Bifurcation Theory*, Springer-Verlag, New York, 1980.

[37] Jahnke, C. C. and Culick, F. E. C., "An Application of Dynamical Systems Theory to Nonlinear Combustion Instabilities," in *AIAA 31st Aerospace Sciences Meeting*, 1993, AIAA Paper 93-0114.

[38] Jahnke, C. C. and Culick, F. E. C., "An Application of Dynamical Systems Theory to Nonlinear Combustion Instabilities," *Journal of Propulsion and Power*, Vol. 10, No. 4, 1994, pp. 508–517.

[39] Jahnke, C. C. and Culick, F. E. C., "Nonlinear Energy Transport Between Longitudinal Acoustic Modes in Cylindrical Combustion Chambers," in *30th AIAA/ASME/SAE/ASEE Joint Propulsion Conference*, 1994, AIAA Paper 94-3190.

[40] Keller, H. B., "Numerical Solution of Bifurcation and Nonlinear Eigenvalue Problems," in *Applications of Bifurcation Theory*, pp. 359–384, Academic Press, 1977.

[41] Keller, H. B., *Lectures on Numerical Methods in Bifurcation Problems*, Tata Institute of Fundamental Research, Bombay, 1987, notes by A. K. Nandakumaran and M. Ramaswamy.

[42] Kim, S. I., *Nonlinear Combustion Instabilities in Combustion Chambers*, Ph.D. thesis, The Pennsylvania State University, 1989.

[43] Kooker, D. E. and Zinn, B. T., "Triggering Axial Instabilities in Solid Rockets: Numerical Predictions," in *AIAA/SAE 9th Propulsion Conference*, 1973.

[44] Krylov, N. M. and Bogoliubov, N. N., *Introduction to Nonlinear Mechanics*, Princeton University Press, Princeton, 1947.

[45] Levine, J. N. and Baum, J. D., "A Numerical Study of Nonlinear Instability Phenomena in Solid Rocket Motors," *AIAA Journal*, Vol. 21, No. 4, 1983, pp. 557 564.

[46] Lin, W. W. H., "On the Energy in Acoustic Modes," Guggenheim Jet Propulsion Center, California Institute of Technology, Documents on Active Control of Combustion Instabilities CI95-1, 1995.

[47] Ma, Y., Moorhem, W. K. Van, and Shorthill, R. W., "Experimental Investigation of Velocity Coupling in Combustion Instability," *Journal of Propulsion and Power*, Vol. 7, No. 5, 1991, pp. 692–699.

[48] Marble, F. E., "Dynamics of a Gas Containing Small Solid Particles," in *5th AGARD Colloquium*, 1963.

[49] Marble, F. E., "The Dynamics of Dusty Gases," *Annual Review of Fluid Mechanics*, Vol. 2, 1970, pp. 397–446.

[50] McClure, F. T., Bird, J. F., and Hart, R. W., "Erosion Mechanism for Nonlinear Instability in the Axial Modes of Solid Propellant Rocket Motors," *ARS Journal*, Vol. 32, 1962, pp. 375–378.

[51] Paparizos, L. and Culick, F. E. C., "The Two-Mode Approximation to Nonlinear Acoustics in Combustion Chambers. I. Exact Solutions for Second Order Acoustics," *Combustion Science and Technology*, Vol. 65, No. 5, 1989, pp. 39–65.

[52] Paparizos, L. and Culick, F. E. C., "The Two-Mode Approximation to Nonlinear Acoustics in Combustion Chambers. II. Influence of Third-Order Acoustics and Mean Flow in Triggering," unpublished, 1990.

[53] Powell, E. A., Padmanabhan, M. S., and Zinn, B. T., "Approximate Nonlinear Analysis of Solid Rocket Motors and T-Burners: Volume 1," Air Force Rocket Propulsion Laboratory, Technical Report AFRPL-TR-77-48, Edwards AFB, CA 93523, 1977.

[54] Sirignano, W. A. and Crocco, L., "A Shock Wave Model of Unstable Rocket Combustors," *AIAA Journal*, Vol. 2, No. 7, 1964, pp. 1285–1296.

[55] Yang, V. and Culick, F. E. C., "On the Existence and Stability of Limit Cycles for Transverse Acoustic Oscillations in a Cylindrical Combustion Chamber, I. Standing Modes," *Combustion Science and Technology*, Vol. 72, No. 1, 1990, pp. 37–65.

[56] Yang, V., Kim, S. I., and Culick, F. E. C., "Third-Order Nonlinear Acoustic Waves and Triggering of Pressure Oscillations in Combustion Chambers, Part I: Longitudinal Modes," in *AIAA 25th Aerospace Sciences Meeting*, 1987, AIAA Paper 87-1873.

[57] Yang, V., Kim, S. I., and Culick, F. E. C., "Third-Order Nonlinear Acoustic Instabilities in Combustion Chambers, Part II: Transverse Modes," in *AIAA 26th Aerospace Sciences Meeting*, 1988.

[58] Yang, V., Kim, S. I., and Culick, F. E. C., "Triggering of Longitudinal Pressure Oscillations in Combustion Chambers, I: Nonlinear Gasdynamics," *Combustion Science and Technology*, Vol. 72, No. 5, 1990, pp. 183–214.

[59] Zinn, B. T. and Powell, E. A., "Application of the Galerkin Method in the Solution of Combustion Instability Problems," *Proceedings of the 19th International Astronautical Congress*, Vol. 3, 1970, pp. 59-73.